To the Graduate Council:

I am submitting herewith a thesis written by Austin P. Albright entitled "The Detection of Stress Corrosion Cracking in Natural Gas Pipelines using Electromagnetic Acoustic Transducers." I have examined the final electronic copy of this thesis for form and content and recommend that it be accepted in partial fulfillment of the requirements for the degree of Master of Science, with a major in Electrical Engineering.

Hairong Qi

Hairong Qi, Major Professor

We have read this dissertation
and recommend its acceptance:

Donald W. Bouldin

Donald W. Bouldin

Michael J. Roberts

Michael J. Roberts

Accepted for the Council:

Carolyn R. Hodges

Carolyn R. Hodges, Vice Provost and Dean of the Graduate School

(Original signatures are on file with official student records.)

The Detection of Stress Corrosion Cracking in Natural Gas Pipelines using Electromagnetic Acoustic Transducers

A Thesis
Presented for the
Master of Science Degree
The University of Tennessee, Knoxville

Austin Peter Albright
December 2007

Dedication

To the glory of my Lord and Savior, Jesus Christ
and to my beautiful, patient wife Melissa.

Acknowledgments

First and most importantly, I am deeply indebted to my wife Melissa and to my family (The Albrights - Steve, Peggy, Seth, Cindy, Kevin, and Manju) (The Dyers - Ron, Cindy, Kaye, Christy, and Ashley) for there encouragement and support, especially when I would get stressed and frustrated about every little thing and flip-out. Where I am today is in no small part due to their love and support... especially Melissa's.

Secondly, I would like to acknowledge and thank Dr. Venugopal "Venu" K. Varma and Mr. Raymond W. Tucker, Jr. for everything they have done for me. Their work is the foundation of all the work I have done, which is covered in this thesis. Dr. Varma and I spent hours and hours collecting data from different pipes, and eventually the machined pipe. Mr. Tucker and Dr. Varma allowed me to develop my skills as a researcher within a supportive team environment. Additionally, I would like to thank Mr. Tucker for being my "engineering dad." His willingness to support my work, his guidance throughout my studies on selecting classes, prioritizing my life, encouraging me to apply for fellowships, and to pursue graduate school as the means to a career in research and development.

I also want to thank Dr. Hairong Qi for her unbelievable patience with me through out the excruciatingly slow process of writing this thesis. The two and half years of research seemed to fly by compared to the year and a half it has taken me to write this. Dr. Qi has treated me like a real person, but still managing to keep me moving forward, all while coming to realize and handle the fact that I am perpetually wrong about how long I think it will take me to do something and when it "surely" will be done by. I want to thank all of the AICIP crew for their friendship and company during this process. For sitting through my thesis defense presentation every time I really thought I was going to be defending it that month.

I want to acknowledge Mr. Conard Murray at my undergraduate alma mater, Tennessee Technological University, as well. Mr. Murray taught me more hands on electronics design, construction, and debugging then any course I ever taken. He helped me keep my hands dirty and the soldering iron hot. Not to mention the art of scrounging and salvaging I learned by following him around has saved me hundreds of dollars in parts and repairs and has definitely benefited the mobile sensor platforms in the AICIP lab at the University of Tennessee - Knoxville.

Also important to my sanity during the writing process were Tom Karnowski and Philip Bingham out at Oak Ridge National Lab. They are my “work buddies.” Taking the time talk when I was needed a break to regain prospective on whatever detail I was obsessing about at that point in the writing process.

I would like to thank the members of my committee: Dr. Donald W. Bouldin and Dr. Michael J. Roberts. I greatly appreciate their time and patience as I perpetually told them I would have this thesis to them by a specific day and then missed it every single time.

Finally, I acknowledge that there is not anything funny in this thesis. Usually, I try and add something humorous just to show that engineers do have a sense of humor. Unfortunately, I could not think of any good puns involving stress corrosion cracks that would crack anybody up.

Abstract

This thesis describes the refinement of a non-destructive, in-line inspection system sensor for the detection of stress corrosion cracks (SCCs) in natural gas pipelines. The sensors are prototype electromagnetic acoustic transducers (EMATs) for non-contact ultrasonic inspection. The focus areas discussed involve the statistically validated performance improvements achieved through the addition of 12 more features, the addition of Principal Component Analysis plus Linear Discriminant Analysis (PCA+LDA) to the classification algorithm, and most significantly the creating of a training set. The training set allowed PCA+LDA to be included in the classification algorithm, as well as allowing one set of no-flaw signature features, one PCA projection matrix, and one LDA projection matrix to be used on multiple pipes and on multiple scanned paths from a pipe. A discrete wavelet decomposition is used to separate the frequency content of each EMAT sample (signature) into five distinct bands. From these decomposed signatures, features are extracted for classification. The classification begins with the projection of the features using the PCA projection matrix derived from the training set, immediately followed by the projection of the PCA projected features using the LDA projection matrix that was also derived from the training set. Finally, the PCA+LDA projected features are classified based on their Mahalanobis distances from the PCA+LDA projected no-flaw training set features. Using the improved feature set and this classification procedure, SCC identification improved 14% and there was an 80% reduction in the number of false positives. In addition, there was a 30% improvement in the detection of the most critical SCCs. SCCs whose average through wall depths were between 35% and 54%.

Contents

List of Tables

List of Figures

Chapter 1

Introduction

According to the Energy Information Administration's 2006 Annual Energy Review, the United States consumed 22.2 trillion cubic feet of natural gas in 2005 and are projected to have consumed 21.8 trillion cubic feet during 2006 [1]. Natural gas is the second most common source of energy production in the United States; accounting for 33.76% of the energy generated in 2005 and is estimated to have fueled the same amount of generation in 2006. This translate into 18.6 quadrillion Btu of energy in 2005, 19 quadrillion Btu in 2006 [1].

All of this supply at some point must travel through a portion of the interstate natural gas distribution system. The Office of Pipeline Safety (OPS) 2005 statistics for natural gas transmission pipelines reports that there is currently 45,998 miles of steel transmission pipe with diameters over 20 inches but less than 28 inches and 69,332 miles of pipe with diameters over 28 inches, for a total large diameter pipeline mileage of 115,330 [2]. This is 40.4% of all natural gas transmission pipeline in the U.S. If you consider the fact that pipes as small as four inches in diameter can be classified as transmission pipelines it is clear that the majority of all natural gas is distributed via these large diameter steel pipelines. The 2005 OPS statistics for transmissions pipelines also show that of the 285,782.3 miles of natural gas transmission pipeline in the U.S. 72.9% of it is at least 25 years old, 62.4% is at least 35 years old, and 37.2% is 45 years old or more. A mere 14.7% of all transmission pipeline was constructed in the last 15 years [2]. Because of the significant role of natural gas in every aspect of our society, as well as the danger inherent to a combustible gas, it is critical that the natural gas transmission system be inspected and maintained.

The regular inspection and maintenance of pipelines is needed in order to provide reliable service, protect the public, and lower cost. While there are numerous challenges to pipeline inspection the most prominent and long running challenge is access to the pipes. Almost all natural gas pipelines are buried and since rust, corrosion, pitting, and cracking, to name a few defects that are inspected for, can occur anywhere on the pipe excavation for inspection is not a reasonable option. Which is why the present advanced pipe inspection tools inspect pipes for internal and external defects and damage without requiring their excavation. This process of inspecting the pipe from the inside is known as in-line inspection (ILI). ILI tools are loaded inside the pipeline to be inspected and perform non-destructive inspection (NDI) (also known as non-destructive testing (NDT)). The ILI tools travel inside the pipes and are generally propelled by the pressurized contents of the pipeline. These ILI tools are referred to as pipe inspection gauges (PIGs).

While there are several methods which have been and continue to be used for in-line NDI they all suffer from either the out right inability to detect stress corrosion cracks (SCCs), or require the use of a coupling liquid that means natural gas distribution must be halted. Because of these issues natural gas pipelines are seldom, if ever, fully inspected for SCCs.

1.1 Motivation

Only in the last few decades has the desire of the industry to locate stress corrosion cracks (SCC) developed in to an actual demand and need for SCC detection. This is due to the shear age of the pipelines along with increased governmental regulation and oversight plus. Though there are methods for inspecting pipelines for defects and damage these techniques all suffer from a variety of disadvantages, such as:

- Inability to detect SCC.
- Require a liquid coupling.
- Require cutting or degrading service to the end-user.
- Cannot be performed as an in-line inspection technique.

Of these items obviously the inability to detect SCCs is the biggest problem. Followed by the need for liquid coupling, which itself causes the operation of the pipeline to be stopped or at the best limited. The current federally congressionally mandated regulations for the inspection of gas pipelines, 49 CFR 192, which extensively references the American Society of Mechanical Engineers and American National Standards Institute standard on "Gas Transmission and Distribution Pipping Systems" (ASME\ANSI B31.8) and "Managing System Integrity of Gas Pipelines" (ASME\ANSI B31.8S), list only one method for determining the presence of SCCs, direct assessment. Direct assessment means excavating a section of pipeline in a location favorable to the formation of SCCs, removing any protective coating, cleaning the exposed pipe, and then visually inspecting the area using magnetic particle inspection.* So while locations with conditions conducive to the formation of SCCs are logical places to check for SCCs, inspecting a few feet of a multi-mile pipeline still leaves many opportunities for disaster. Entire pipelines need to be inspected every few years to find and mitigate any SCC damage and to monitor for SCC formation.

This has led to research into the use of Electromagnetic Acoustic Transducers (EMATs) as a means of performing ultrasonic inspection of ferromagnetic materials (e.g., steel pipes, steel plate, steel beams, etc.) without the need for a liquid couplant. The focus of the research covered by this thesis is to detect SCCs using EMATs in large diameter natural gas pipelines, specifically 26-inch and 30-inch diameter pipelines.

1.2 Stress Corrosion Cracks

Stress corrosion cracks are a growing concern due to the age of the nation's infrastructure. The gradual process that leads to the formation of SCCs has meant that until the last few years SCCs were not a high priority (compared to mechanical damage.) The characteristics of SCCs and their formation contributes to the difficulties in detecting them. These traits and the method for visually identifying SCCs are discussed in the following sections.

1.2.1 Source and Characteristics of SCCs

The majority of SCCs result from the same basic process, though as with any natural phenomena there are exceptions to the "rule". SCCs are considered to be an environmental failure source [3]. The general series of events that lead to the formation

*This process is also known as a Bell Hole Examination

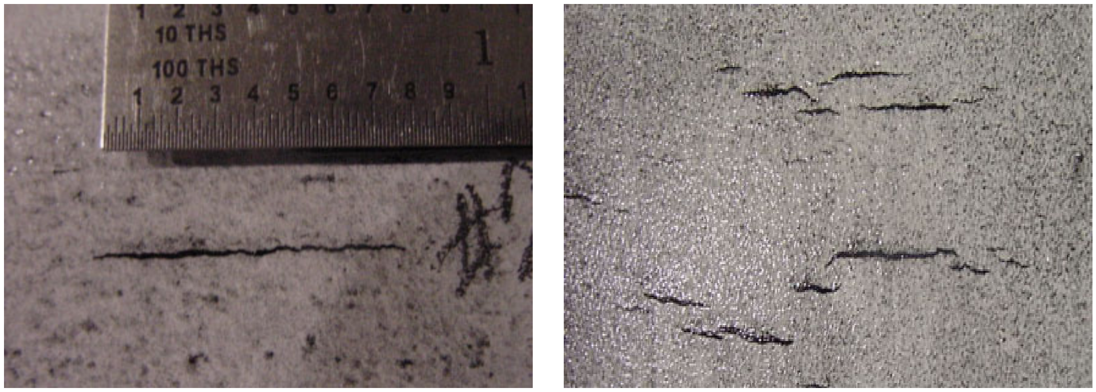

(a) Single SCC (b) SCC Colony

Figure 1.1: Typical SCCs formations. (a) A single SCC. (b) A colony of SCCs. Notice the “zig-zag” nature of the cracks. This is the primary trait for distinguishing a real SCC from a scratch in the pipe identified using magnetic particle inspection.

of an SCC starts with the penetration of the protective coating (e.g., tar, PVC, etc) on the pipe. These breaches usually are due to either damage to the coating during installation, a pressure point from a rock or such cutting through the coating, coating break down, or a combination of these. Once moisture is under the coating, corrosion forms on the pipe wall. A crack (or cracks) form in the corrosion due to cyclic loading of the pipe. This cyclic loading primarily comes from changes and/or fluctuations in the operating pressure of the pipeline. Extreme temperature variations of the pipe’s environment can also contribute. The stresses of expansion and contraction due to temperature changes are far less significant than variations in internal operating pressure.

SCCs form along the axial direction of pipes almost exclusively. SCCs can occur as single cracks, Figure 1.1(a), or in colonies, Figure 1.1(b). SCCs can be distinguished from other line-like marks and/or defects by the piecewise nature that an SCC “line” exhibits compared to the smooth, continuous “line” of other line-like defects, such a scratch. This piecewise trait is due to the fact that virtually every SCC of significant length, i.e. greater than a third of an inch, is composed of SCCs that have grown together as seen in Figure 1.1, 1.2, and 1.3. There are two types of SCCs, high pH SCC and near-neutral pH SCC, where pH refers to the pH of the actual pipe surface environment at the crack location [4].

SCCs occur in all types of metal. The aerospace industry has been particularly interested in SCC for much longer than the pipeline industry. So while there is much more information and research data available on SCCs in aluminum and other metals used by the aerospace industry there is a very limited amount of information on SCCs in pipelines. Due to the rarity of SCC samples available for study the profile of SCCs with respect to how they penetrate through a pipe wall is not well known. It is known that SCCs are an inter-granular crack. That is an SCC will usually crack between the actual grains that form the steel of the pipe.

1.2.2 Visual SCC Identification

There is a technique available that can make SCCs visually detectable, magnetic particle inspection. Magnetic particle inspection (MPI) uses fine magnetic particles that are applied to the area to be inspected. There are two types of particles, color contrast particles visible under normal lighting and fluorescent particles that are only visible under a black light. Either type of particle can be applied in either a liquid suspension (wet) or as a dry powder. The mean particle size for the Magnaflux®[†] fluorescent particle is six microns ($6\mu m$) and the black color contrast particles are less than 20 microns ($20\mu m$) [6, 7]. Once the area has been "painted" with the suspension a magnetic field is applied across the site. The magnetic field is created so that potential defects will be perpendicular or close to perpendicular to the flux lines. Any "breaks" in the surface of the magnetized object being inspected allow leakage which draws the magnetic particles in to the "break" [8]. This is more clearly explained in the following quote from the NDT Resource Center

> "A strong magnetic field is established in the pipe wall using either magnets or by injecting electrical current into the steel. Damaged areas of the pipe can not support as much magnetic flux as undamaged areas so magnetic flux leaks out of the pipe wall at the damaged areas" [9].

The closer to perpendicular a defect is to the flux lines the stronger the flux leakage will be and ideally more particles that will be drawn into the defect. The size of a defect is directly related to the amount of potential flux leakage that could occur due to the defect. A small crack, even perfectly oriented with the magnetic field, will not attract as many particles as a larger crack several degrees off of perpendicular with

[†] These particle sizes are for Magnaflux® 7HF black color contrast product and Magnaglo® 14A Aqua-Glo fluorescent particles. Magnaflux® is a company founded by the discoverer of "magnetic particle crack-finding method" [5] and is still a leading producer and distributor of MPI equipment and supplies today.

the magnetic field will. If fluorescent magnetic particles are used a black light would be used at this point in the MPI process to check for any defects in the area coated with the particle suspension. Figure 1.2 shows an SCC colony identified using liquid fluorescent MPI. If color contrast particles are used the metal must either be a light color or a contrasting background applied, such as white paint. Figure 1.3 shows an SCC colony identified using liquid color contrast MPI. If any defects are located, measurements are taken from one end of the pipe segment to the beginning of the defect, from the longitudinal weld to the defect, and the length of the defect. Color photographs are also taken of the defect. When the inspection of the selected area is complete the magnetic field is removed and if desired/required the area is rinsed with water to remove the particles, suspending liquid, and contrast paint if used. Regardless, of whether the area is rinsed or not the particles do not remain magnetized and cannot be used to identify defects without re-applying both the magnetic field and a fresh coat of the liquid suspension.

There are also some major caveats that come with the use of MPI. First, as is probably apparent at this point, the pipe section must be removed from service, excavated, and any protective coating stripped from the pipe. Second, scratches, manufacturing defects, manufacturing handling marks, etc. are also made visible. This makes it very difficult to identify SCCs that might be "mixed" in with any other crack-like markings e.g., scratches, manufacturing process marks. Finally, and most significantly, is that no depth information can be obtained using MPI. While these problems mean that superficial marks can be misinterpreted as SCCs, the characteristics of SCCs do help to distinguish SCCs from manufacturing marks and scratches.

The decommissioned pipe sections containing SCCs that were used in the blind test of our sensor system where all inspected using liquid fluorescent magnetic particle inspection when the sections were first obtained by the Battelle Pipeline Simulation Facility (PSF).Since naturally occurring SCC samples are of such rarity, the SCC sample pipes have been shared with organizations all across the nation. Sometime the borrowing organization alters the pipe such as by cutting off a section and$backslash$or welding a section on to the SCC pipe. This was the situation with pipe sample inspected during the most recent blind test of the system. The length of the pipe was changed while on loan. The length of the pipe is what the defects found during the original MPI inspection was referenced to. With the particles from that MPI assessment no longer present, the defect locations could not be confirmed without

Figure 1.2: Fluorescent MPI image of an SCC colony from a decommissioned natural gas pipeline. The box around the SCC colony is $6\frac{1}{4}$ inches long by 4 inches wide.

Figure 1.3: Color contrast MPI image of an SCC colony from a decommissioned natural gas pipeline. The SCC colony is $2\frac{8}{10}$ inches long and approximately $1\frac{2}{5}$ inches wide.

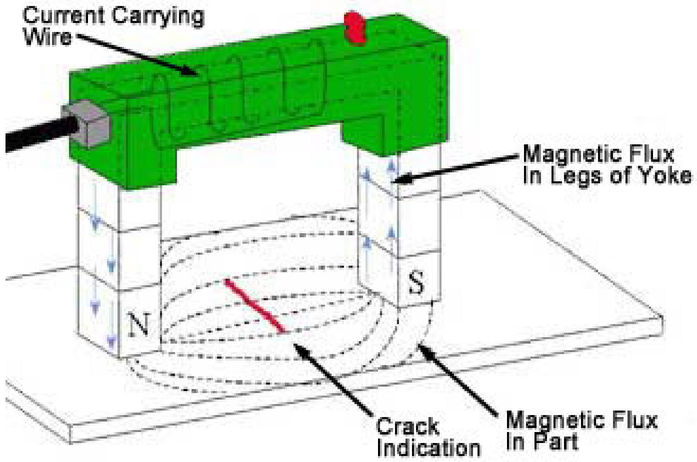

Figure 1.4: An MPI yoke used to create the magnetic field when the entire object under test is to large or unwieldy [10].

performing MPI again. In the specific case of the pipe section inspected during the blind test, it the full-pipe MPI inspection was performed in 1994. At some unspecified time later, it was loaned to an organization that removed a piece from an end of the pipe and then later reattached a piece. The inconsistences in the length of the pipe came to our attention when the "answer key" (the 1994 MPI assay) was distributed. With the locations of defects found in the 1994 assay in doubt, a trip was made to the PSF to re-inspect the locations given in the 1994 assay using MPI, as well as locations that the sensors indicated possible defects to be[‡]. In this situation, a color contrast suspension mixture was used to re-inspect the locations of interest via MPI. The mixture contained white contrast paint along with black magnetic particles. An electromagnetic yoke, Figure 1.4, was used to create the magnetic field. In the end the MPI inspection allowed us to take new measurements from a known reference point to the location of re-confirmed defects and to determine if a defect was actually present (some defects listed in the 1994 assay could not be located anywhere on the pipe), and verify the presence of defects not found during the 1994 assay (two "new" SCCs were confirmed).

[‡] Since the blind testing was complete the roofing felt paper used to conceal the outside of the pipe was removed and we were allowed to see and inspect the pipe.

1.3 Current In-Line Inspection Methods

There are a variety of commercially used in-line inspection techniques. The vast majority are divided into one of two categories: 1. Ultrasonic Techniques and 2. Magnetic Flux Leakage (MFL). Each of theses two areas is discussed along with their advantages and disadvantages in regards to their use for inspection natural gas pipelines.

1.3.1 Ultrasonic Methods

Ultrasonic inspection has been in use for non-destructive testing (NDT) of objects for years and as such is used to perform in-line inspection of pipelines. Piezoelectric transducers are the most commonly used means of creating an ultrasonic wave in the pipe wall. However, these transducers must contact the pipe wall. This contact, more precisely coupling, is provided through the use of a liquid couplant. NDT performed using ultrasonics with a liquid coupling are capable of detecting all types of defects. The reason there is a need for another means of performing ultrasonic inspection is mostly due to the use of a liquid couplant in a natural gas pipeline. Using a liquid couplant requires that service be cut so that a liquid slug can be created for the inspection system to "ride" in, Figure 1.5. When a liquid slug is used in a natural gas pipeline, the pipeline can only contain small elevation changes. This is because of the pressure gradient that is required across the liquid slug in order for to propel the slug through the pipeline. Large elevation changes, even when made gradually, can require a dangerous increase in system pressure to push the liquid slug up hill and of course the reverse can occur in front of the slug when going down hill. Another serious complication with using a liquid slug is that the line to be inspected must be isolated from any connecting lines (e.g., feeder lines/laterals) to prevent losing the couplant [11]. This essentially rules out using a liquid slug in mountainous and hilly terrain [4]. Two other problems with using a liquid couplant in natural gas pipelines are the difficulties in maintaining a constant rate of travel and the potential need to dry the pipeline after the use of a liquid couplant to prevent possible contamination, corrosion, and freezing[§].

[§]This freezing is with respect to equipment on the line such as pump stations.

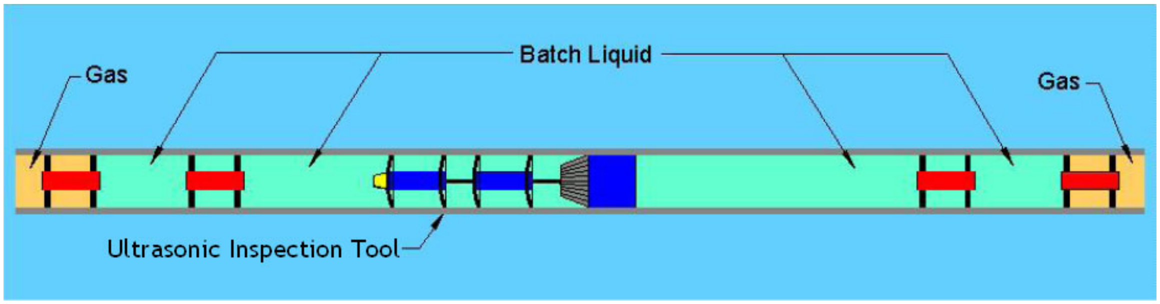

Figure 1.5: An ultrasonic inspection tool that requires a couplant can be operated in a natural gas pipeline by creating a slug of liquid for it to ride in, as illustrated in this figure [4].

1.3.2 Magnetic Flux Leakage (MFL)

Magnetic flux leakage (MFL) originated from MPI. While MPI uses magnetic particles, which are attracted into defects by the magnetic leakage from the defect, MFL uses sensors to measure the magnetic field "leaking" from defects. MFL has been in use for over 40 years and so the capabilities of MFL are well known [12]. MFL uses Hall effect sensors to measure the leakage from defects. An MFL tool developed and available for commercial use from the ROSEN Group is shown in Figure 1.6. This ROSEN PIG is a high resolution MFL tool in that the flux leakage sensors are thinner circumferentially than those used on a standard MFL PIG, i.e. there are more sensors per circumferential inch than on a standard PIG.

MFL PIGs can provide information on the size, depth, and location of metal loss defects e.g., pitting, corrosion, gouges, etc. However, MFL can not effectively or reliable detect SCCs. This is because the orientation of the magnetic field generated by MFL PIG is axially along the pipe. Since SCCs are also oriented axially in pipes there is minimal disruption of the magnetic field and therefore minimal flux leakage as clearly illustrated in Figure 1.7 [12, 14]. As an example, the effect of the magnetic field orientation to defect orientation is shown in Figure 1.8 for an actual MFL PIG scan on pipe containing synthetic defects. This data clearly shows the limitation of MFL to detect axially oriented defects. Also consider the fact that the narrowest axial oriented man-made defects, Figure 1.8(b), is still one inch wide, while the widest of our synthetic SCCs are only 0.012-inches wide. This is 84 times wider than our widest synthetic SCC but the MFL response barely registers. While MFL has been successful used for years to locate metal loss defects and in recent years "high-resolution" MFL tools have been developed that significantly improve the defect sizing

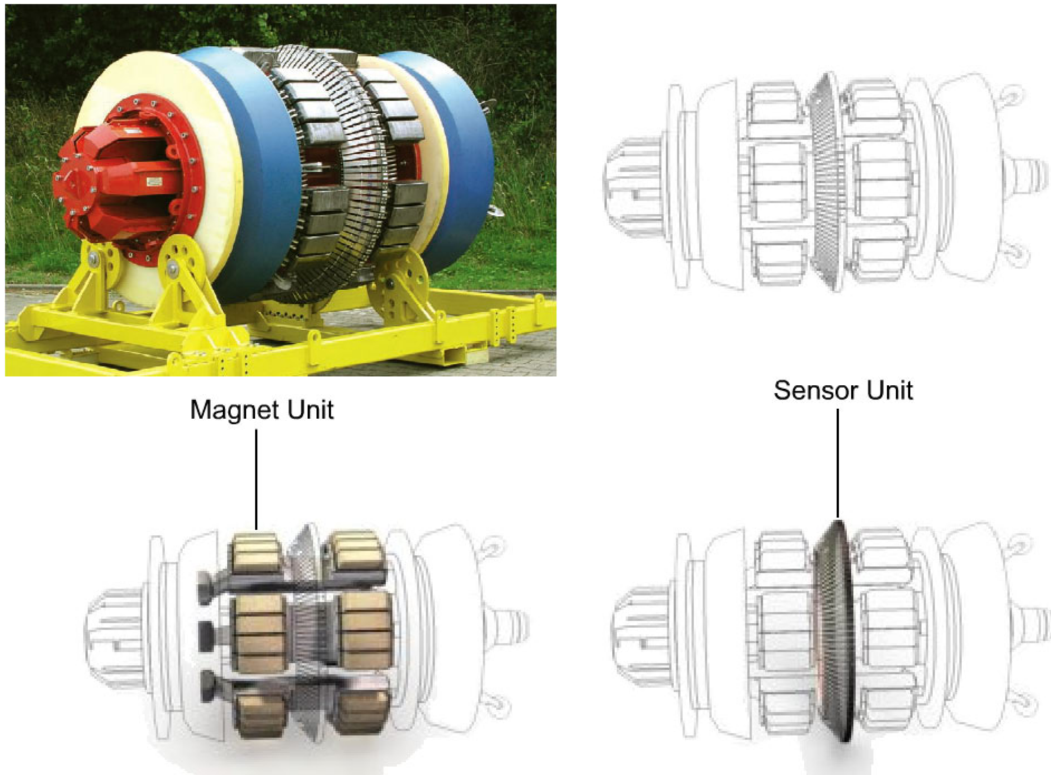

Figure 1.6: Shown here is a 56 inch diameter MFL in-line inspection pig [13].

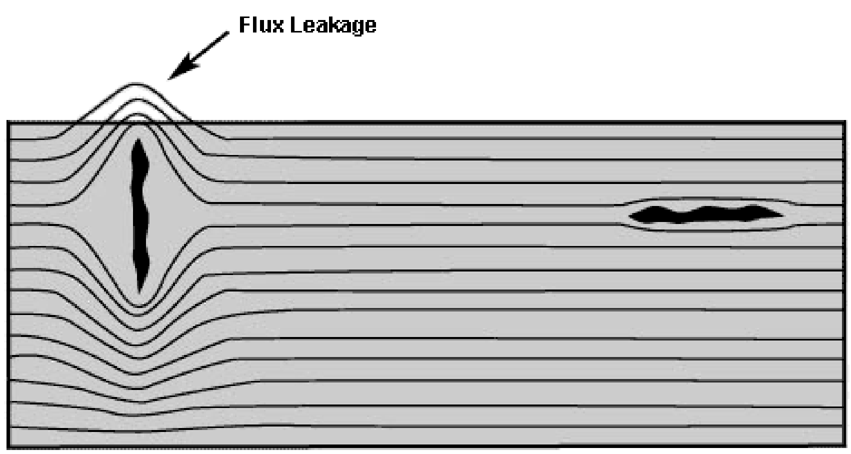

Figure 1.7: The orientation of the magnetic field compared to the orientation of the defect is critical in whether a defect is detectable or not for both MFL and MPI inspection methods. [14].

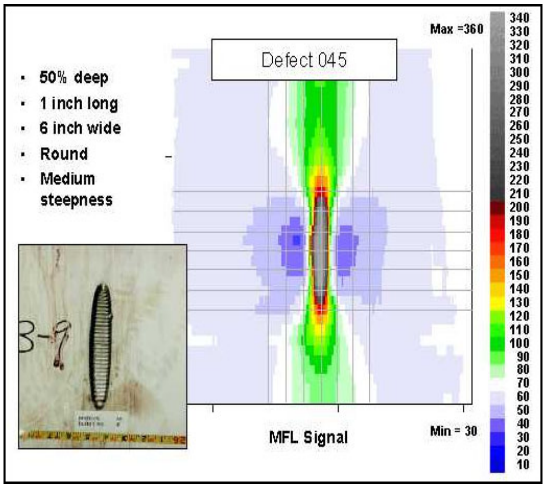

(a) 1-in axially, 6-in circumferentially, 50% through pipe wall, 45° edge bevel

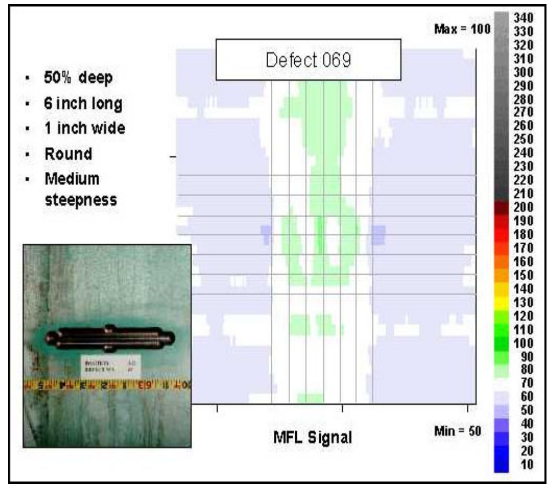

(b) 6-in axially, 1-in circumferentially, 50% through pipe wall, 45° edge bevel

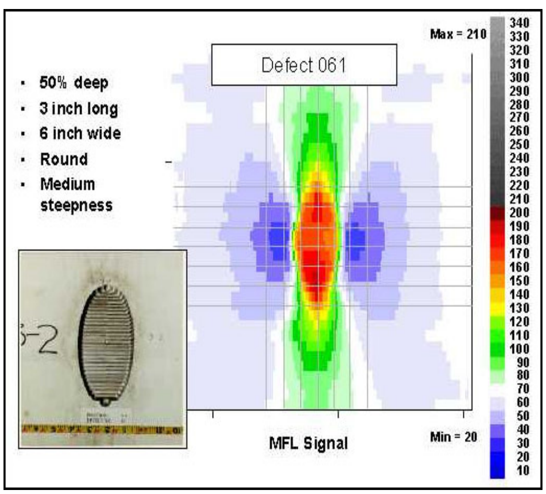

(c) 3-in axially, 6-in circumferentially, 50% through pipe wall, 45° edge bevel

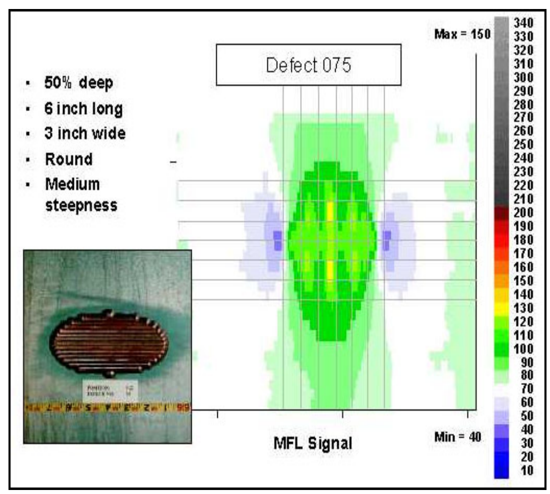

(d) 6-in axially, 3-in circumferentially, 50% through pipe wall, 45° edge bevel

Figure 1.8: These MFL scans of man-made metal loss defects clearly show the limitations of even high resolution MFL to detect axially oriented defects. The color bar on the right of each figure is amount of magnetic flux leakage measured in gauss The max and min in each figure refer to the maximum and minimum leakage measured on that defect [15].

and location accuracy. Still, even these “high-resolution” MFL systems are still unable to detect all but the largest and most sever axial defects of any type. There has and continues to be research toward producing an MFL unit that creates a circumferential magnetic field. For more information and a detailed discussion of MFL’s capabilities see [12, 15].

1.4 Electromagnetic Acoustic Transducers

1.4.1 Basic EMAT Properties

Electromagnetic acoustic transducers (EMATs) are used to create an ultrasonic guided wave without the need of a liquid coupling. This capability is what makes EMATs stand out as a solution for providing non-contact (couplant-free) ultrasonic inspection of natural gas pipelines, and can be designed to fit almost any pipe diameter. EMATs affect the atomic lattice of the material to produce a guided wave. There are a number of wave types that can be produced with an EMAT depending on the coil and magnet configuration. Several of the more common types used for material inspection are the Shear Vertical (SV), Shear Horizontal (SH), Lamba wave, and longitudinal wave [16, 17, 18]. The ORNL EMATs designed by Dr. Venugopal K. Varma¶ are specifically tailored to create an SH-wave which propagates circumferentially in the pipe wall. The ultrasonic wave an EMAT creates in the pipe wall is produced by the interactions of a static magnetic field from the strong permanent magnets in the EMAT and the oscillatory electromagnetic field produced when a coil of wire, also inside the EMAT, is energized. The coil inside the EMAT overlays the permanent magnets and is excited by a widowed frequency burst. When the coil is excited it produces eddy currents in the pipe wall, which in the presence of the static magnetic field results in the production of an electromagnetic force given by the Lorentz equation, Eqn. (1.1),

$$f = J \times B_o \tag{1.1}$$

where,

¶Dr. Venugopal K. Varma has been the primary investigator of the EMAT natural gas pipeline inspection sensor project at Oak Ridge National Laboratory since its inception in late 2001.

f body force per unit volume,

J the induced dynamic current density,

B static magnetic induction.

If the material being inspected is ferromagnetic then there is also a magnetostrictive contribution to the body force, f [19]. The ORNL EMATs have been designed so that the face (the side that goes toward the inner pipe wall) fits the inside curvature of 30-inch diameter pipes‖ and can also operate in 26-inch diameter pipes. One of the ORNL EMATs is shown in Figure 1.9 without the protective mylar film used to cover the epoxy-potted coil and permanent magnets. The mylar film serves as a replaceable wear surface to protect the EMAT. While the theory and detail operation and properties of EMATs can be shown and explained with the combination of calculations and principals used with electromagnetic fields and thinking of the pipe wall as a waveguide (which it is) with its reflection coefficients and transmission line properties, these details are beyond the scope of this research, but are available with in-depth explanations of calculations and principles in [19].

There is one more noteworthy issue specific to the collection of data from pipe sections regarding the reflection of the guided wave. The issue is that in the sections of pipe used for testing when the EMATs are with in 12 to 16 inches of the end of the pipe the ultrasonic waves are reflect off the end. The ends of the pipe are equivalent to a "wall" placed across the end of the wave guide that is the inner and outer faces of the pipe wall. This is because the ends of the pipe are junctions between two transmission mediums with extremely different propagation velocity constants. The closer the EMATs get to the end the strong the reflected wave strength and the more acutely corrupted the sampled signals. This means that the data collected close to the ends of the pipes is unreliable. Fortunately, the end-effect issue is only a concern in the test pipes, since operational pipelines are continuous welded pipe.

1.4.2 Basic Operation of an EMAT

EMATs can be configured and driven in several ways. There are three "standard" methods/modes for configuring ultrasonic transducers, which are Pulse-Echo, Pitch-Catch, and Through-Transmission [20].

‖Pipe diameters are given for the outside diameter, inside diameters vary based on the wall thickness. This variation is not enough to prevent a 30-inch diameter tool from working in any 30-inch diameter pipe. I mention this because pipes are listed, classed, and discussed referring to the outside diameter (ODS) and wall thickness.

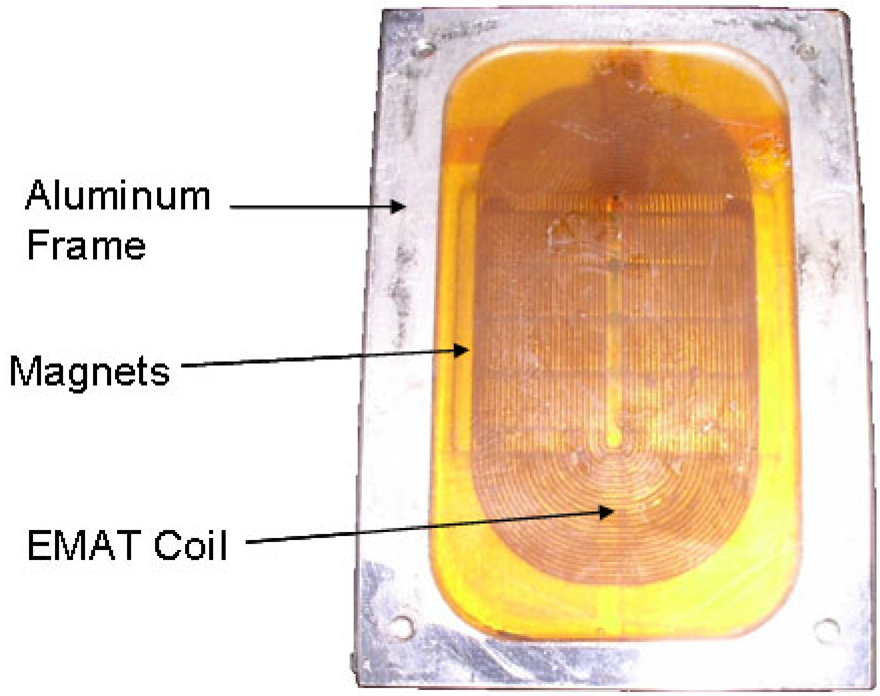

Figure 1.9: The EMAT head without the replaceable protective mylar. Designed to produce Shear wave in a 30-inch diameter pipe.

- Pulse-Echo mode uses one transducer to both transmit and receive the signal, Figure 1.10(a). Pulse-echo is commonly used to inspect planar objects such as steel plates, semi-conductor wafers, etc. Pulse-echo is problematic for pipeline inspection because the transducer is moving while the echo is returning from the outer pipe wall.

- Pitch-Catch mode can be done using one or two transducers. When two transducers are used one transducer pitches (transmits) the signal and the other transducer catches (receives) the signal. The transducers do not change functionality i.e. the transmitter is always the transmitter, the receiver is always the receiver. The pipe's inner and outer walls function as a wave guide for the transmitted ultrasonic wave "carrying" it to the receiver, Figure 1.10(b). The spacing between the two transducers is variable depending on the hardware used and other user selected traits. It is possible to operate in pitch-catch mode using a single transducer if the object to be inspected forms a closed path i.e. a circle. The single transducer transmits the signal, then its functionality swaps to receiver as the signal circumvents the pipe. However, care must be taken so that the transducer does not move out of range of the returning wave(s) (reflected and/or round-trip).

- Through-Transmission mode uses two transducer, one on each side of the object being inspected, Figure 1.10(c). Through-transmission is not applicable to in-line pipe inspection since the outside of the pipe is not accessible.

The ORNL EMATs are configured in the pitch-catch mode with an arc length of approximately 12-inch between the outside edges of the receiver and transmitter EMATS**. The input signal to the transmitter EMAT is a windowed frequency burst from the tone-burst card. This frequency burst, or driving frequency, controls which mode the SH-wave is generated at [16, 19]. The driving frequency is tuned to excite SH mode 1 (SH_1). The frequency to achieve SH_1 differs from pipe to pipe and is dependent upon the wavelength and material velocity. Frequency, wavelength, and velocity are all related via Eqn. (1.2),

$$f = \frac{v}{\lambda} \tag{1.2}$$

**The arc length is given as an approximate because the EMATS are on spring loaded struts so as to keep the EMATs pressed against the inside pipe wall and therefore vary.

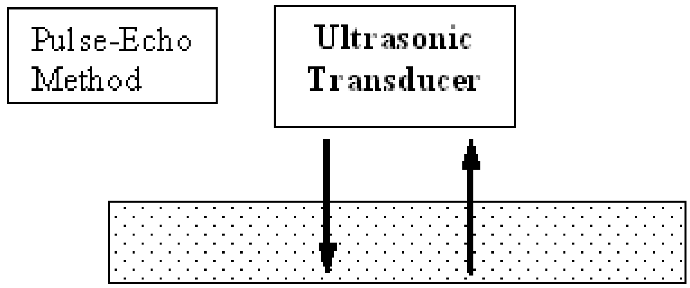

(a) Pulse-Echo configuration

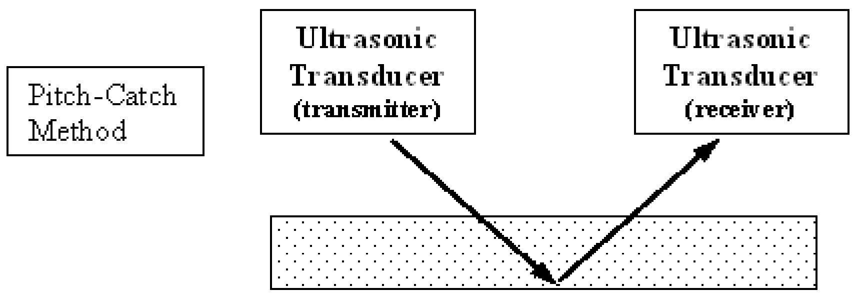

(b) Pitch-Catch configuration

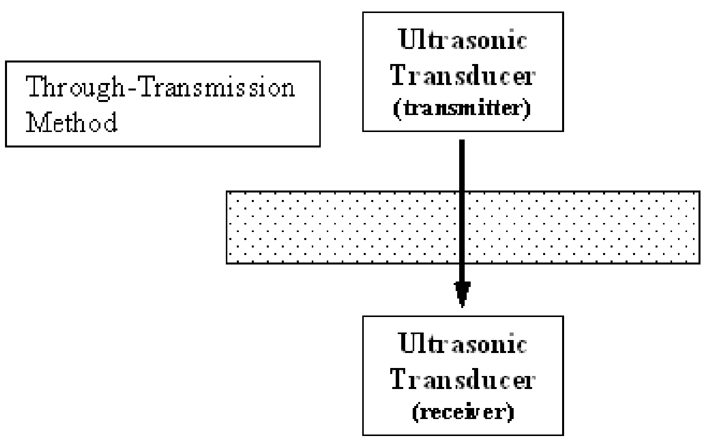

(c) Through-Transmission configuration

Figure 1.10: Ultrasonic transducers are generally configured using one of the three illustrated methods.

where,

f frequency,

v velocity of sound in the material,

λ wavelength.

The wavelength is determined by the spacing of the permanent magnets in the EMAT and so is fixed. The material velocity depends on the thickness and other properties of the pipe and is constant for a given type of pipe (i.e. given wall thickness, steel type, etc). The frequency of the tone burst must be adjusted to excite the SH_1 mode of a pipe based on the thickness of the pipe wall, since the wavelength can not be changed and the material velocity is also a constant. There is an important caveat with regards to the material velocity being a constant. If the thickness of the pipe wall changes due to any sort of metal loss defect or mechanical damage, then the material velocity will change. This in turn comes back to affect the driving frequency, in that with the fixed wavelength a change in the material velocity precipitates a change in the frequency of the ultrasonic wave. The "size" of this change in the material velocity, and thus change in frequency, is related to the size (volume) of the defect [16]. One reason that the SH_1 mode was selected was based on the hypothesis that since a higher mode can decay to lower mode a defect in the pipe would precipitate a drop to SH_0. During the research and experiments conducted prior to the construction of the ORNL PIG, it was discovered that in stationary situations different types of defects each effected the wave structure in different way that could be used to identify the type of defect [18, 21]. In summary, SCCs have such small volumes that they have little effect upon the frequency and do not cause the ultrasonic wave to decay from SH_1 to SH_0. This is why feature analysis and classification play the major role in actually identifying defects.

1.5 ORNL Sensor System

While in the initial work to detect SCCs using EMATs it was found that the actual type (pitting, corrosion, or SCC) of defects could be determined these EMAT data was collected using a stationary hand placed pair of EMATs. Since then the rolling platform shown in Figure 1.11 was designed and constructed. The EMAT sensors, electronics, computer, and data acquisition systems were the same as used in the stationary test with a few minor additions. The elements of the ORNL PIG divided into either hardware or software components and are described in the following two sections.

1.5.1 Hardware

The PIG is a rolling frame designed to fit into 30-inch diameter pipes. It also can be converted to fit into 26-inch diameter pipes. The frame holds an industrial computer, an electronics box, a position resolver, and the spring loaded support assembles for the EMATs. The industrial computer contains dual Intel Xeon processors, a Datel PCI-417F data acquisition card, and a Matec TB-1000 gated amplifier tone-burst card. Both the Datel and Matec cards plug in to the PCI bus of the computer. The Datel card is capable of a sampling at 10 MHz per channel with 14-bit resolution on each of its four channels [22]. Only two of these channels are used in the system and so the two channels are sampled using a 5 MHz sampling rate. One samples the position resolver and the other samples the received signal from the receiver EMAT. The Matec tone-burst card creates the excitation signal at the driving frequency that is sent to the transmitting EMAT. The tone-burst card is designed specifically for use in non-destructive ultrasonic testing. It is capable of producing a gated sinusoid in the frequency range of 50kHz to 20MHz with a peak output power of 450 Watts at 5 MHz [23]. The majority of the time we use a driving frequency in the range of 200 KHz to 300 KHz. One of the tone-burst card features is a dedicated "initialization" output. This output is a scaled down version of the signal sent to the transmitter EMAT. The "initialization" signal and excitation signal are sent simultaneously allowing the data acquisition to record during the entire transmit-receive process of the EMATs. The Matec card also contains a built-in amplifier which the received signal is passed through after going through the pre-amplifier.

In addition to the hardware installed in the on-board computer, there is a pre-amplifier, matching networks, and terminal block for the data acquisition connections. These items are contained what is labeled as the signal conditioning unit in Figure 1.11. The reason for using both the pre-amplifier in the signal conditioning box and the amplifier built into the tone-burst card is that the initial pulse to the receiver is 300 volts peak-to-peak and 1.5 amperes but the received signal is in micro-volts. The pre-amplifier has a fixed 50dB of gain and the built-in amplifier is capable of a maximum gain of 70dB. The gain of the built-in amplifier is tuned so that under normal conditions in the pipe a strong, well defined signal is sent to the Datel

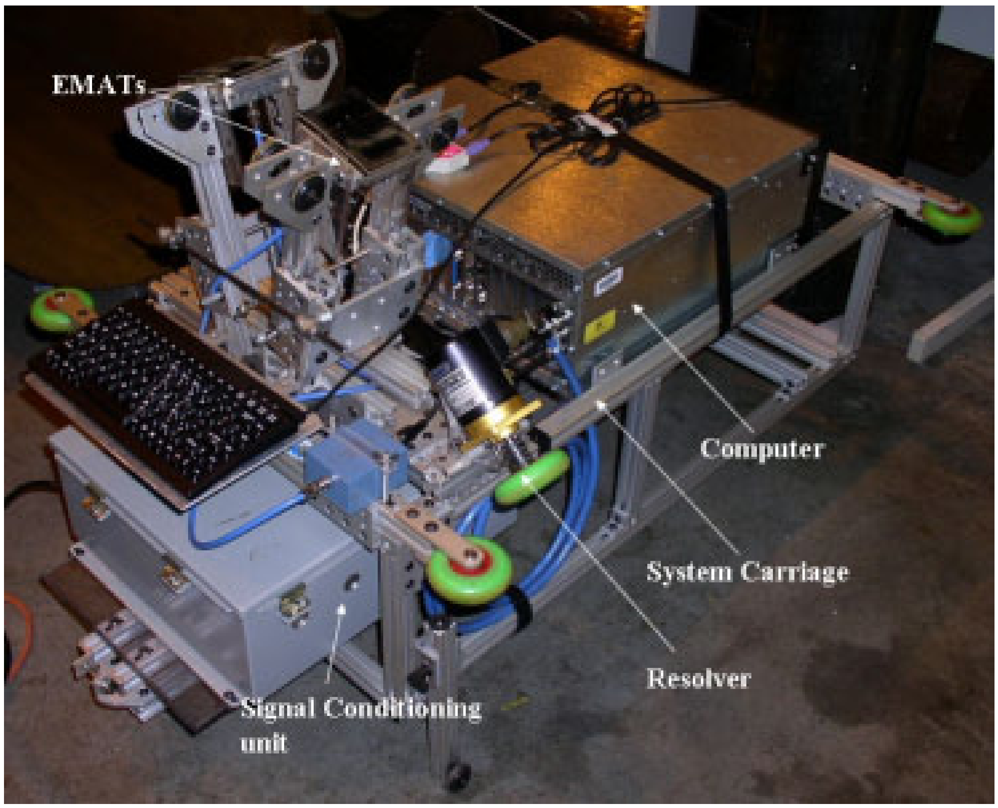

Figure 1.11: The ORNL sensor platform used to collect data from the EMAT sensors while moving through a pipe.

card. Usually, the built-in amplifier is tuned to between 42dB and 48dB gain. The mechanical resolver used for position measurements is attached on a spring loaded mount so that the wheel on the resolver's shaft maintains contact with the pipe wall. The resolver has its own "control" unit which converts the analog resolver count in to a digital count that is passed to the data acquisition system. There are keyboards attached at both ends of the PIG so that the Labview data acquisition program can be started and stopped without removing the PIG from the pipe. Power for the computer is provided via an extension cord connected to a power strip attached to the PIG's frame.

1.5.2 Software

Software used with this project can be divided into two categories, "on-line" software and "off-line" software. The on-line software runs on the computer integrated in to the ORNL PIG. The off-line software is software used for the project which is not on the PIG's computer. The computer on to the ORNL PIG is running the Windows 2000 Professional operating system. The National Instruments Labview software is used to control the Datel data acquisition card and save the data to hard disk. The Matec tone-burst card has its own software interface for adjusting the gain of its built-in amplifier, the frequency of the windowed tone-burst, the duration of the window, and the power output. Once the tone-burst card is enabled it begins outputting a 22 microsecond burst every 12 milliseconds, until it is disabled via its software interface again. The exact duration and "timing" of one burst-sample cycle is shown in Figure 1.12. Once a series of experiments are completed the PIG's computer is connected to the local area network using an ethernet cable and the data is transferred to a workstation. The actual data processing, analysis, and visualization is performed on the workstation using the off-line software, which is Matlab.

1.6 Contributions

Two years of development on this sensor system had been conducted prior to my involvement. So much of the foundation that my research is built upon had already been completed or at least started. This includes the design or purchase of hardware; construction of the rolling test platform; the data acquisition software (Labview program), the mother wavelet to be used and how many levels the wavelet decomposition

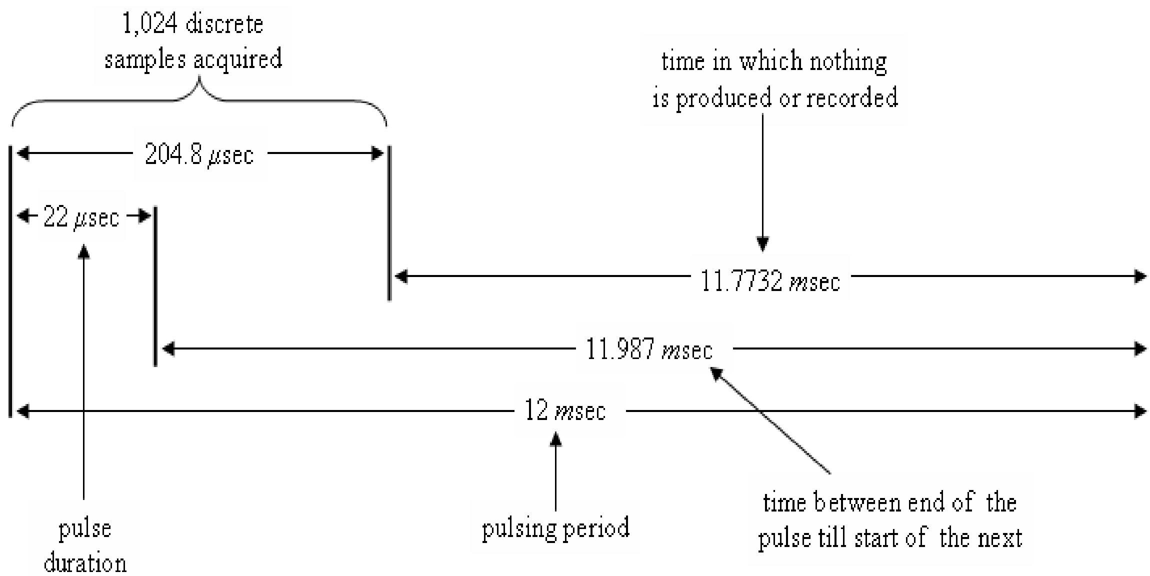

Figure 1.12: The timing and duration of the events making up one burst-sampling cycle are shown here. The times listed in the diagram are accurate, but the diagram is NOT to scale.

would go. Also, what portion of the EMAT signatures to be used in the wavelet decomposition; the initial redundant data reduction and conversion to meaningful position. The use of the Mahalanobis distance for classification, and the "original" feature set had been selected. This work was done by the original members of the project: Dr. Venugopal K. Varma (the primary investigator), Dr. Stephen W. Kercel, and Mr. Raymond W. Tucker, Jr. However, at the time of my arrival the research team working on the natural gas pipeline inspection project consisted of only Dr. Varma and Mr. Tucker. As a member of this research team I eventually became the primary researcher dealing with the signal processing, feature selection, and classification algorithms. My specific contributions are of the evaluation and addition of several new features along with the removal of several un-useful features; adding PCA+LDA to the original classification algorithm; the collection of multiple data sets from both decommissioned pipe sections with real SCCs and pipe sections with synthetic SCCs. During the years I worked on this research the amount of data available for testing improvements to, as well as statistically validating, the feature set and classification algorithm was more than tripled. I developed the criteria for distinguishing between SCC responses and anomaly responses in the Mahalanobis distances from moving data. Most importantly, I created the training set that is the key to the improved classification accuracy. The training set contains a group of no-flaw features that are used to perform the final step of the classification algorithm. This group of no-flaw features is the first and only group that has successfully worked on multiple scanlines, on multiple pipes.

1.7 Document Organization

The remainder of this thesis, documents the details of the methods, algorithms, and validation of the research discussed in this thesis. Chapter 2 presents the preprocessing steps, the feature extraction, the original feature set, and the final feature set. This is followed by an explanation of the discriminant analysis techniques and classifier used in either the original classification algorithm, the final classification algorithm, or both, in Chapter 3. Experimental results from this research are provided in Chapter 4. These experimental results present the significant improvements achieved as a result of this research by comparing the results from multiple trials of multiple test in which the original and final feature sets were used in conjunction with both the original and final classification algorithms. Finally, we conclude in Chapter 5 with a summary of the achievements as well as the recommendations for future work.

Chapter 2

Preprocessing and Feature Extraction

The data collected from the EMATs and the resolver must undergo several preprocessing steps before it is suitable for use. This is necessary so that the EMAT and resolver data are uniformly formatted and to eliminate the large amount of duplicate data collected from the resolver. The resolver data collected is straight forward, however the EMAT signals are more difficult to understand and so will be explained in the next section to provide a common baseline for the material on feature extraction in Section 2.3.

2.1 EMAT Signals

In ultrasonic NDT, the collected data/signals can be represented using a number of formats specific to the ultrasonic NDT field. There are three defacto standard formats known as A-scan, B-scan, and C-scan. These formats provide representations that correlate/orient the signal(s), time, and the position on the scanned object.

An A-scan is the actual received signal. This is commonly described as the RF signal and is either displayed as received, Figure 2.3, or as a rectified version of the received signal. The A-scan signals are what are referred to as signatures through out this thesis. We do not rectify our A-scans, i.e. EMAT signatures, since this would decrease the information of the signatures and thus the information in the features. An A-scan connects time (x-axis) to signal amplitude (y-axis). When an ultrasonic inspection is performed the sound wave travels through the material and is reflected by the boundaries of the object. For now lets just examine an idealized situation of just one tone-burst on a pair of **non-EMAT** ultrasonic transducers in the pitch-catch configuration, Figure 2.1. The wave is shown as being "separated" in to three different waves propagating through the pipe wall for visual purposes. The basis for this "splitting" analogy comes from the fact that the ultrasonic wave is in the actual atomic lattice of the material and so the "layer" a reflection occurs in can propagate that reflected wave. In this idealized example, the received A-scan signal is shown in Figure 2.2.

The basic ideas behind the idealistic case hold true for received EMAT signatures as well, but with several key differences. First take a look at the real EMAT A-scan shown in Figure 2.3. The first thing you probably noticed is that there is only one "wave packet" after the initial pulse instead of three as in the idealistic A-scan. In our case where the ultrasonic transducer is an EMATs there is no "front-wall" or "back-wall" reflections of the excitation from the transmitter EMAT, because the generation of the ultrasonic wave is actually taking place in the "near-surface" of the wall (the inside face of the pipe wall) where the eddy-currents are induced by the EMAT [19] and traveling through the pipe wall circumferentially and so does not "impact" the back-wall and reflect as with traditional ultrasonic transducers. Next, since the SH_1 wave is created in the pipe wall at the transmitter and propagates past the receiver, the one "wave packet" present in the EMAT signatures, Figure 2.3, is the actual ultrasonic wave as it passes the receiver, not a reflection as in the idealized example shown previously. Finally, as mentioned in Section 1.4.2, SCCs are so small

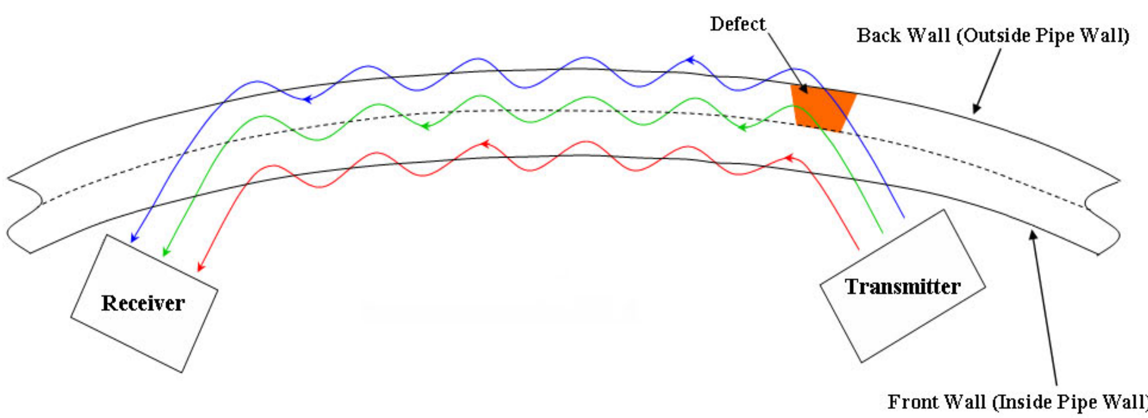

Figure 2.1: Ideal situation and propagation of a single tone-burst between a pair of ultrasonic transducers in the pitch-catch configuration in the presence of a defect.

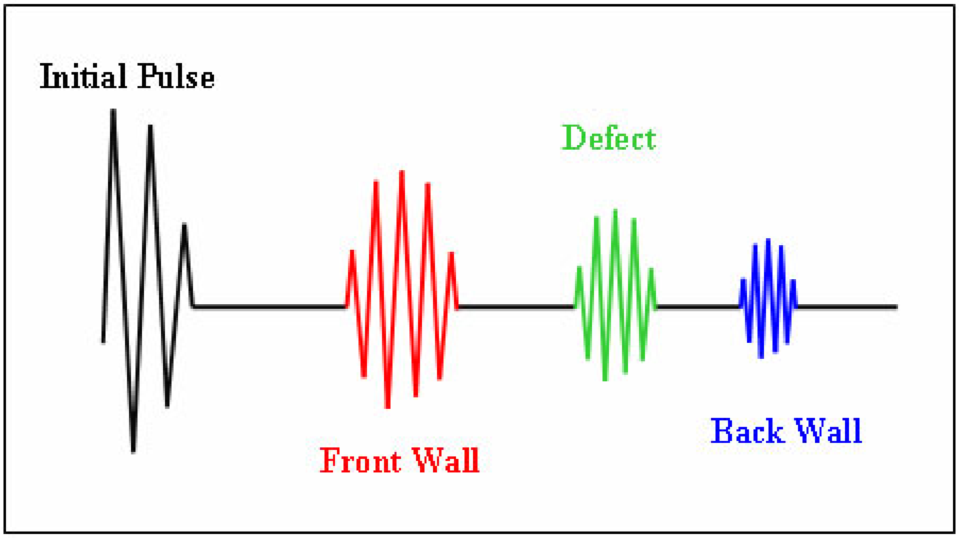

Figure 2.2: This is the idealistic A-scan signal resulting from the situation in Figure 2.1. Keep in mind that the initial pulse is not actually transmitted through the pipe, it is a scaled down copy of the actual pulse to the transmitting ultrasonic transducer passed directly to the data acquisition system where it triggers the acquisition and becomes pre-pended to the signal received by the receiving ultrasonic transducer [24].

that they have little affect on the signal which in this case means the defect does not create a reflection. However, defects (SCC, corrosion, pitting) do have an effect on the wave, which the features capture. One point about the EMAT signatures that merits reiterating is with respect to the initial pulse. The initial pulse is a scaled down version of the windowed tone-burst to the transmitting EMAT. The full-scale pulse and the reduced version are sent simultaneously to the transmitter EMAT and the data acquisition respectively. So the initial pulse in the A-scans (signatures) occurs when the time is zero. It is reasonable to state that the time for the EMAT to create the ultrasonic wave in the pipe wall and the time for the data acquisition to begin sampling are equivalent and negligible.

While an A-scan shows amplitude and time in a two-dimensional plot, a B-scan shows time, position (distance), and amplitude in a three-dimensional representation. The best way to understand this is with a simple analogy. Consider a single A-scan to be represented by a single playing card. For our purposes lets say this deck of cards has 52 numbered one through 52, and that each card has only a single number on its face. If you hold a single card as you normally would, you see the number; we will say it is number one for the purpose of this analogy. This represents the first A-scan signature of a scanline. Now, turn the single playing card on its edge and place the

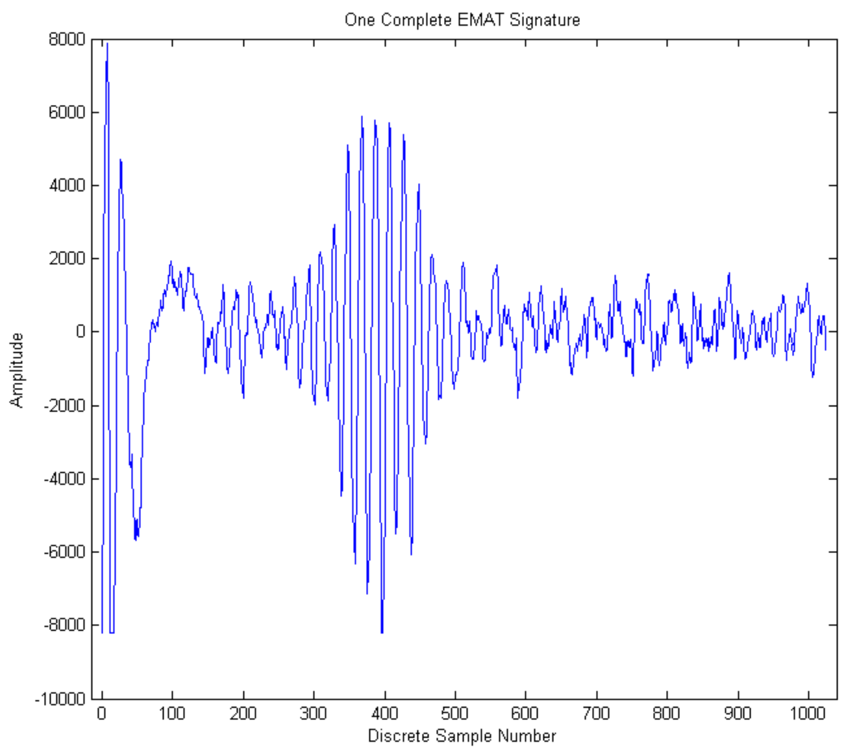

Figure 2.3: A single EMAT signature, A-scan, captured while moving through a pipe.

number two card on its edge to the right of the first card. Repeating this until you have all 52 cards on their sides in ascending order from left-to-right (you are looking at the side of a deck of cards), this is a B-scan. Each A-scan is collected at a known distance from the starting point of the scan. When these "on their edge" A-scans are stacked in order by the position where the A-scan was collected, a B-scan results. The whole "translation" from an A-scan to a B-scan is shown in Figure 2.4.

C-scans are more applicable to planar objects, since a C-scan is a three-dimensional matrix of A-scans where the z-axis is time/depth and the $x - y$ axes refer to the actual $x - y$ position on the test object's face. Semiconductor packages are a situation where the C-scan format is ideal. By picking a specific range of depth the response to the ultrasonic wave at individual layers of the semiconductor can be seen [24]. Understanding the "layout" of an A-scan and how an A-scan signatures correlates to the data from a full scan of a scanline (a B-scan) will make the explanation of the signature quality check procedure in Section 2.2.3 easier to follow.

2.2 Preprocessing Procedures

The data collected during the scanning of a pipe requires a few preprocessing steps before it is ready for feature extraction and classification.

2.2.1 Convert Position from Resolver "Units" to Inches

The data collected from the resolver is simply the current value of the counter. As the resolver's shaft turns it increments the count. When the counter reaches 8,192, the shaft has made a full rotation and the counter rolls back around to zero. Since, the ORNL PIG can be pulled from either end the counter may count down from 8,192 to zero or up from zero to 8,192. Regardless of the direction of the count (up or down) the resolver data must be converted in to meaningful position data. The data acquisition channel sampling the counter value is sampled at the same rate as the channel sampling the receiver EMAT's signal. This means that for the 1,024 samples taken for each signature there is also 1,024 counter values sampled and all in 204.8 microseconds (μs), as shown in the timing diagram Figure 1.12. In such a short amount of time the counter only changes if it was in the process of changing at the moment the sampling occurred. For this reason the majority of the data collected from the resolver is redundant and so the first step in the preprocessing is to take the

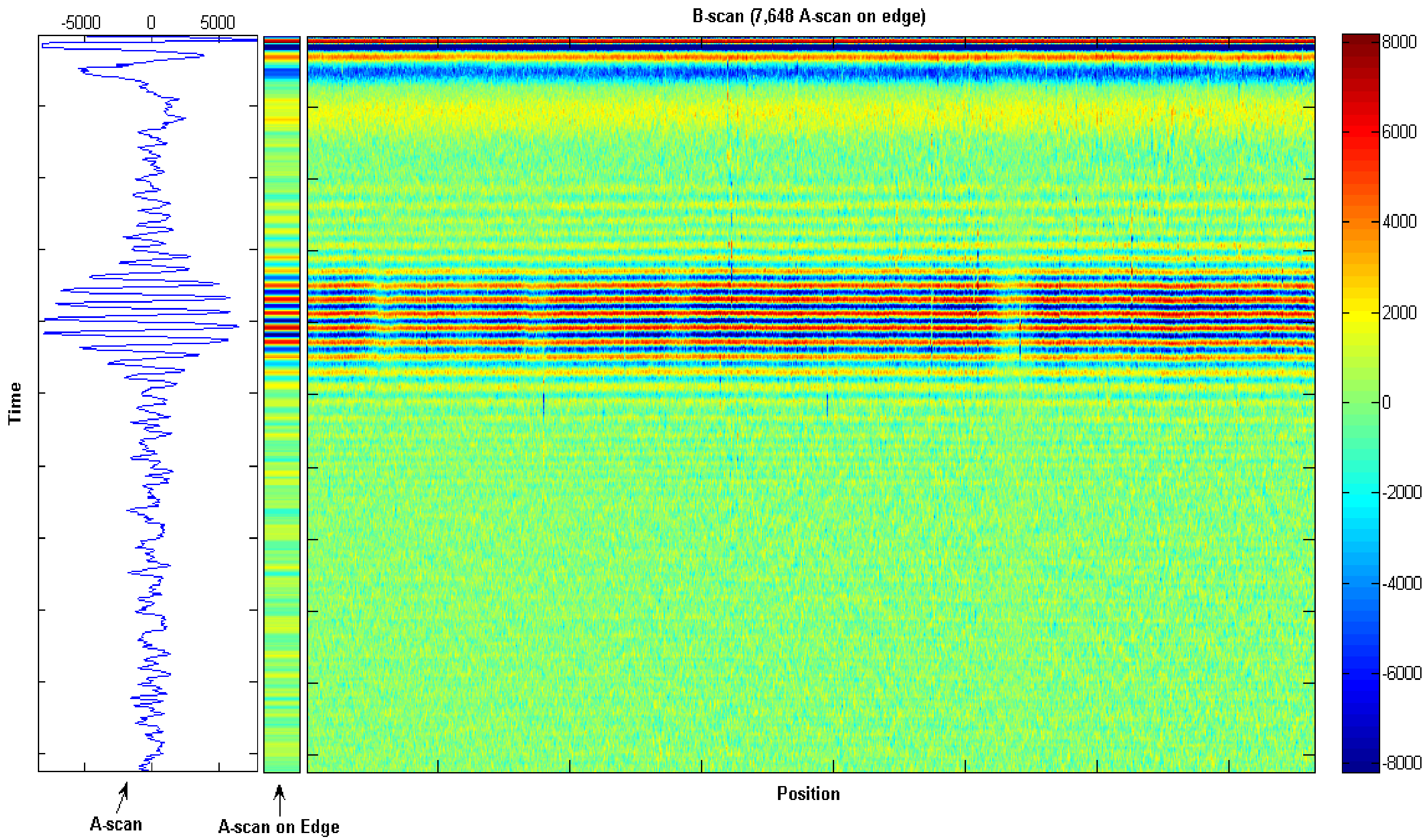

Figure 2.4: On the left of the figure is a single A-scan, to the right of which is the same A-scan in its B-scan form followed by the B-scan for the entire scanline from which the A-scan originated.

mean value of the 1,024 counter readings for one signature and create a new “pairing.” The “pairing” is the 1,024 samples of the signature and the mean of the 1,024 counter samples. These “pairings” are what will be used by all following operations.

The next step is to perform a simple quality check on the EMAT signatures to remove the corrupted ones, which is discussed in Section 2.2.3. The position values that corresponded to the signatures removed by the quality check are removed as well. At this point the position data is still just the mean counter value at the time a signature was taken and must be converted in to meaningful units. The counter wraps over numerous times during a scan so the first step is to unwrap the count values so that the values are monotonically increasing. Attached to the resolver shaft is a wheel which actually makes contact with the pipe wall. A standard rollerblade wheels was chosen and attached in our case. Then the circumference of the wheel that is attached to the resolver shaft is used to convert the count into an actual position in inches.

$$\text{Position [in inches]} = \left(\frac{\text{Monotonically Increasing Resolver Count}}{\text{Maximum Resolver Count}}\right) \times \text{Max Wheel Circumference} \tag{2.1}$$

When the PIG is placed in a pipe the EMATs are already four to seven inches in from the pipe’s end. This initial offset is measured and recorded so that the collected position data will match the real-world position when the offset is added. However, to accommodate the variability of a pipe’s geometry, the resolver is on a spring loaded support to keep resolver’s wheel pressed against the pipe wall. Because of this the resolver is always at a slight angle that causes the resolver wheel to not roll precisely on its outermost edge. So the actual “rolled-on” circumference is less than the maximum circumference used to convert the resolver count to inches. This can be seen in Figure 2.5 by comparing the rust “stains” on the front and rear guide wheels, which are rolling on their maximum circumferences to the “stain” on the resolver wheel. This error was corrected by adjusting our data collection procedure to include measuring the ending offset, in addition to the initial offset. The starting offset and stopping offsets are subtracted from the full length of the pipe to find the actual distance traveled. The actual total distance traveled divided by the total distance traveled according to the resolver gives a position correction factor, Eqn. (2.2).

$$\text{Position Correction Factor} = \frac{\text{Actual Distance Traveled}}{\text{Resolver's Distance Traveled}} \tag{2.2}$$

The position data is then multiplied by the position correction factor to correct for the resolver's wheel rolling on a smaller circumference. Finally, the true position at which each signature was acquired is found by taking the position data in inches, multiplied by the position correction factor, plus the starting offset, plus half the width of the EMAT head, Eqn. (2.3). The reason half the width of the EMAT head is added is that the center of the resolver shaft and the center of the EMAT heads are all aligned with one another. So the resolver yields the position of the center of the EMATs but the starting offset is measured to the outside edge of the EMAT head not the center.

$$\begin{aligned}\text{Corrected Position} = {} & \text{Position Data}_{\;[in inches]} \times \text{Position Correction Factor} \\ & + \text{Starting Offset} + \text{Half the Width of the EMAT Head}\end{aligned} \tag{2.3}$$

2.2.2 EMAT Signature Corruption

There are a variety of things that affect the quality of the collected signatures, such as debris build up between the EMAT head and pipe wall, an out of round pipe, loss of synchronization in the data acquisition, and so on. All of these things are sources of signature quality issues and can be placed into one of two categories: coupling issues or electronics issues. Coupling issues refers to the electromagnetic coupling between the EMATs and the pipe wall. Put in the simplest terms possible, coupling issues boil down to "what is going on between the face of the EMAT and the face of the inner pipe wall." What follows is a brief explanation of the issues that cause the mass majority of the corrupted signatures.

Coupling Related:

- When the *roundness of a pipe* section has become more oval than circular the gap between the EMAT heads and the pipe wall is no longer uniform. The active face of the EMAT heads were designed as arcs to fit the curvature of a 30-inch diameter circle. We have seen this cause the gap, which is nominally a

Figure 2.5: The spring loaded resolver mount is shown here. Also visible in this image are the rust "stains" that give an indication that the resolver wheel does not roll on its maximum circumference (compare the rust strips on the guide wheels to the rust strip on the resolver wheel).

uniform one to three millimeter gap, shrink till the center of the EMAT head is touching the pipe wall while the outer edges have quarter inch gaps.

- Certain situations and types of *debris on the inside pipe wall* can cause the spacing rollers to travel over the debris instead of on the pipe wall. This increases the gap between the EMAT head and the pipe wall which degrades the coupling and attenuates signal transmission. One example of an attenuating type of debris are delaminations (flakes) that are not knocked loose from the wall as the EMATs begin to pass by and so cause a second "air gap." Figure 2.6 shows a fairly typical inner pipe wall and the rust, scale/flakes, and such that forms. A situation we encountered where debris effected the spacing rollers was a large area of caked on dirt left behind by muddy water running through the test pipe and slowly drying, leaving a continuous patch of dirt firmly adhered. The spacing rollers were actually rolling on the caked on debris, which absorbed the signal from the transmitting EMAT as well as increased the gap to the pipe wall.

- The rare earth permanent magnets plus the magnetic field produced when the coil is energized in the EMAT heads causes small particles of *magnetic debris to build up on the EMAT head*. In most circumstances this debris build is kept to a minimum by the movement of the PIG. The spring loaded struts press the spacing rollers against the pipe wall. Additionally, the strong magnetic fields (permanent and pulsed) of the EMAT heads add to the strength of "bound" between the pipe wall and the EMAT head. These properties ensure that the space between the EMAT head and the pipe wall is fairly constant, so small flakes and fragments that come off and stick to the magnets are pushed off as the debris contacts the rough pipe wall, as more clearly shown in Figure 2.7. In some cases though so much debris is coming off the pipe wall that it cannot be scraped clean fast enough and so the debris pushes the EMAT away from the wall. Another situation similar to this is when a large scale/flake comes off as a whole and because of its large surface area (compared to the dust normally attracted to the magnets) combined with its thinness (it is in the air gap between the EMAT's face and the pipe wall) it is "stuck" to the EMAT head for the duration of the scan.

Electronics Related:

Figure 2.6: This was taken from inside a 30-inch diameter test pipe containing real SCCs. The image is of an approximately two feet wide three feet tall area of inside pipe wall.

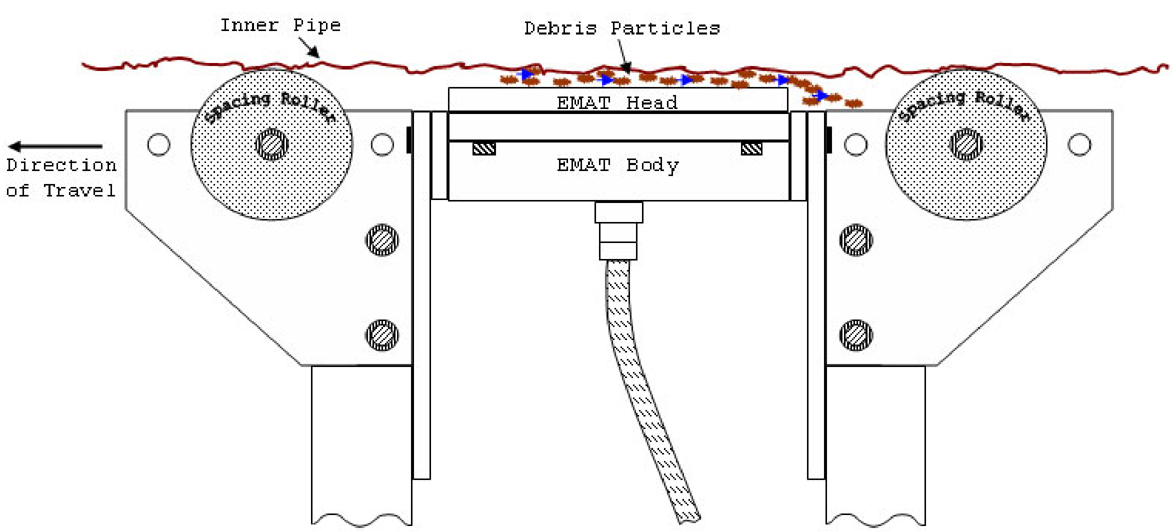

Figure 2.7: This diagram shows the natural "self-cleaning" action resulting as the EMAT travels across the rough pipe wall.

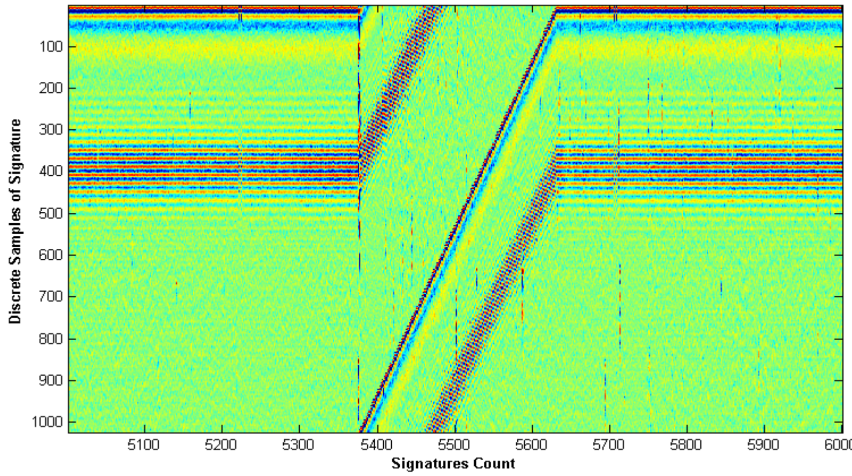

Figure 2.8: This B-scan image shows a loss of 250+ signatures. Notice the smearing of the initialization pulse at the top and the shear wave envelope in the middle indicative of a loss of time synchronization.

- Signatures are inevitably corrupted due to *saturation of the analog-to-digital converters* in every scan. Usually the cause is related to either a section of pipe were the wall has thinned (due to corrosion or such) or the pipe is out-of-round and the EMAT head touches the pipe wall, eliminating the air gap completely. In the cases where the pipe wall has thinned this decreases the attenuation of the signal, which in turn means the received signal is stronger than the "normal" signal at which the gain was tuned and so the analog-to-digital converter is saturated.

- Rarely a momentary *loss of synchronization in the data acquisition* occurs causing the timing for gathering the samples of a signature to be skewed. When an un-synch occurs usually a two hundred to five hundred signatures are involved an are a total loss as shown in Figure 2.8. These un-synchs occur very rarely since the wiring to the receiver EMAT and the transmitter EMAT were isolated as much as possible. However, the cause of the un-synchs is still unknown, since they occur so rarely they have not been isolated to any particular activity.

- There are also several *electrically based corruption sources* that regularly occur but have not been identified. These issues include 180° out of phase signatures and signatures that appears to be on a sinusoidal carrier per say. These two types of signature corruption as well as a un-synchronized signature and a normal signature are shown in Figure 2.9 for comparison.

2.2.3 Signature Quality Check

There are always "bad" signatures collected in every scan, even on a new pipe there are bad signatures collected. It is just an unavoidable consequence of the harsh signal environment present as the EMATs slide past the rough surface of the inner pipe wall with only one to two millimeters of clearance. Since there is a high degree of variation in "good" EMAT signatures, the "bad" signatures that are removed are substantially different from other signatures regardless of their class (flaw, no-flaw). The signatures are cleaned in a two step process.

The first step removes the majority of the bad signatures based on the percentage of "energy" in the head and/or tail of the signature, with respect to the energy contained in the excitation section, Figure 2.10. Since the value of each sample point is an amplitude, the dot product of the vector points with itself returns the sum of elements of the squared. By taking the square root of this dot product results, the final scalar result is the sum of the absolute values of the amplitudes, thus a very energy-like measure. The fraction (percentage before multiplying by 100) of the excitation "energy" contained in the head and tail sections are calculated using Eqn. (2.4) and Eqn. (2.5) respectively. Since all of the "energy" in the head, signal, and tail sections of the signature comes from the excitation pulse, the percentage contained in the head and tail are fairly consistent regardless of the signature's class.

A signature is determined to be bad if the head fraction, the tail fraction, or both is greater than or equal to their respective thresholds. These thresholds were set initially to 0.5 (50% of the excitation energy) each. However, there were still to many blatantly corrupt signatures being passed, so the thresholds were adjusted to determine if a more through cleaning could be had using this method. The thresholds were adjusted through trail-and-error using a set of signatures which had previously been hand cleaned and therefore the exact indices of the signature that should be removed were known. In the end the head fraction threshold was changed to 0.61 (61% of the excitation energy) and the tail fraction threshold was left at 0.5 (50% of the excitation energy).

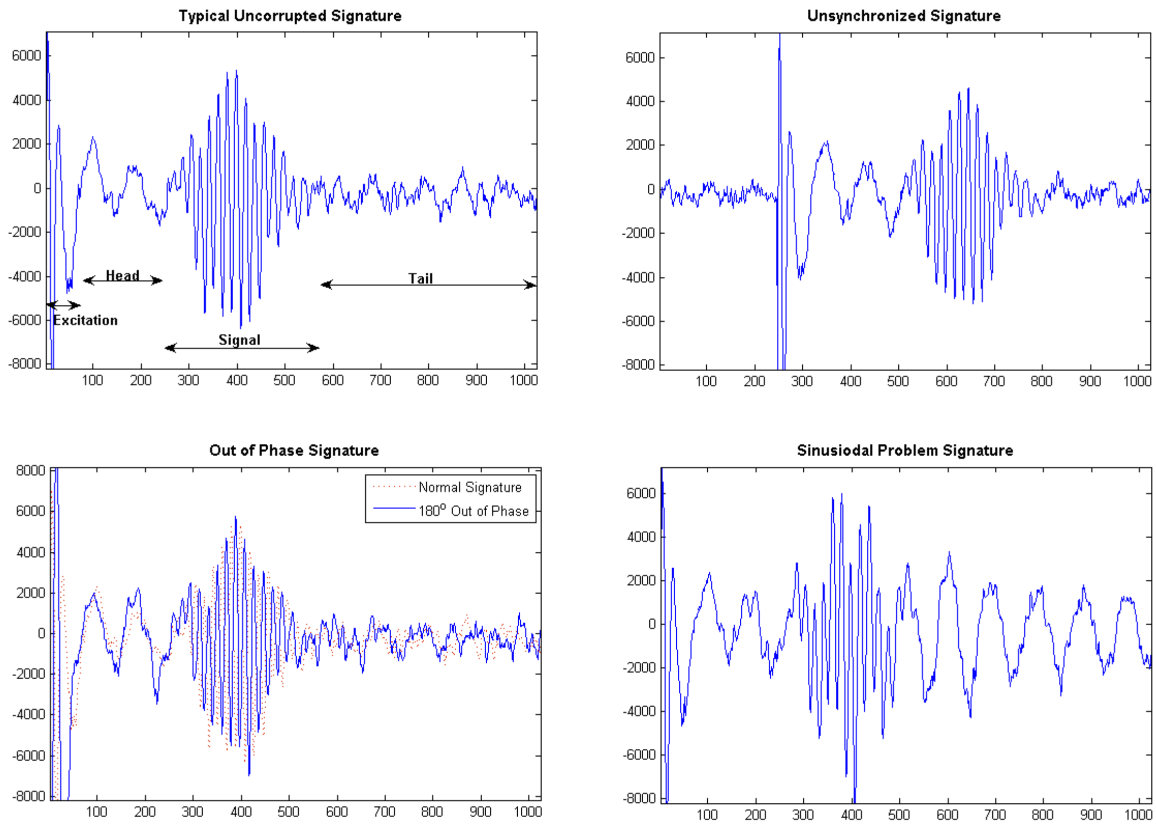

Figure 2.9: The signatures shown in these images illustrate several of the more commonly seen types of corrupted signatures as well as one signature from the rarely seen un-synchronized acquisition problem.

$$\text{Head Fraction} = \frac{\sqrt{\mathbf{H} \cdot \mathbf{H}}}{\sqrt{\mathbf{E} \cdot \mathbf{E}}} \tag{2.4}$$

$$\text{Tail Fraction} = \frac{\sqrt{\mathbf{T} \cdot \mathbf{T}}}{\sqrt{\mathbf{E} \cdot \mathbf{E}}} \tag{2.5}$$

where,

- $\mathbf{E}$ is the vector containing the amplitude value of each discrete sample point in the excitation section,
- $\mathbf{H}$ is the vector containing the amplitude value of each discrete sample point in the head section,
- $\mathbf{T}$ is the vector containing the amplitude value of each discrete sample point in the tail section.

After this fractional energy cleaning, there still remains one type of corrupt signature that cannot be removed using the head and tail energy fraction method, the 180° out-of-phase signatures. To remove the 180° out-of-phase signatures the median of the signatures is calculated using the set of signatures that remain after removing the signatures identified as bad by the head-tail cleaning method. These signatures are then correlated to the median signature. A perfect correlation results in a correlation value of one. A completely inverse correlation results in a negative one correlation value. The correlation values are then thresholded so that any signature with a correlation value less than 0.2 will be removed. Only the 180° out-of-phase signatures have correlation values less. To test the robustness of the correlation threshold value the correlation cleaning was done before the head-tail cleaning, even then the 180° out-of-phase signatures were the only signatures with correlation values less than the 0.2 threshold value. In fact, with just the 180° out-of-phase signatures removed the average correlation value for most of the tested scans were between 0.9 and 0.93. When the head-tail cleaning and the out-of-phase cleaning have been preformed the average correlation falls between 0.93 and 0.95. This is why correlation has not been used as a feature.

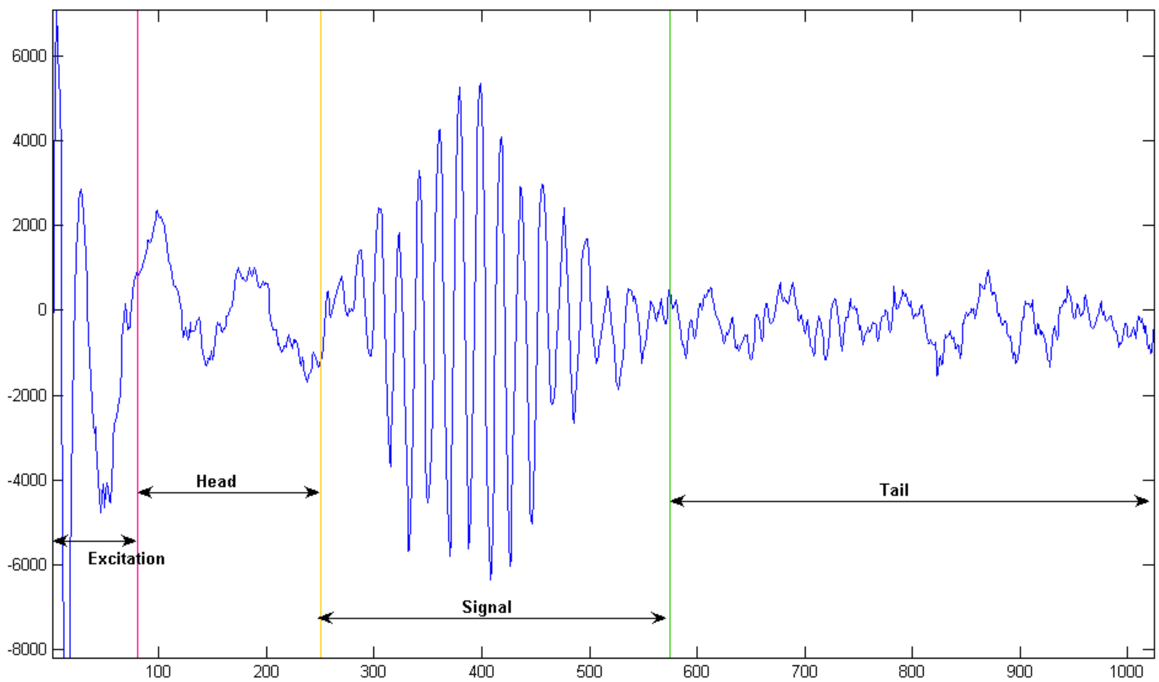

Figure 2.10: The signal is divided in to four sections: the excitation, the head, the signal, and the tail. The energy in the head and tail sections are found as a percentage of the energy in the excitation section.

2.3 Feature Extraction

The actual features used for the classification are extracted from a wavelet decomposition of each EMAT signature. Each full signature is composed of 1,024 discrete sample points. The full signatures are used in all steps until it is time to perform the discrete wavelet transform. At this point a continuous range of 512 points is extracted from the 1,024 point signatures and is the input to the wavelet decomposition. This 512 point section is roughly the 1,024 point signature with the excitation and half the head section removed from the beginning (the first 26% of the signature) and the last half of the tail (the last 23% of the signature) removed also. This section, Figure 2.11, contains the critically important SH_1 "wave packet." A discrete wavelet decomposition will be performed on the 512 point signature section.

2.3.1 Discrete Wavelet Transform

The transient nature of the EMAT signals along with the harsh environment the EMAT signatures are collected in lead to the usage of a discrete wavelet transform (DWT) to decompose the signatures into sections from which features are extracted. Wavelet analysis was chosen over Fourier analysis based on the knowledge that the ultrasonic signals are transient, oscillating burst of energy. The Fourier basis functions, sines and cosines, perform poorly when used to represent transient signals [18, 21, 25]. Also as mentioned previously, SCCs do not cause a reflection of the guided wave because of there size, but do affect the shape of the signal. So it is key that these transient signals be well represented by the analysis method used to decompose them.

Two additional benefit of using a DWT are that the wavelet decomposition contains both frequency and time information (i.e. the time a frequency occurred at) and the energy preserved in each piece of the decomposed signal is solely represented in that portion of the decomposition. That is to say, there is no redundant energy. The sum of the energy contained in the decomposed signal is equal to the energy contained in the original signal i.e. there is no leakage. In the wavelet domain the information and energy are effectively proportional [25]. It is useful to think of the DWT as a perfect filter. Each successive filter in the bank divides the frequency range in half, passing the low frequency portion on to the next filter. These frequency bands are orthogonal and so the sum of the energy in the separated frequency bands sums to

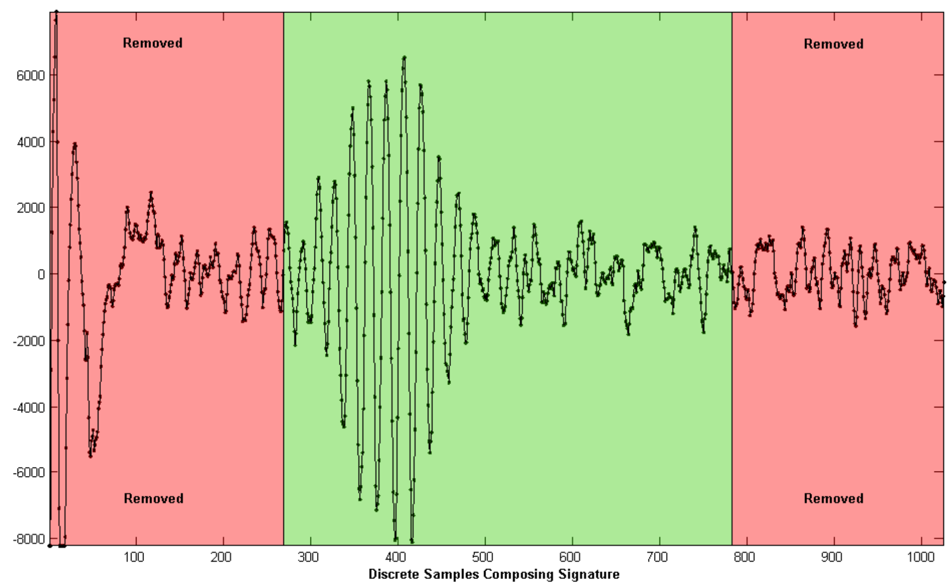

Figure 2.11: The 1,024 sample points of a signature cover more "time" than is necessary for feature extraction. So it is trimmed to the 512 point section shown in green. The excitation pulse does not contain any information about the area the SH_1 wave propagated through, since it is passed directly to the data acquisition by the tone-burst card. The last quarter of the signature is trimmed because it does not contain any information not contained by the portion of the "tail" that is retained.

the total energy contained in the full signal. There is no leakage as long as the basis function (mother wavelet) is an orthogonal function and the results of the decomposition accurately separates the signal in to sub-signals representing specific frequency bands [18, 25, 26]. The mother wavelet used for our DWT is a 58 coefficient Symlet wavelet. Using this mother wavelet each signature is decomposed to a "depth" of four layers.

The mother wavelet is scaled by a factor of two and time shifted until the "closest" fit to the signal being transformed is found. When this weighted sum representation is reached it has effectively divided the input signal's frequency content in half, as if it were passed through a perfect lowpass filter. The portion of the signal passed by this lowpass filter is called the approximation. The portion "rejected" by the lowpass filter (the high frequency content) is called the detail [18, 26]. An approximation component plus its matching detail component form one wavelet decomposition level. The approximate component can then be passed through the same procedure to from another set of components, as illustrated in Figure 2.12. Each level in the decomposition divides frequency content of the input signal, the original full signal or the level above's approximation component, in half. The mother wavelet is scaled and shifted progressively, separating out bands of frequency content each time a "fit" is found. In the end, signal under test can be fully represented by the weighted sum of these bands [18, 25]. For the remainder of this thesis the "parts" of the DWT decomposed signal are identified as Approx-4, Detail-4, Detail-3, Detail-2, and Detail-1, which also corresponds to the wavelet decomposition tree in Figure 2.12. Once the wavelet decomposition of the data set is completed we are ready to calculate the features of each decomposed signature.

2.3.2 The Features and Their Calculations

The features are the numerical representation of signature traits that are expected to allow a classification to be made as to whether the signature was collected over a defect in the pipe. The selection of features is the most difficult aspect of developing a classification algorithm. Ideally, potential features are chosen based on either the recommendations of experts in the application field, the previous research in the field, or both [27, 28, 29]. When the target application involves prototype sensors, in an experimental system, in what is essentially an entirely new field of application the

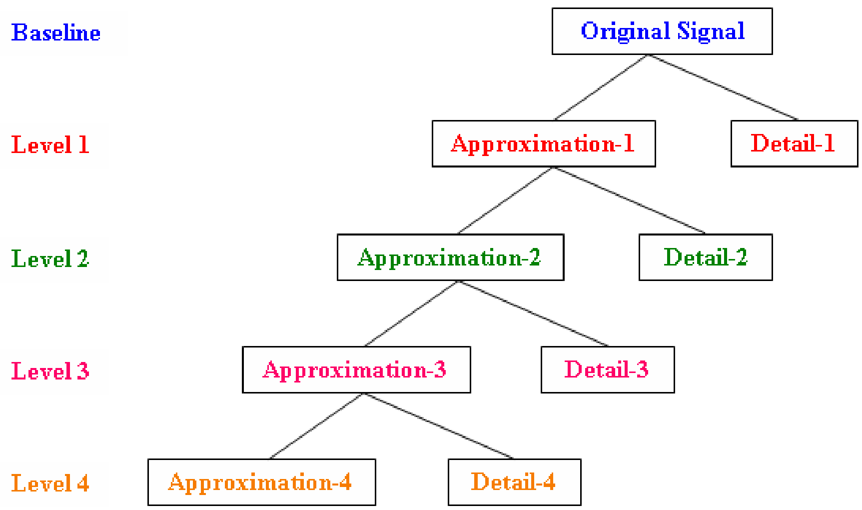

Figure 2.12: The decomposition "tree" of the input signal (EMAT signature in our case) at each level and the name of each retained level.

selection of features becomes a critical challenge. For example, traditionally amplitude is the primary feature used by NDT inspection systems that perform feature analysis to detect flaws [30]. This is regardless of whether the inspection system uses MFL or ultrasonics for inspecting pipes, plates, railroad track, or even semiconductors. However, the variable, transient nature, and noisiness of signature amplitudes has resulted in the exclusion of amplitude based features from our feature set.

There have been a net total of seven "unique" features used. Six of these were actually incorporated as part of the feature set at some point during the progression of the features set. The seventh, correlation with respect to a "good" set, provided such negligible information in even idealistic initial test, that it was never included in a "working" feature set. The reason for not including correlation as a feature was discussed in the last paragraph of Section 2.2.3. While a small number of "unique" features are used there is actual a much larger total number of features. This is because each feature is calculated for each wavelet level of a decomposed signature. For example, a single signature is decomposed in to five pieces: Detail-1, Detail-2, Detail-3, Detail-4, and Approx-4 (a four level wavelet decomposition). Next, we calculate the energy feature for each level as a percentage of the total energy in the signature i.e. energy in a single piece divided by the sum of the energy in all five pieces. Thus there are five energy features. In this way the utmost advantage is made of the DWT's ability to separate frequency bands without leakage.

The feature set has gone through several iterations over the course of this research. The overall progression of the changes made to the feature set are shown in a chronologically ordered table, Table 2.1, which shows each feature making up the feature set. We will discuss in more detail two of the feature sets in Table 2.1. The beginning feature set (original feature set) and the ending feature set (final feature set) since these were used to show the improvements achieved through this research.

The Original Feature Set

The original feature set that was built upon during this research consisted of 13 features. The following list gives the feature name, a description of it, the wavelet levels that it is calculate for, and the equation for the actual calculation. The equations are formulated for calculating the 13 features a single signature at a time. To calculate the features for an entire data set, the calculation should utilize a loop that increments through the signatures one at a time, calculating the 13 features each time.

Table 2.1: **The chronological progression, from left to right, oldest to newest, of the feature set. The blue feature names are newly added features to the "working" feature set at the time. The red struck-through feature names were removed from the "working" feature set at that time.**

	"Original" 13 Features		20 Features		25 Features		30 Features	"Final" 25 Features	
1	Approx-4 Energy		Approx-4 Energy		Approx-4 Energy		Approx-4 Energy	Approx-4 Energy	*1*
2	Detail-4 Energy		Detail-4 Energy		Detail-4 Energy		Detail-4 Energy	Detail-4 Energy	*2*
3	Detail-3 Energy		Detail-3 Energy		Detail-3 Energy		Detail-3 Energy	Detail-3 Energy	*3*
4	Detail-2 Energy		Detail-2 Energy		Detail-2 Energy		Detail-2 Energy	Detail-2 Energy	*4*
5	Approx-4 Entropy		Detail-1 Energy		Detail-1 Energy		Detail-1 Energy	Detail-1 Energy	*5*
6	Detail-4 Entropy		Approx-4 Entropy		Approx-4 Entropy		Approx-4 Entropy	Approx-4 Entropy	*6*
7	Detail-3 Entropy		Detail-4 Entropy		Detail-4 Entropy		Detail-4 Entropy	Detail-4 Entropy	*7*
8	Detail-2 Entropy		Detail-3 Entropy		Detail-3 Entropy		Detail-3 Entropy	Detail-3 Entropy	*8*
9	Detail-4 Difference Feature		Detail-2 Entropy		Detail-2 Entropy		Detail-2 Entropy	Detail-2 Entropy	*9*
10	Approx-4 FFT Bin		Detail-1 Entropy		Detail-1 Entropy		Detail-1 Entropy	Detail-1 Entropy	*10*
11	Detail-4 FFT Bin		Approx-4 Difference Feature		Approx-4 Difference Feature		Approx-4 Difference Feature	Approx-4 Difference Feature	*11*
12	Detail-3 FFT Bin		Detail-4 Difference Feature		Detail-4 Difference Feature		Detail-4 Difference Feature	Detail-4 Difference Feature	*12*
13	Detail-2 FFT Bin		Detail-3 Difference Feature		Detail-3 Difference Feature		Detail-3 Difference Feature	Detail-3 Difference Feature	*13*
		14	Detail-2 Difference Feature		Detail-2 Difference Feature		Detail-2 Difference Feature	Detail-2 Difference Feature	*14*
		15	Detail-1 Difference Feature		Detail-1 Difference Feature		Detail-1 Difference Feature	Detail-1 Difference Feature	*15*
		16	Approx-4 FFT Bin		Approx-4 FFT Bin		Approx-4 FFT Bin	~~Approx-4 FFT Bin~~	~~*16*~~
		17	Detail-4 FFT Bin		Detail-4 FFT Bin		Detail-4 FFT Bin	~~Detail-4 FFT Bin~~	~~*17*~~
		18	Detail-3 FFT Bin		Detail-3 FFT Bin		Detail-3 FFT Bin	~~Detail-3 FFT Bin~~	~~*18*~~
		19	Detail-2 FFT Bin		Detail-2 FFT Bin		Detail-2 FFT Bin	~~Detail-2 FFT Bin~~	~~*19*~~
		20	Detail-1 FFT Bin		Detail-1 FFT Bin		Detail-1 FFT Bin	~~Detail-1 FFT Bin~~	~~*20*~~
				21	Approx-4 pt-by-pt Mahal. Dist.		Approx-4 pt-by-pt Mahal. Dist.	Approx-4 pt-by-pt Mahal. Dist.	16
				22	Detail-4 pt-by-pt Mahal. Dist.		Detail-4 pt-by-pt Mahal. Dist.	Detail-4 pt-by-pt Mahal. Dist.	17
				23	Detail-3 pt-by-pt Mahal. Dist.		Detail-3 pt-by-pt Mahal. Dist.	Detail-3 pt-by-pt Mahal. Dist.	18
				24	Detail-2 pt-by-pt Mahal. Dist.		Detail-2 pt-by-pt Mahal. Dist.	Detail-2 pt-by-pt Mahal. Dist.	19
				25	Detail-1 pt-by-pt Mahal. Dist.		Detail-1 pt-by-pt Mahal. Dist.	Detail-1 pt-by-pt Mahal. Dist.	*20*
						26	Approx-4 (pt-by-pt Mahal. Dist.)^2	Approx-4 (pt-by-pt Mahal. Dist.)^2	21
						27	Detail-4 (pt-by-pt Mahal. Dist.)^2	Detail-4 (pt-by-pt Mahal. Dist.)^2	*22*
						28	Detail-3 (pt-by-pt Mahal. Dist.)^2	Detail-3 (pt-by-pt Mahal. Dist.)^2	*23*
						29	Detail-2 (pt-by-pt Mahal. Dist.)^2	Detail-2 (pt-by-pt Mahal. Dist.)^2	*24*
						30	Detail-1 (pt-by-pt Mahal. Dist.)^2	Detail-1 (pt-by-pt Mahal. Dist.)^2	*25*

The variables and notation used in the equations are described the first time they are used in an equation.

Energy – The fraction of the full signal's energy contained in the Approx-4, Detail-4, Detail-3, and Detail-2 wavelet levels.

$$\mathbf{F}_i = \frac{\sum_{k=1}^{n} \mathbf{S}_j^2(k)}{\sum_{p=1}^{N} \mathbf{S}^2(p)} \tag{2.6}$$

where,

$\mathbf{F}_i$	vector holding the 13 features of the ith signature ($\mathbf{F}$ is the feature matrix),
$\mathbf{S}$	vector holding the wavelet decomposition of a signature,
$\mathbf{S}_j$	portion of the wavelet decomposition that make up the jth wavelet level,
j	is the wavelet level, where Detail-1 = 1, Detail-2 = 2, ..., Approx-4 = 5,
k	is an index to the elements of wavelet level j,
n	number of discrete points in the jth wavelet level (e.g., for Detail-1 $n = 256$, Detail-4 $n = 32$),
p	is an index to the elements of the entire decomposed signature,
N	is the total number discrete points in the decomposed signature.

Entropy – The fraction of the total Shannon's entropy of the signal that is contained in the Approx-4, Detail-4, Detail-3, and Detail-2 wavelet levels.

$$\mathbf{F}_i = -\sum_{k=1}^{n} \mathbf{S}_j(k) \ln\left(\mathbf{S}_j(k)\right) \tag{2.7}$$

Difference Measure – the mean Detail-4 of a set of "no-flaw" signatures (the expected Detail-4 signal) which is subtracted from the Detail-4 of the signature under test. This produces a vector containing the difference between each data point. The dot product is taken of the difference vector with itself and this scalar value is the difference measure.

$$\mathbf{F}_i = \left(\mathbf{S}_j - \boldsymbol{\mu}_j\right)^T \left(\mathbf{S}_j - \boldsymbol{\mu}_j\right) \tag{2.8}$$

where,

$\boldsymbol{\mu}_j$	is the mean of the wavelet level j portion of the no-flaw signatures.

FFT Bin Number – A fast Fourier transform (FFT) is performed on Approx-4, Detail-4, Detail-3, and Detail-2 using a step size that equals the number of data points used to represent the level under test, e.g., the FFT step size for Approx-4 and Detail-4 would be 32. Each of the points in the step is a bin; the bin with the maximum value from the FFT is the scalar that becomes the feature. For example, say the seventh discrete point of an FFT results had the largest value for the Detail-4 of some signature X, then signature X's Detail-4 FFT Bin feature value would be seven.

$$\mathbf{Y}(h) = \sum_{g=1}^{N} \mathbf{S}_j(k) \exp\left(\frac{-2\pi i}{N}(k-1)(h-1)\right)$$
$$\mathbf{F}_i = h, \text{ when } max\,\{\,\mathbf{Y}(h)\,\} \tag{2.9}$$

where,

$\mathbf{Y}$ the fast Fourier transform of $\mathbf{S}$,

h index to the elements of $\mathbf{Y}$.

For the calculating features of the original feature set the no-flaw signatures were signatures taken while the pig was stationary in the pipe. An area in the pipe that was free of flaws (SCCs, pitting, corrosion, etc) based on the SCC assay, which was done upon receipt of the pipe by the Battelle PSF, and a visual inspection at the time of our inspection. While we have found these initial assays to be a good indication of were SCCs maybe on the decommissioned pipes, the assay was often done a decade or more before we inspected the pipe. In several cases, SCCs were found that were not on the original assay and in one case the pipe was cut and re-welded causing the point from which the measurements of the axial distances to all the SCCs listed in the assay to be "lost."* Usually these "pauses" were either at the beginning of the scan after the data acquisition was started but prior to the wench being engaged or at the end of the scan once the wench was stopped but before the data acquisition was halted. There were occasionally intentional pauses in the midst of a scan as well in order to collect a stationary set of signatures. A copy of the signatures making up a stationary section would be made and processed using the same procedures as used on the entire scan, as described previously in Section 2.2 and 2.3. The Detail-4s of all the "no-flaw" set (stationary signature set) were averaged to form an expected Detail-4

*The cutting and re-welding were done to the sample pipe while it was on loan from PSF to another facility and the "changes" were not documented beyond stating a section was removed and reattached. When we were inspecting this pipe as part of a blind test we measured the pipe and found it was a foot shorter than the documentation said it was.

signal. The issue with this original technique for forming the "no-flaw" set was that there was no real assurance that the signatures in the stationary ranges were flaw free. It was later found that the assumption that the locations were the no-flaw signatures were collected were truly defect free was erroneous. Additionally, the fact that the "good" set was composed of stationary signatures while the signatures under test were collected while moving seriously skewed the classification results toward almost all signatures producing defect responses. However, these problems are addressed by the features and a more method for calculating the feature that is more representative of the data being classified.

The Final Feature Set

The features belong to the final feature set are listed along with the feature name, a description of the feature, the wavelet levels that it is calculate for, and the equation for the actual calculation. The equations are formulated for calculating the 13 features a single signature at a time. To calculate the features for an entire data set, the calculation should utilize a loop that increments through the signatures one at a time, calculating the 13 features each time. The variables and notation used in the equations are described the first time they are used in an equation.

Energy – The fraction of the full signal's energy contained in the Approx-4, Detail-4, Detail-3, Detail-2, and Detail-1 wavelet levels.

$$\mathbf{F}_i = \frac{\sum_{k=1}^{n} \mathbf{S}_j^2(k)}{\sum_{p=1}^{N} \mathbf{S}^2(p)} \tag{2.10}$$

where,

- $\mathbf{F}_i$ vector holding the 13 features of the ith signature ($\mathbf{F}$ is the feature matrix),
- $\mathbf{S}$ vector holding the wavelet decomposition of a signature,
- $\mathbf{S}_j$ portion of the wavelet decomposition that make up the jth wavelet level,
- j is the wavelet level, where Detail-1 = 1, Detail-2 = 2, ..., Approx-4 = 5,
- k is an index to the elements of wavelet level j,
- n number of discrete points in the jth wavelet level (e.g., for Detail-1 $n = 256$, Detail-4 $n = 32$),
- p is an index to the elements of the entire decomposed signature,
- N is the total number discrete points in the decomposed signature.

Entropy – The entropy (Shannon's entropy) that is contained in the Approx-4, Detail-4, Detail-3, Detail-2, and Detail-1 wavelet levels.

$$\mathbf{F}_i = -\sum_{k=1}^{n} \mathbf{S}_j(k) \ln\left(\mathbf{S}_j(k)\right) \tag{2.11}$$

Difference Measure – An average Approx-4, Detail-4, Detail-3, Detail-2, and Detail-1 is calculated from the no-flaw signatures of the training set. These "expected" signals are subtracted from their matching wavelet level in the signature under test. This produces a vector containing the difference between each data point, one per wavelet level. The dot product is taken of each difference vector with itself and this scalar value is the difference measure for that particular wavelet level.

$$\mathbf{F}_i = \left(\mathbf{S}_j - \boldsymbol{\mu}_j\right)^T \left(\mathbf{S}_j - \boldsymbol{\mu}_j\right) \tag{2.12}$$

where,

$\boldsymbol{\mu}_j$ is the mean of the wavelet level j portion of the no-flaw signatures.

Point-by-Point MD – Each discrete point of a wavelet level is treated as if it were an actual feature unto itself, hence point-by-point. The Mahalanobis distance is calculated using the corresponding wavelet level of the no-flaw signatures as the source of the covariance matrix and the mean vector. The point-by-point Mahalanobis distance results in a scalar that represents how closely the wavelet level under test matches the known no-flaw signatures, while still allowing the inherent variance in each wavelet level of the known no-flaw signatures. This is calculated for the Approx-4, Detail-4, Detail-3, Detail-2, and Detail-1 levels.

$$\mathbf{F}_i = (\mathbf{S}_j - \boldsymbol{\mu}_j)^T \Sigma_j^{-1} (\mathbf{S}_j - \boldsymbol{\mu}_j) \tag{2.13}$$

This equations show the point-by-point Mahalanobis distance expanded so that the point-by-point calculation is shown.

$$\begin{aligned} \mathbf{F}_i = {} & \left[\left(\mathbf{S}_j(1) - \boldsymbol{\mu}_j(1)\right), \left(\mathbf{S}_j(2) - \boldsymbol{\mu}_j(2)\right), \cdots \left(\mathbf{S}_j(n) - \boldsymbol{\mu}_j(n)\right)\right] \cdot \\ & \boldsymbol{\Sigma}_j^{-1} \cdot \begin{bmatrix} \left(\mathbf{S}_j(1) - \boldsymbol{\mu}_j(1)\right) \\ \left(\mathbf{S}_j(2) - \boldsymbol{\mu}_j(2)\right) \\ \vdots \\ \left(\mathbf{S}_j(n) - \boldsymbol{\mu}_j(n)\right) \end{bmatrix} \end{aligned} \tag{2.14}$$

where,

$\mathbf{\Sigma}_j$ is the covariance matrix of the training set's wavelet level j no-flaw signatures.

$(\textbf{Point-by-Point MD})^2$ the value from calculating the point-by-point Mahalanobis distance feature for Approx-4, Detail-4, Detail-3, Detail-2, and Detail-1 is squared.

The FFT-bin features were removed because they provided little to no classification benefits. In fact the only difference between the original feature set with and without the FFT-bin features was a small DC offset. The Mahalanobis distances shown in Figure 2.13, show the Mahalanobis distance resulting from classifying the same data set, using the same classification technique, and the same "good" set. The only difference is that the FFT-bin features were removed from the feature set before classification in first case, Figure 2.13(top), and with them still included in the feature set for the second case, Figure 2.13(middle). Finally, the results from the two cases are overlaid to show the negligible DC offset that is the only contribution of the FFT-bin features, Figure 2.13(bottom).

The point-by-point Mahalanobis distance features were added so that if a defect causes a discernible change only in a particular frequency band or two this useful information will be represented in the feature set. By using the no-flaw signatures from the training set along with the Mahalanobis distance the variations due to sliding through the pipe. Along this same line of thinking, all of the wavelet levels that were not calculated for a feature were added (e.g., Detail-1 energy, Detail-1 entropy, etc.). This way since it is unclear yet how different types of defects (i.e. single SCC, corrosion, pitting, an SCC colony) affect the ultrasonic signal.

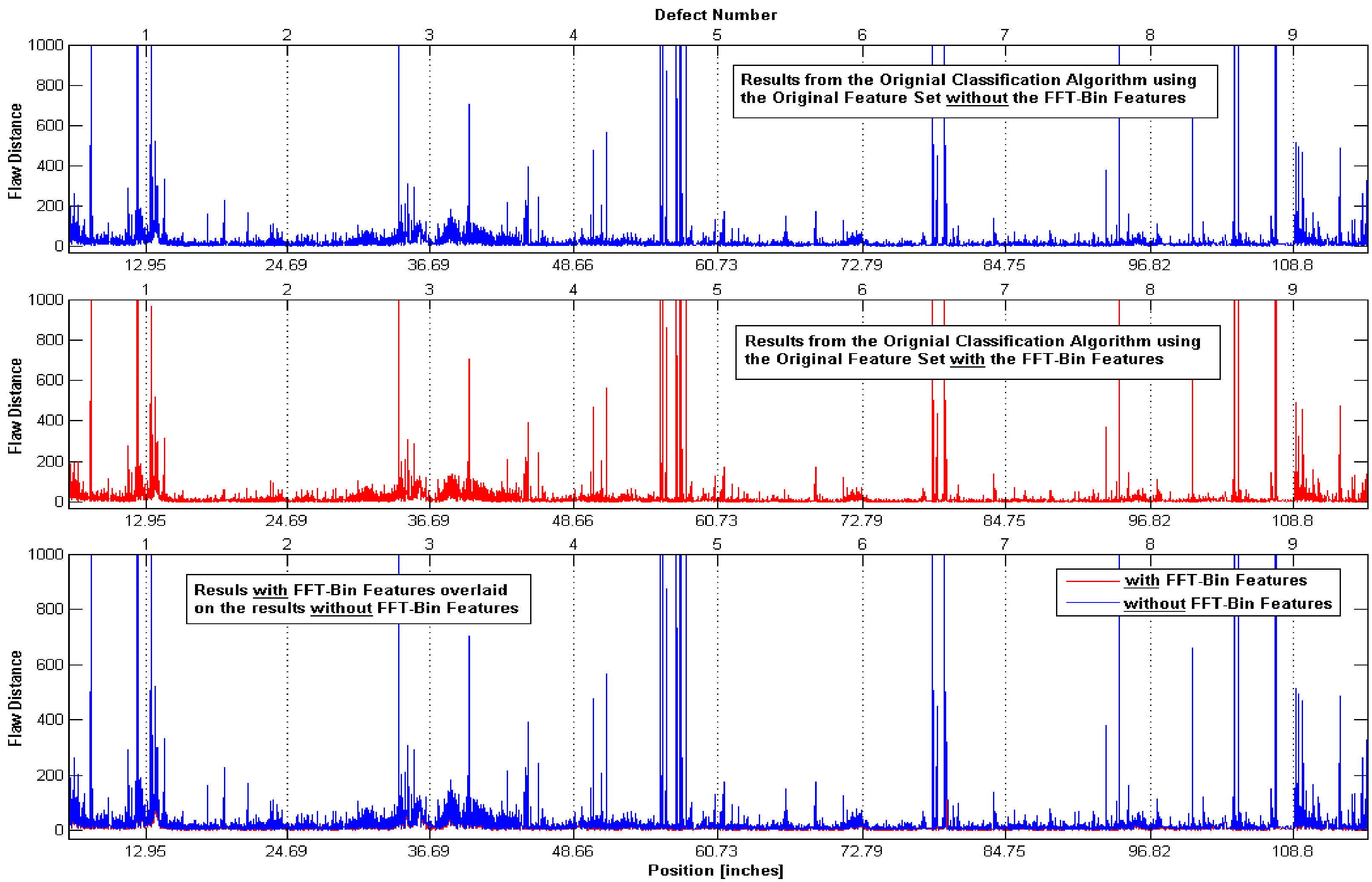

Figure 2.13: The classification results from the tenth scan of scanline I on the machined pipe using the original feature set without the FFT-bin features (top plot) and with the FFT-Bin features (middle plot). When the result from the feature set without the FFT-bin features is overlaid by the results from the feature set with the FFT-bin features the thin red "underlining" of the blue plot shows the only contribution of the FFT-bin features.

Chapter 3

Pattern Recognition and Classification

Now, that signatures have been pre-processed, the blatantly corrupt signatures removed, the 512 point range extracted and decomposed via the DWT, and the features extracted from the decomposition; things are ready for the classification algorithm. To avoid confusion this chapter begins with brief explanations of the individual algorithms used to develop what will be referred to as the final classification algorithm from here on. This is followed by a description of the final classification algorithm as a whole.

3.1 Dimensionality Reduction

The features on there own are unable to clearly identify known SCCs (synthetic or natural) without causing a large number of false defect identifications (i.e. false positives). Dimensionality reduction plays a critical roll in our ability to identify SCCs in pipes. Dimensionality reduction techniques are separated into two groups: supervised techniques such as linear discriminant analysis (LDA), and unsupervised techniques like principal component analysis (PCA).

3.1.1 Principal Component Analysis (PCA)

Principal component analysis (PCA) is a beneficial discriminant analysis technique that, in simplest of terms, seeks to project a set of features into the most efficient space possible while preserving the variance of the data set [27]. This is regardless of the effect upon the discernibility between classes. PCA provides the ability to reduce the redundancy of the data by identifying dimensions containing little variance. The components that contribute little to the total variance of the data set are essentially stochastic noise, so PCA is useful for removing stochastic noise from the data. PCA is capable of projecting a n-dimensional feature space to a d-dimensional feature space, where $d < n$. Overall, PCA seeks a projection that optimize the feature space such that the maximum amount of variance is retained, were the variance is regarded as the information content, while minimizing the mean-square error [27, 31, 32].

To derive a projection using PCA it is important to recognize that a vector of weights is sought that will minimize the mean-square error, while at the same time maximizing the in-feature variance. The mean of each feature needs to be zero so for a $n \times x$ data set, where n is the number of dimensions (features) and x is the number of samples, a mean vector is formed with the mean of each dimension. The mean vector is then subtracted from each n-dimension sample i.e. the mean feature value is subtracted from the "matching" dimension's elements. With the mean removed the covariance matrix is calculated for the data set. The covariance matrix's eigenvalues and eigenvectors are calculated. Each eigenvalue has an associated eigenvector. The eigenvectors are sorted so that their associated eigenvalues are largest to smallest. The largest eigenvalue corresponds to the eigenvector that is the principal component i.e. contains the greatest variance/information. The dimensionality is reduced by keeping only the features necessary to retain 90 to 98 percent of the total variance contained in the complete feature set. The percentage of information is calculated using Eq. (3.1) in which the eigenvalues are summed beginning with the largest value and continuing in descending order until the desired amount of information is retained. Whether the percentage of retained variance is between 90% and 98% or something different entirely is up to the system designer.

$$\text{Percent Information Retained} = \frac{\lambda_1 + \lambda_2 + \cdots + \lambda_n}{\sum_{i=1}^{n} \lambda_i} \tag{3.1}$$

where,

λ_i is the ith largest eigenvalue.

The eigenvalues that are not needed to reach the desired percentage are discarded along with their associated eigenvectors. In a two-dimensional data set the smallest, non-trivial, mean-square error is obtained when the data is projected on to a line that passes through the mean of the entire data set [27, 31]. The direction of this line is in the direction of the eigenvector that minimizes the mean-square error. The eigenvector(s) that will provide these traits are the largest eigenvalues of the data set's covariance matrix. The eigenvalues provide a scalar representation of the variance in a single feature/dimension. Using just the set of eigenvectors corresponding to the eigenvalues retained, a projection matrix is formed. Since the features are the rows and the samples are the columns in the data matrix the projection matrix must be transposed before it is multiplied by the data matrix, as shown in Eq. (3.2).

$$\mathbf{Y} = \mathbf{E}_{set}^{T} \cdot \mathbf{X} \tag{3.2}$$

where,

$\mathbf{Y}$	the projected data set matrix
$\mathbf{E}_{set}$	the matrix formed by the set of eigenvectors retained
$\mathbf{X}$	the original mean-removed data set matrix

As a simplistic example a data sets containing two classes represented by two features is shown in Figure 3.1(a), after the full data set was normalized so that each feature has a mean of zero and unit standard deviation. This is done so that mere scaling does not allow a feature to become dominant during the analysis. While the two classes are obviously easily separated by a line with only a marginal number of points being miss-classified it is the effect of reducing the dimensionality from two dimensions to one using PCA that is important here. In Figure 3.1(b), the first and second principal components (PCs) are plotted indicating the line the data would be projected to when either the first or second PC is used. Figure 3.1(c) show a histogram of the number of samples located in the same spots when all the samples were projected to one dimension using the primary PC. Figure 3.1(d) is the histogram when all the samples are projected onto the secondary PC.

3.1.2 Linear Discriminant Analysis (LDA)

Linear Discriminant Analysis (LDA), also known as the Fischer Linear Discriminant technique is another method for projecting data to a lower dimensionality. When LDA is used to project data with more than two classes it is also occasionally referred to as Multiple Discriminant Analysis (MDA) [27]. PCA and LDA both seek

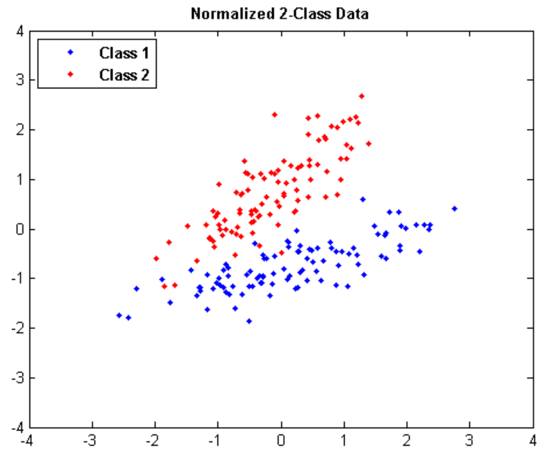

(a) The normalized two class data.

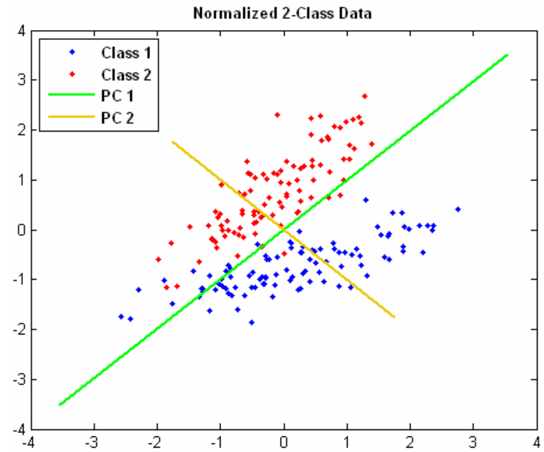

(b) The first two PCs (eigenvectors) from PCA, overlaid on the normalized data set.

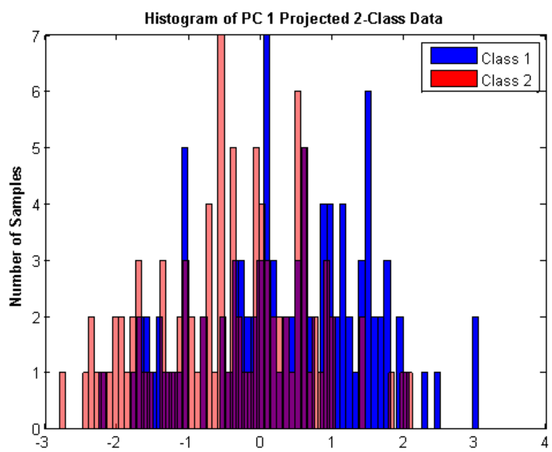

(c) The data is projected to one dimension using the largest eigenvalue's eigenvector (PC) from PCA. Then creating a histogram of the projected data the separability of the two classes is clearly shown.

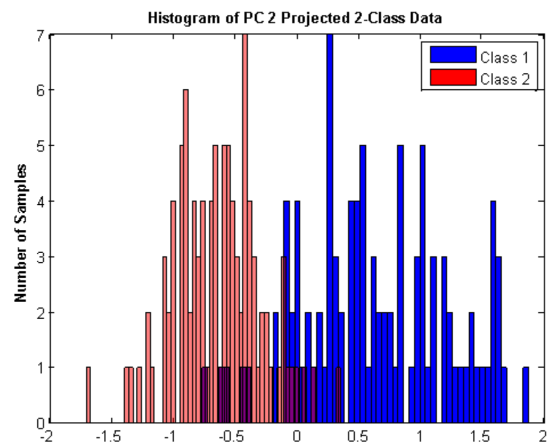

(d) The data is projected to one dimension using the second largest eigenvalue's eigenvector from PCA. Then creating a histogram of the projected data the separability of the two classes is clearly shown.

Figure 3.1: Using the simple two class, two feature data shown in (a) the first two PCs, which are eigenvectors from performing PCA, are shown overlaid on top of data in (b). Creating a histogram from the data after it is projected to one dimension allows the retained variance to easily be seen as well as the separability between the two classes. (c) is from using the primary PC and (d) is from using the second PC.

to project data to a lower dimensionality but differ significantly in their affect on the data. The difference is that LDA seeks a projection that allows for the best discrimination between classes, while PCA seeks a projection that represents the data in the fewest dimensions i.e. the most dimensionally efficient representation [27]. Another, significant, difference is that LDA is a projection from a d-dimensional space to at most a $(c-1)$ dimensional space, where c is the number of classes represented in the data set. For example, the feature set at the point when LDA is applied, in this research, has 13 dimensions (features) and represents three unique classes. Therefore the input to LDA, a $13 \times n$-signature feature matrix, is reduced to a 2* $\times$ n-signature feature space. Where as PCA could be used to project this data to any dimensionality, from 1 to 13.

To apply LDA a projection matrix is calculated in the form of a classic eigenproblem, Eq. (3.3). This calculation is formulated using the between-class scatter matrix, $\mathbf{S}_{\text{B}}$, calculated using Eq. (3.4), the with-in class scatter matrix, $\mathbf{S}_{\text{W}}$, Eq. (3.5), the scatter matrix of the ith class, (3.6), the mean vector of the entire data set, $\mathbf{m}$, Eq. (3.8), and the mean feature vector using just the ith class's signatures Eq. (3.7). The eigenvectors resulting from this calculation are sorted into descending value via the descending order of the eigenvalues. Then the $(c-1)$ eigenvectors, which are column vectors, are used to from the projection matrix by "stacking" the eigenvectors side-by-side, such that the eigenvectors remain columns.

$$\mathbf{S}_{\text{B}}\mathbf{w}_i = \lambda_i \mathbf{S}_{\text{W}}\mathbf{w}_i \tag{3.3}$$

$$\mathbf{S}_{\text{B}} = \sum_{i=1}^{c} n_i(\mathbf{m}_i - \mathbf{m})(\mathbf{m}_i - \mathbf{m})^T \tag{3.4}$$

$$\mathbf{S}_{\text{W}} = \sum_{i=1}^{c} \mathbf{S}_i \tag{3.5}$$

$$\mathbf{S}_i = \sum_{\mathbf{x} \in D_i} (\mathbf{x} - \mathbf{m}_i)(\mathbf{x} - \mathbf{m}_i)^T \tag{3.6}$$

$$\mathbf{m}_i = \frac{1}{n_i} \sum_{x \in D_i} \mathbf{x} \tag{3.7}$$

$$\mathbf{m} = \frac{1}{n} \sum_{i=1}^{c} n_i \mathbf{m}_i \tag{3.8}$$

* In this situation you could also use LDA to reduce to single dimension from 13 dimensions. Your are limited to results containing a maximum of $(c-1)$ dimensions when using LDA.

where,

c	is the number of classes,
$\mathbf{x}$	is the feature vector of single signature,
$\mathbf{m_i}$	is the mean feature vector using only the ith class' samples,
$\mathbf{m}$	is a vector containing the mean of each feature using the entire data set,
n	is the number of samples in the entire data set,
n_i	is the total number of samples belonging to the ith class,
λ_i	is the ith largest eigenvalue,
$\mathbf{w}_i$	is the ith eigenvector (associated with the ith largest eigenvalue).

Performing LDA on the same two-class, two-feature data set used in the simplistic PCA example and overlaying the LDA projection vector with the data results in Figure 3.2(a). By overlaying the vectors that are the three possible projections from two dimensions down to one with the data set it is clear that the clearest separation between Class 1 (blue) and Class 2 (red) will result from using the LDA projection vector, Figure 3.2(b). A histogram of the 1-D LDA projected data set is shown in Figure 3.2(c). LDA separated the data so well you can actual see that only three samples from the red class (Class 2) would be miss-classified as the blue class (Class 1).

The LDA 1-D projection can be easily compared to the PCA 1-D projection (the primary PC from PCA) using the histograms in Figure 3.3. Below each histogram, in Figure 3.3, is a scatter plot of the actual 1-D projected samples from which the histogram above each scatter plot was generated. A different marker is used to differentiate the two classes and also shows the ability to separate the two classes using only one dimension (feature). It is important to remember that while in this **simplistic** example LDA clearly separates the two classes using only one dimension better than PCA; this is a very idealistic example. PCA and LDA each provide benefits that the other does not. For example, PCA is good for removing stochastic noise and requires no training set i.e. it is an unsupervised dimensionality reduction technique. LDA will improve the classification results by maximizing the between-class variance while minimizing the in-class variance, but requires a training set i.e. it is a supervised technique.

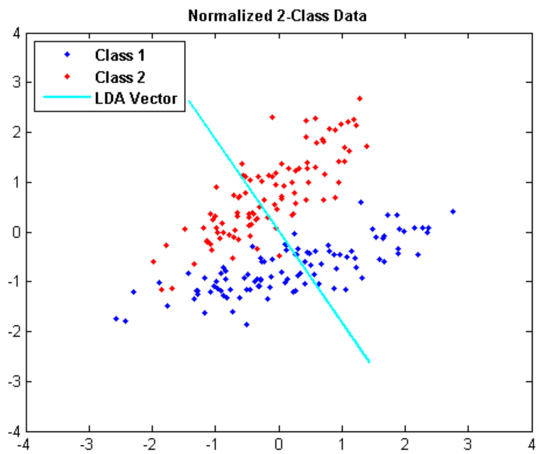

(a) The normalized, simplistic two class data with the one-dimensional LDA projection vector overlaid.

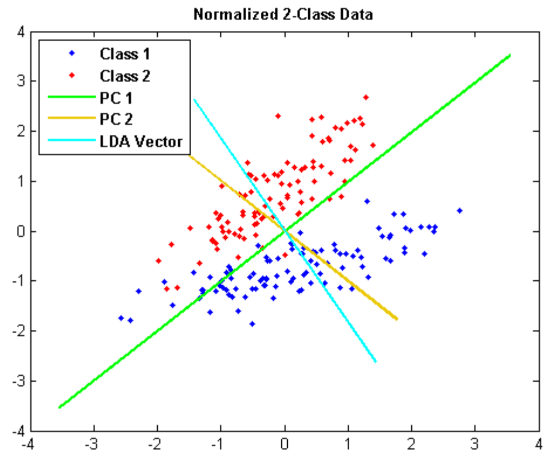

(b) The two class data with the one-dimensional LDA projection vector overlaid along with the first two one-dimensional PCs from PCA.

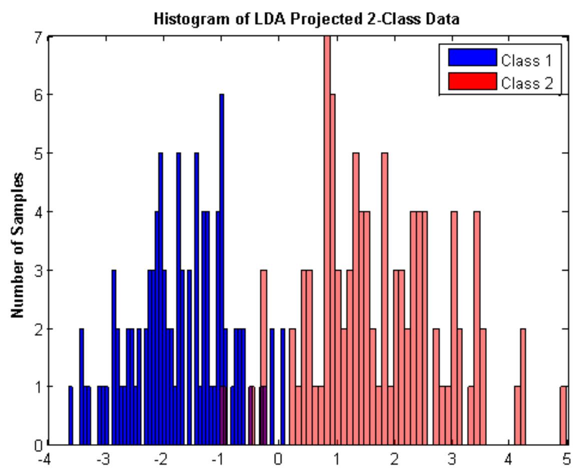

(c) The data is projected to one dimension using the LDA projection matrix, then a histogram of the projected data was created to show the separability of the two classes.

Figure 3.2: Using the same simple two class, two feature data shown in Figure 3.1(a) the vector along which the data will be projected to is shown overlaid on the data in (a). In (b) the one-dimensional projection vector for LDA, the primary PC from PCA, and the second PC from PCA are all shown overlaid together. Creating a histogram from the data after it is projected to one dimension via LDA allows the separability between the two classes to be seen in (c).

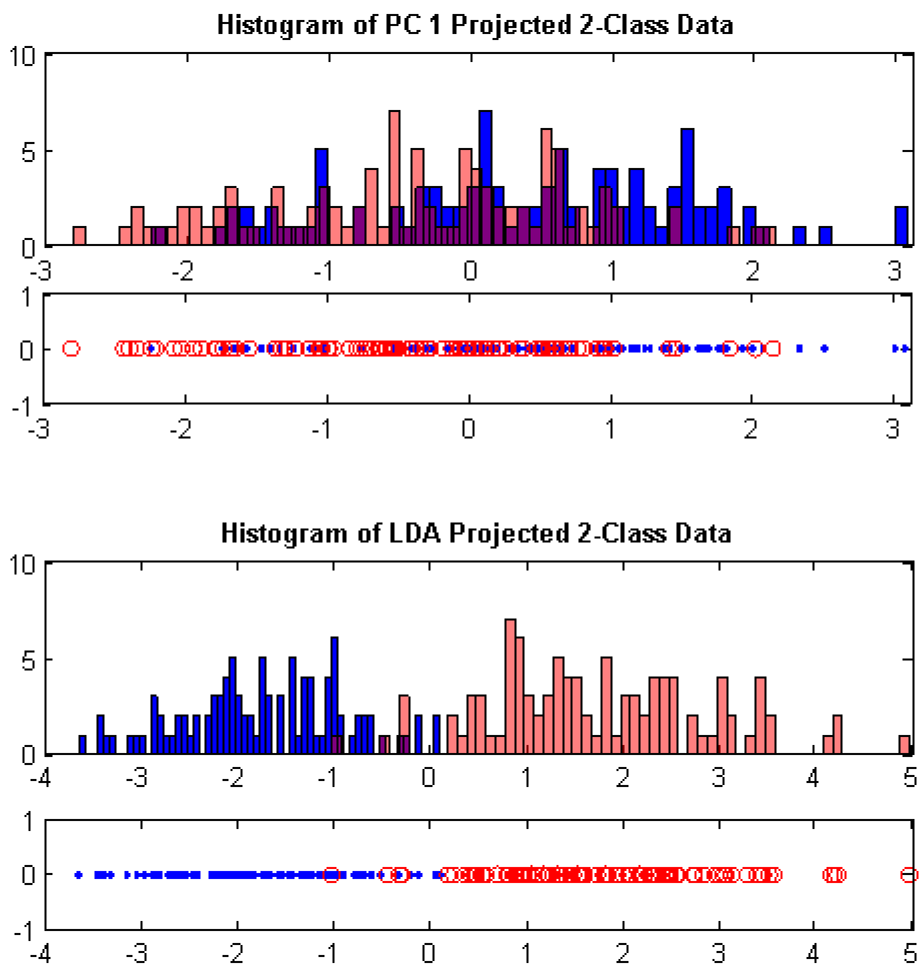

Figure 3.3: The histograms show the number of data points "in the same location" and the scatter plot underneath the histogram shows the actual 1-D projected samples the histogram was generated from. The blue bars and dots are Class 1. The red bars and circles are Class 2.

3.1.3 PCA+LDA

PCA+LDA is a innovative technique used for dimensionality reduction. It has primarily been used in facial recognition [33, 34, 35]. PCA+LDA combines the noise reducing benefits of PCA with the class separability improvements of LDA. PCA+LDA was adopted in facial recognition to overcome the weaknesses of using just LDA, which are that samples not represented in the training set, with different backgrounds, or a notably different version of training sample have little chance of identification [34, 35]. PCA on the other hand has its disadvantage rooted in the fact that the within class-variance is not minimized and so makes the final classification difficult [34]. These problems are similar, and in some cases identical, to the problems we face in the EMAT data. The EMAT data has been challenging to represent in a training set, which has lead to a rather small training set. The in-class variances are large especially compared to the between class variance. However, by combining PCA and LDA these problems are significantly reduced while still obtaining the benefits of reduced dimensionality and stochastic noise removal from PCA and the simultaneous minimization of the in-class variance and maximization of the between-class variance from LDA. Additionally, it has been shown in [36] that there is no information lost when performing PCA+LDA when all the PCA eigenvectors are retained. For this research, the only information lost due to performing PCA+LDA, was what was already being discarded when only PCA was used. When calculating PCA+LDA the first step is to perform PCA on the full feature set. Then the full feature set is projected via the PCA projection matrix. The LDA is then performed on the PCA projected data. Figure 3.4(a) shows the same simplistic two-class example projected into PCA-space with the one-dimensional LDA projection vector overlaid. Overlaying the histogram of each class after being projected to one dimension using PCA+LDA, as in Figure 3.4(b), shows the separability of the two classes and the number of intermixed samples. Several eigenvectors are discarded during the PCA step of the algorithm as they are likely stochastic noise elements based on the fact that all the discarded eigenvectors had eigenvalues representing less than 0.1% each of the total variance. While Yang and Yang show that no information is lost when all PCA eigenvectors are retained, Fidler and Leonardis show in [35] that classification results can be improved by eliminating eigenvectors with a small associated eigenvalues. Overall, the performance of PCA, LDA, and PCA+LDA when used to projection the simplistic, 2-class example data to one-dimensional can be seen side-by-side in Figure 3.5.

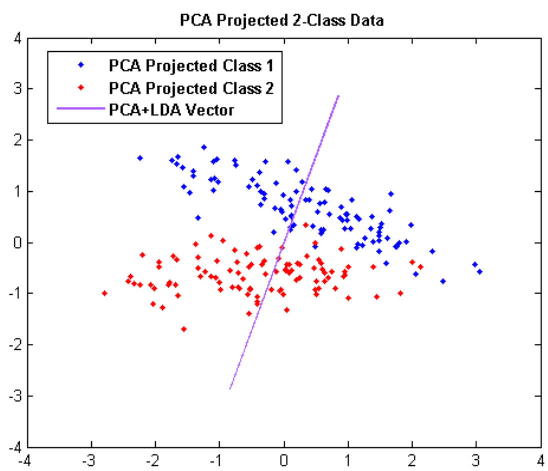

(a) The two class data after being projected using both PCA eigenvectors with the one-dimensional LDA projection vector overlaid, i.e. the PCA+LDA projection vector.

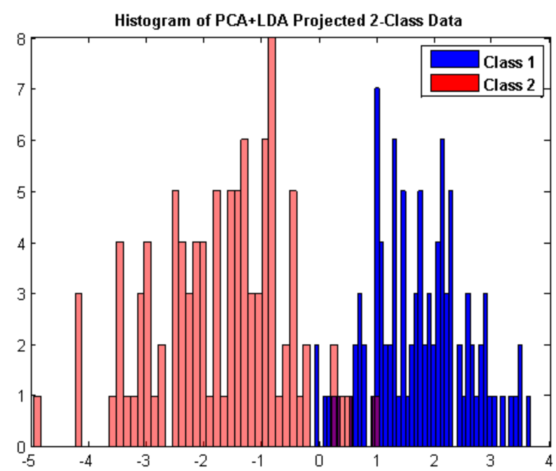

(b) The data was projected to one dimension using the PCA+LDA projection matrix. Then a histogram of the projected data was created to show the separability of the two classes.

Figure 3.4: The same simple two class, two feature data shown in Figure 3.1(a) was projected using the two eigenvectors calculated in the PCA example. The vector along which the data will be projected to by applying LDA to the PCA projected samples is shown overlaid (a), i.e. the one-dimensional projection when LDA is applied in the PCA subspace. The separability between the two classes is illustrated, in (b), by the combined histograms of the classes after being projected to one dimension using PCA+LDA.

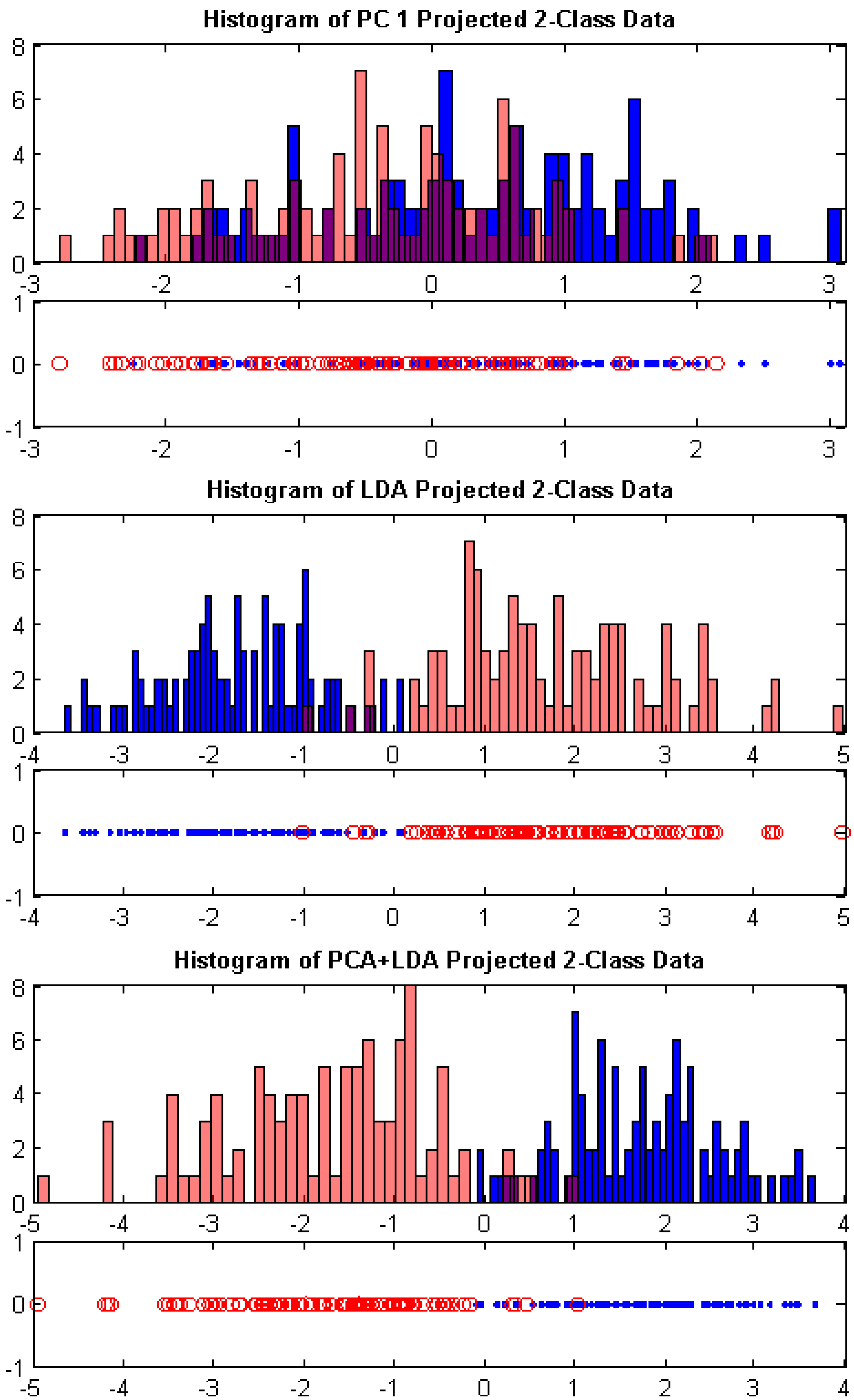

Figure 3.5: The histograms show the number of data points "in the same location" and the scatter plot underneath the histogram shows the actual 1-D projected samples the histogram was generated from. The blue bars and dots are Class 1. The red bars and circles are Class 2.

3.2 Classifier – Mahalanobis Distance

There is still quite a bit of variability in just the features from known no-flaw signatures even after performing PCA+LDA upon them. Combined with the fact that there is such a small number of known SCC signatures in existence limits the number of applicable classification algorithms. Because of the inability to quantify the severity of real SCCs (defects identified using MPI could be mere scratches or completely through the pipe wall) the ability of signatures taken over real SCCs have no guarantee of being even slightly representative of the "standard" SCC signature. However, no-flaw signatures can be selected with acceptable confidence. These factors lead to the selection of Mahalanobis distance for a classifier. The Mahalanobis distance accommodates both the fact that statistically only the no-flaw signatures are well represented and that there is an non-negligible amount of variation even in just the no-flaw class's signatures. The calculation of the Mahalanobis distance, Eqn. (3.9), returns a scalar value indicating a signatures distance from the "target" clusters centroid. We refer to the Mahalanobis distance value as the "flaw distance," since the larger the distance the more "flaw-like" the signature under test is.

$$\text{Mahalanobis Distance} = (\mathbf{x} - \boldsymbol{\mu})^T \Sigma^{-1} (\mathbf{x} - \boldsymbol{\mu}) \tag{3.9}$$

Mahalanobis distance differs from Euclidean distance in that Mahalanobis distance calculates a distance from the centroid of a multi-dimensional cloud of data while Euclidean distance is calculated from a single data point to another single point. The Mahalanobis distance calculates the distance from a single data point to the "target" set. The covariance matrix of "target" set is used in the calculation of the Mahalanobis distance and is how the shape of the hyper-ellipsoid "cloud" formed by the "target" set [27, 32].

The covariance matrix used in the calculation allows the shape of the cluster to be a factor in the distance [27]. This is regardless of the unknown multi-dimensional shape a cluster forms. For example, if a sample is close to a protruding lobe but not necessarily the centroid of the cluster it will not receive an "unfairly" long Mahalanobis distance.

3.3 Complete Classification Algorithm

The features are all normalized after their calculation and before any other operations are performed with them. To normalize the features the mean and standard deviation of each feature is calculated. The standard deviation calculation uses the form of the equation shown in Eq. (3.10). The mean of each feature is subtracted from their respective feature vector, the results of which are then divided by the standard deviation of that feature. This results in each feature vector having a mean of zero and unit standard deviation, as shown for a single feature value in Eq. (3.11),

$$\sigma = \left(\frac{1}{n} \sum_{i=1}^{n} (x_i - m)^2 \right)^{\frac{1}{2}} \tag{3.10}$$

where,

n is the number of elements in the feature vector,

m is the mean of the feature vector,

x_i is the ith element of the feature vector.

$$Standardized\,Value = \frac{(Value - Mean)}{Standard\;Deviation} \tag{3.11}$$

With the features normalized the PCA+LDA step begins using the projection matrices derived from the training set. The PCA projection matrix and the decision on how many dimensions to retain were derived as follows. PCA was performed on the training set, whose features were calculated and normalized same as for the data sets. The eigenvalues were normalized so that they sum to one (100%). This does not change the ordering or the variance represented by the eigenvalues. Then by doing a cumulative summation of the normalized eigenvalues, the fraction of total information (variance) retained by keeping the n largest eigenvalues can be seen. For the 25-feature training set the un-normalized eigenvalues are shown in column one of Table 3.3, the normalized eigenvalues in column 2, and the cumulative sum (running summation of the "percentage" of information retained) is shown in column 3. In the end, the 13 largest eigenvalues, which retained 97% of the information, were kept. Since the choice of how many eigenvalues to retain is a situation-by-situation decision, the final cut was based on the intuitive decision that since the fourteenth eigenvalue is the first eigenvalue to contain less than 1% of the total variance of the data set its eigenvector and all the rest were cut. Using the eigenvectors corresponding to the thirteen largest eigenvalues the 25-features of each signature are projected into 13 features in the PCA subspace.

The LDA step of PCA+LDA brings up an important detail that contributed to the improvements resulting from the final classification algorithm. Since LDA projects to a maximum of ($number\ of\ classes - 1$) dimensions if the only classes were flaw and no-flaw then the results would be a one-dimensional vector. However, by creating a third class in the training set of signatures corresponding to anomalies in the Mahalanobis distance at locations on the training pipe known to be free of any type of defect LDA results in a two-dimensional projection and Mahalanobis distance can still be used as the classifier. This resulted in a significant change to the responses from anomalies in the Mahalanobis distance.

These changes made the anomaly responses distinguishable from defect responses and so the characteristics that a response must have in order to be a defect were developed. So projecting the PCA features using the three class LDA projection matrix derived from the PCA projected training set data produces the final features used in the classification of each signature. Using the Mahalanobis distance calculated with the PCA+LDA projected no-flaw portion of the training set as the "target," a Mahalanobis distance value for each signature in the data set under-test is found. This Mahalanobis distance is then examined and responses (spikes in the flaw distance) that meet the criteria to be a defect are visually identified along with their axial position in the scanned pipe.

One common question that arises about the Mahalanobis distance is, "if the Mahalanobis distance is calculated with the flaw signatures from the training set as the "target" set and likewise for the anomaly signatures in the training set." The answer is we do not. The reason is that the flaw signatures in the training set are from synthetic SCCs and so could result in real SCCs being mis-classified. The reason the anomaly signatures are not used either is that there is no benefit in this identification. Anomalies' are present in every single pipe that has ever been scanned in the course of the project's life. Pipes that were in service for decades and pipes that have never been used or even buried all show anomaly responses. As no anomaly response has ever corresponded to a defect (real or synthetic) it is our opinion that they are intrinsic, metallurgic differences in the pipe's composition that affect the ferromagnetic properties at the specific locations the anomaly response appears. Additionally, the concern is to identify a signature as being a flaw or no-flaw not as an anomalies.

Table 3.1: The first column shows the eigenvalues calculated from the 25-feature training set, the second column is the eigenvalues normalized so that they sum to one, and the third column is the percentage (when multiplied by 100) of the information (variance) retained by keeping the n largest eigenvalues (i.e. keeping the eigenvalues in the row containing the value plus all the eigenvalues above that row.) NOTE: the values in the table should be multiplied by 100 to truly be in percent format.

Number	Normalized Eigenvalues	Cumulative Sum
1	0.26082	0.26082
2	0.13005	0.39087
3	0.11331	0.50417
4	0.10101	0.60519
5	0.08702	0.69221
6	0.06566	0.75787
7	0.05164	0.80950
8	0.03999	0.84949
9	0.03792	0.88740
10	0.03031	0.91771
11	0.02541	0.94312
12	0.01715	0.96027
13	0.01113	0.97140
14	0.00759	0.97899
15	0.00546	0.98446
16	0.00365	0.98811
17	0.00300	0.99110
18	0.00249	0.99359
19	0.00173	0.99532
20	0.00122	0.99654
21	0.00105	0.99759
22	0.00093	0.99852
23	0.00081	0.99933
24	0.00067	1.00
25	0.00	1.00
Sum	**1.00**	

So in summary, the no-flaw signatures in the training set do represent the no-flaw signatures found in both the machined pipe and the decommissioned pipes that have been inspected. Because of this the training set no-flaw signatures can be used with confidence as the "target" for calculating Mahalanobis distance.

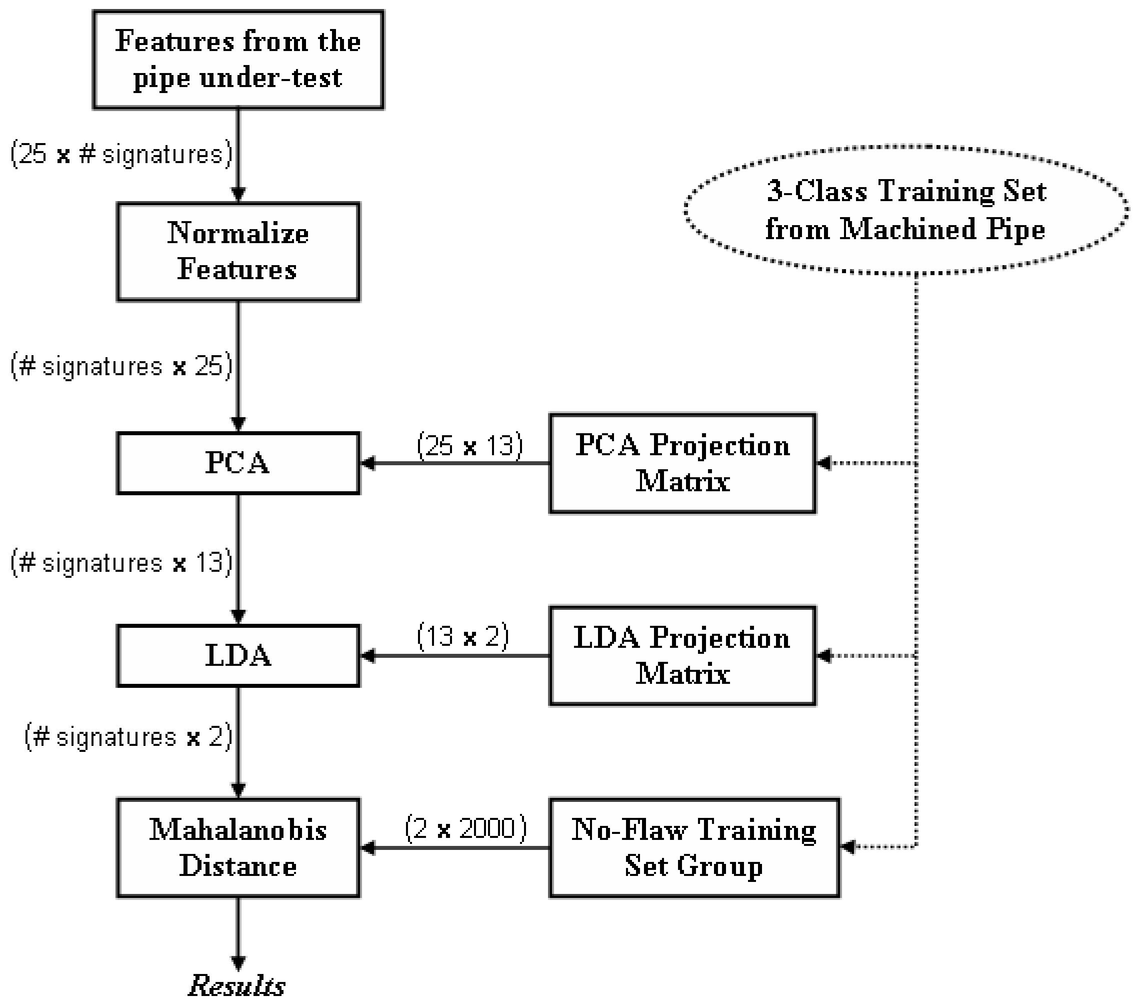

Figure 3.6: Flowchart of the Complete Classification Algorithm

Chapter 4

Experiments and Results

Once features have been extracted from the wavelet decomposition of the EMAT signals they are ready for use in identifying the presence or lack of SCCs in the scanned section of pipe. This classification is performed as described in Section 3.3. All of the following results and statistics make use of the data collected from multiple scans of the machined pipe in order to have an objective, quantified ground truth to compare the original and final classification algorithms' results when both the original and final feature sets are used. Only scanline I and II made up of parabolic cuts are used, since the parabolic cuts are the most realistic synthetic SCCs. The scanlines and synthetic SCCs (parabolic cuts) and their creation will now be explained.

4.1 The Training Set

In the beginning of working on the ability to detect SCCs while moving, a training set was simply the selection of a range (or ranges) of signatures after the signature quality check (Section 2.2.3) that appeared to be "normal" when displayed as a B-scan.* Signatures that were abnormal when compared to the 100 signatures or so before and after it were removed. At the end of this process a set of signatures which still contained the variation seen between known good signatures but contained no signatures that would be an outlier from the rest of the set. This process took days to perform and in the end the set was really just for use as the "no-flaw" set

*At the time when training sets (i.e. good sets) were constructed by hand in this manner the signature quality check did not yet include the 180° out-of-phase check or the use the improved thresholds.

("good" set) when calculating the expected signal needed for calculating the difference features (Section 2.3.2) and to calculate the centroid and covariance matrix used in the Mahalanobis distance. The most disappointing things of all were that *a*) the set generally only produced results semi-close to what was anticipated for the scanline the set was derived from; *b*) no set created this way ever worked on a different pipe, even if the pipes were the same diameter and had the same wall thickness; and *c*) the range(s) of signatures selected based on their appearance in the B-scan could contain signatures taken over a defect.

In one particularly unfortunate incident involving a blind test on a pipe containing natural SCCs, the ranges of "no-flaw" signatures were selected based on there appearance from the B-scan and carefully examined and cleaned by hand turned out to be almost entirely flaw signatures. So in this incident it turned out that the smaller the Mahalanobis distance was the likelier is was actual defect, but of course this was not know until the results were released. While this was the worst-case scenario it is representative of the risk of creating a no-flaw set in this manner. Even when the ranges selected from known good areas were used to generate a no-flaw set it was not useful for evaluating the ability of the classification algorithm to identify SCCs, since the flaw indications could actually be a metallurgic anomaly or such. In the end, the creation of a fully quantized training set was one of the most important and difficult outcomes of this work.

This truly supervised training set data has allowed a classification algorithm to be developed that is "transportable" between different pipes of the same diameter and wall thickness as the pipe used to create the training set, between 30-inch diameter with a different wall thickness, and even 26-inch diameter pipes. The difficulty in developing a classification algorithm to detect SCCs is primarily due to the rarity of pipes containing SCCs available for testing. Because of this we do not have enough real SCC signatures to adequately characterize a signature as an SCC signature.In order to detect SCCs we needed a known set of defects in a known environment. By "known set of defects" what is meant is that the SCCs depths, lengths, and widths are known. The problem with needing SCCs with known dimensions is that to determine the depth along the entire length of an SCCs requires the defect area be removed from the pipe and either thinly sliced or x-rayed. It is possible to determine a maximum depth, without destroying the pipe, using a specialized ultrasonic inspection technique, applicable only from the exterior of the pipe specimen.

This specialized inspection is costly and must be done by a highly skilled technician with access to calibration blocks. A technician was hired to do this inspection in hopes of determining depth and thus the severity of the SCCs contained in a pipe that was inspected during a blind test and demonstration at the Battelle PSF. The data from this did provided insight in to the severity and thus the sensitivity of our EMAT sensor system to depth. However, it was not possible to determine the "amount" of an SCC that was at or close to its measured maximum depth. In addition, when this technique is used on a SCC colony, it only provides the maximum depth of the entire colony, but again how much of the colony is at or near that depth is unknown. Based on these results, it was possible to determine if an SCC that was not detected during the blind trial was due to it being too shallow.[†] However, a confident determination as to what the limitations of the sensor system are based solely on these specialized measurements cannot be made, since there are still too many unknowns with regards to the actual SCCs.

As for a known environment, this is referring to the pipe containing the defects. What the pipe has been subjected to during its "life." So to develop reliable statistics as to the sensor systems capabilities and to improve the quality of our features (e.g., add new features, remove redundant or noisy features, etc) a pipe was purchased and precision synthetic SCCs machined in to it.

A 10-foot long section of brand new 30-inch diameter, 0.375-inch thick pipe was purchased. By using a new, never-been-used section of pipe we eliminated the possibility of there being any defects (corrosion, pitting, SCCs), that the pipe is out-of-round, and that any unknown, undocumented alteration, testing, or abuse occurred to the pipe. To create synthetic SCCs that closely mimicked the characteristics of natural SCCs a set of size and spacing specifications for machining synthetic SCC defects in to the pipe [37] were determined that would mimic real SCCs. In the end a machining facility with an electrical discharge machining (EDM) system capable of accommodating the pipe segment was contracted to perform the machining. EDM machining can be used on hardened steel and is capable of making precise angles, cuts, curves, even cavities, all with tolerances at or near 0.0001-inches [38]. This pipe is referred to as the machined pipe through out the remainder of this thesis.

[†]If an SCC had a maximum depth that was shallow compared to the wall thickness it is safe to assume that is why it was not detected.

Four lines of synthetic defects were created, each line contains nine defects separated by 12-inches from center-to-center, and each scanline separated by 60° circumferentially, Figure 4.1. These defects, from left to right, are numbered one through nine. This one through nine from left to right numbering will be constant through out the remainder of this thesis, unless otherwise stated. The defect classification results from the machined pipe are also displayed with defect-1 on the left edge and defect-9 on the right edge. Defect-1 on each scanline consist of either two or three staggered cuts to simulate an SCC colony and serves a second purpose of being a physical indication of which end of the pipe defect-1 is actually on. The layout of the two staggered cuts and three staggered cuts are shown in Figure 4.2(a) and Figure 4.2(b) respectively. All the cuts for defect-1 are made to exactly the same width, depth, and when applicable length specifications.

The width and length of typical SCCs have been measured and thus can be "translated" in to dimensions for the creation of synthetic SCCs in the new pipe. What the depth profile should be was a far more difficult decision. In the end two of the four scanlines were made using the EDM process, scanline III and IV. All the defects in scanline III and IV have uniform depth for the entire defect's length. This also means that there are straight, 90° vertical transition "in to" and "out of" the cuts. Figure 4.3(a) shows the generic profile of the EDM cuts. The depth, width, and length of each rectangular cut was specified in [37]. The other two scanlines, scanline I and II, were made using a circular cutting wheel with a one inch diameter to the specifications also in [37]. These defects are what we have come to refer to as the parabolic cuts (defects).

The parabolic defects are spaced 12-inch a part center-to-center. Since the parabolic cuts were made using a cutting wheel, the depth and width were specified, but not the length. The specified depth is the maximum depth into the pipe and is essentially a point depth. So the parabolic cuts only have the length that was necessary for the wheel to penetrate the pipe wall to the specified depth. Figure 4.3(b) shows a generic depth profile for a parabolic cut. The specific dimensions for the defects on scanline I and II, including the length of each defect as measured after the specified depth was reached, are shown in Table 4.1. Since the specified depth of each parabolic cut is a point depth, the average depth is also included as part of the data in Table 4.2. The fact that the parabolic cuts do not have a uniform depth and transition gradually "in to" and "out of" the pipe is far more SCC-like than the rectangular cuts.

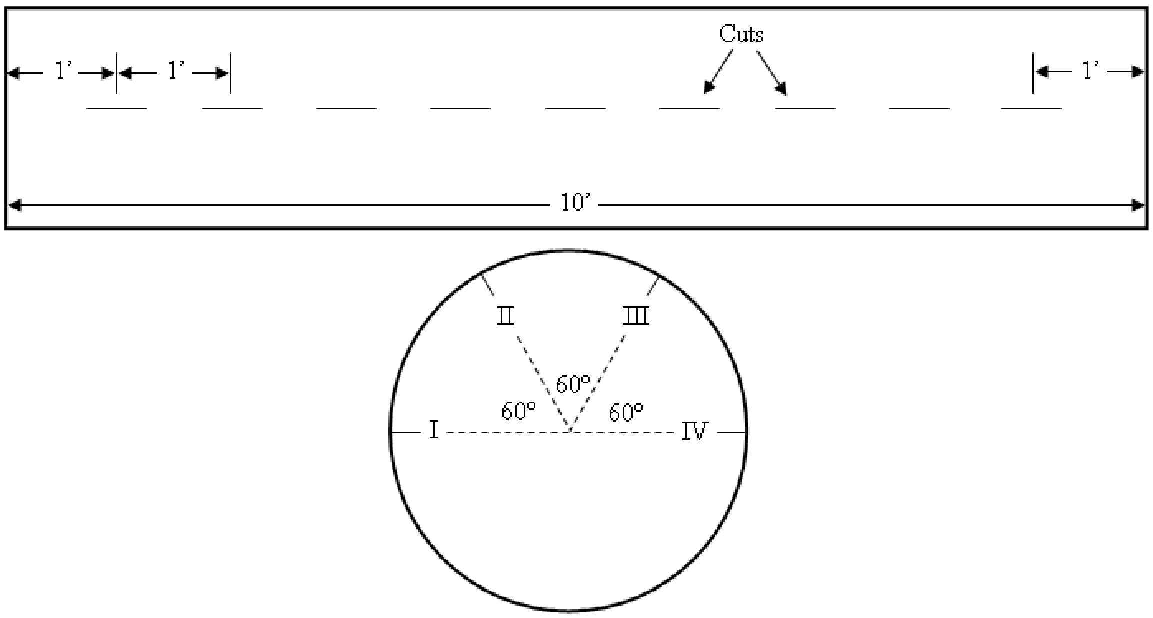

Figure 4.1: Each scanline consist of nine defects spaced 12-inches apart center-to-center. These defects are named one through nine from left to right in this figure. Defect one of each scanline is identifiable on the pipe because it is either a double cut, Figure 4.2(a), or a triple cut defect, Figure 4.2(b).

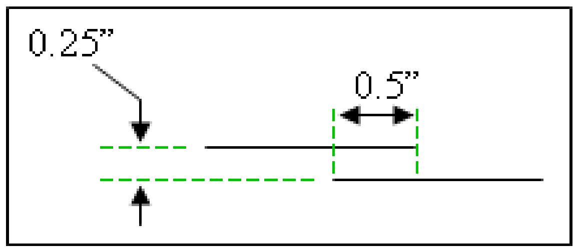

(a) The specified traits of the double cut defects are that they overlap by a half inch (0.5") axially and are separated circumferentially by a quarter of an inch (0.25"). One cut is on the reference line.

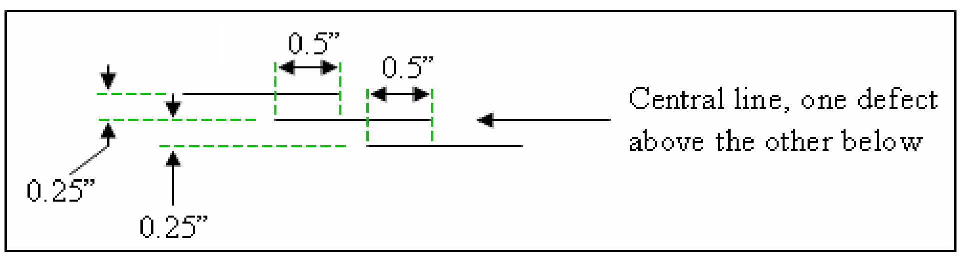

(b) Three staggered cuts at approximately the same location with a half inch (0.5") overlap and circumferential separation of a quarter inch (0.25") between each cut. The middle cut is on the reference line.

Figure 4.2: The reference line is the scanline I, II, III or IV [37].

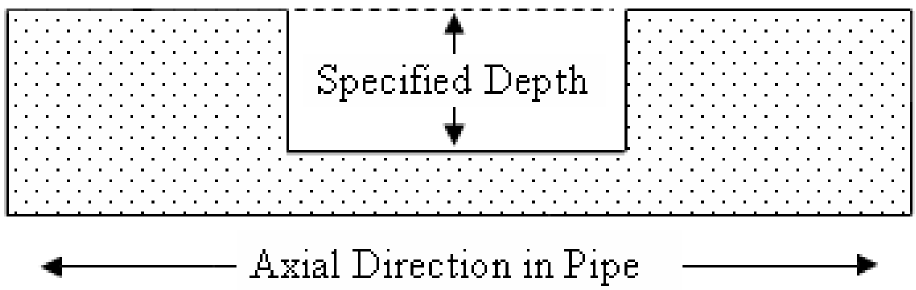

(a) Generic depth profile of a rectangular cut made using the EDM process.

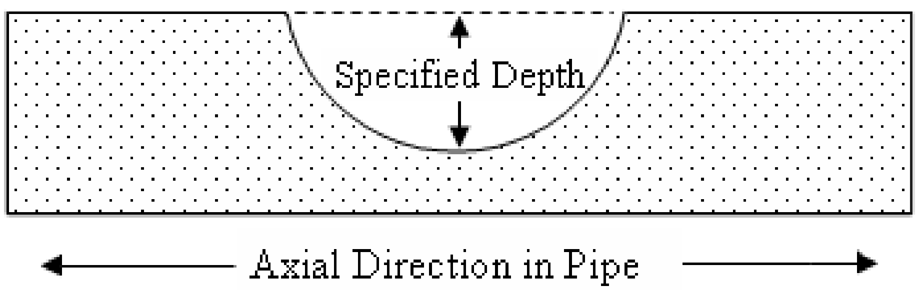

(b) Generic depth profile of a parabolic cut.

Figure 4.3: Generic depth profiles for the rectangular cuts, scanlines III and IV, and the parabolic cuts, scanlines I and II.

Because the length, width, and exact maximum depth of each SCC-like parabolic cut were known, the exact signatures taken over each of the parabolic cuts on scanline I and II, with one exception, were used to construct a "flaw" set. The exception is that after segmenting out the signatures taken across each defect in scanline I and II, the signatures from the 0.035-inch deep defects (the 10% max depth defects, 6.3% average depth). This is in order to eliminate the possibility that these very shallow, single "crack" defects would have the effect of including no-flaw signatures in with flaw signatures, effectively biasing flaw signature group in the training set. The same defects on an operational pipeline would not merit repair, let alone attention. Since the pipe was known to be brand new and every defect was placed according to the design specifications, the signatures from the anomaly locations where extracted and used to create an addition class called the anomaly class. These anomalies produce dome shaped response in the Mahalanobis distance, similar in shape to an upside-down soup bowl, and have been seen in every pipe we have scanned. Finally, no-flaw signatures were collected as well. The final training set consist of 961 flaw signatures, 1157 anomaly signatures, and 2000 no-flaw signatures.

4.2 Interpreting the Mahalanobis Distance

Once the Mahalanobis distance is calculated, it is the spikes that are of interest. The larger the distances from zero, the greater the difference between the features of the signature under test and the features derived from the no-flaw signature set. By calling the distance the flaw distance, the plots of the Mahalanobis distance classification can be interpreted more intuitively, i.e. the larger the distance the more flaw like the signature.

Using the original classification technique there was no hope of designing a pattern recognition algorithm that could take the classification results (Mahalanobis distance) and mark the flaw indications which were SCCs. This was because there was no consistency between classifications. Each pipe and sometimes each scanline on each pipe needed its own custom no-flaw set. Also there were frequently false positive flaw indications with large flaw distance values in locations where no known flaws of any type were located. As a result of this different feature sets and classification algorithms were experimented with. During these in-depth studies of numerous Mahalanobis distances, SCC responses were visually identified. This allowed a set of criteria that

Table 4.1: This table shows the specifications the parabolic cuts on scanline I and II were machined to. There were on lengths given in the specifications because the length was determined by how deep the cutting wheel went into the pipe wall [37]. The actual lengths as measured after the specified depth was reached are also listed.

Scanline	**Type of Defect**	**Defect "Name" (i.e. Number)**	**Specified Defect Size in Inches**			**Actual Measured Lengths in Inches**		
			Width	**Depth**	**Length**	***Cut 1***	***Cut 2***	***Cut 3***
I	Parabola	1 (2-cuts)	0.012	0.1875	N/A	0.774	0.772	
I	Parabola	2	0.012	0.28	N/A	0.877		
I	Parabola	3	0.012	0.1875	N/A	0.756		
I	Parabola	4	0.012	0.09	N/A	0.442		
I	Parabola	5	0.012	0.035	N/A	0.334		
I	Parabola	6	0.008	0.035	N/A	0.332		
I	Parabola	7	0.008	0.09	N/A	0.508		
I	Parabola	8	0.008	0.1875	N/A	0.765		
I	Parabola	9	0.008	0.28	N/A	0.85		
II	Parabola	1 (3-cuts)	0.02	0.1875	N/A	0.728	0.74	0.74
II	Parabola	2	0.02	0.28	N/A	0.864		
II	Parabola	3	0.02	0.1875	N/A	0.745		
II	Parabola	4	0.02	0.09	N/A	0.524		
II	Parabola	5	0.02	0.035	N/A	0.357		
II	Parabola	6	0.0156	0.28	N/A	0.87		
II	Parabola	7	0.0156	0.1875	N/A	0.713		
II	Parabola	8	0.0156	0.09	N/A	0.587		
II	Parabola	9	0.0156	0.035	N/A	0.392		

Table 4.2: There are two scanlines containing parabolic cuts on the machined pipe. This table list the depth of each defect, what percentage of the pipe wall thickness the maximum depth is, the average depth of the cut (since the maximum depth listed is a point depth), and the percentage of the pipe wall thickness the average depth reaches [37].

Parabolic Flaw Set I

Number	Maximum Depth	% of Wall	Average Depth of Cut	Average % Wall
1	0.1875	50.00%	0.131	34.82%
2	0.28	74.67%	0.200	53.46%
3	0.1875	50.00%	0.131	34.82%
4	0.09	24.00%	0.061	16.31%
5	0.035	9.33%	0.024	6.27%
6	0.035	9.33%	0.024	6.27%
7	0.09	24.00%	0.061	16.31%
8	0.1875	50.00%	0.131	34.82%
9	0.28	74.67%	0.200	53.46%

Parabolic Flaw Set II

Number	Maximum Depth	% of Wall	Average Depth of Cut	Average % Wall
1	0.1875	50.00%	0.131	34.82%
2	0.28	74.67%	0.200	53.46%
3	0.1875	50.00%	0.131	34.82%
4	0.09	24.00%	0.061	16.31%
5	0.035	9.33%	0.024	6.27%
6	0.28	74.67%	0.200	53.46%
7	0.1875	50.00%	0.131	34.82%
8	0.09	24.00%	0.061	16.31%
9	0.035	9.33%	0.024	6.27%

a response in the Mahalanobis distance must poses in order to be a defect (SCC) indication.

1. The response must roughly be triangular without a bottom in shape.

2. A “white-cone” must be visible under the response.

3. The sides of the triangular “spike” should be “thin”.

Since only the most blatantly bad signatures are removed during the quality check step of the preprocessing there can still be corrupted signatures present. These “missed” corrupt signatures show up in the Mahalanobis distance as single points with flaw distances hundreds to thousands of times the largest flaw distance of a non-solitary-point spike. Because of this the Mahalanobis distance results are usually filtered using two different filters/smoothing operations to allow the shape, magnitude, and presence of a “white-cone” to be determined.

The most frequently used filter is simply a running averaging operation where the Mahalanobis distance of every five signatures is replaced by the average and the five associated position measurements are replaced by the average of the position values. A new Mahalanobis distance vector and position vector are assembled with the average flaw distance and position representing the five signatures and their positions. This is safely done without affecting the characteristics used to identify defect indications as an SCC since the axial resolution of the EMAT system is so high. On average there are 91 signatures per inch before cleaning, 78 signatures per inch after cleaning, and 16 signatures per inch after the running average operation. The EMAT head itself is 2.75-inches wide and the coil (the active sensing area) is 1.5-inches wide. So, with 16 signatures per inch there is still substantially high resolution, given that each signature senses at least a 1.5-inch wide, axial “window.”

It is also relevant at this point to mention that the length of a defect can be determined by measuring the width of the defect’s response starting were the response rises above the mean level of the flaw distances leading up to the defect response and ending where the response returns to the mean flaw distance values following the response. This is illustrated in Figure 4.4 where the actual flaw has a length of 0.865-inches and the defect response measures 2.54-inches, subtracting 1.5-inches for the width of the active portion of the EMAT returns a width of 1.04-inches. This is quite an acceptable measure of the flaw’s actual length considering the subjectiveness of selecting the location where the response rises above and returns to the local average flaw distance and that the focus of this research has been on the more important goal of reliable, repeatable SCC detection. After all you cannot size what you cannot find.

Finally, the other filter commonly applied to the Mahalanobis distances removes spikes formed by single points. This "spike filter" takes nine data points at a time and calculates the mean and standard deviation of their flaw distance values. Then the mean plus two and a half times the standard deviation is used as a threshold. Any single point with a flaw distance greater than the threshold is replaced by the mean flaw distance value of the nine points.

4.3 Experiments

This section describes and shows the outcomes from using the final 25-feature set and the original 13-feature set with both the final classification algorithm and the original classification algorithm. The data classified is from the two scanlines with parabolic cuts, scanline I and II. Ten scans of each scanline are classified and the number of correctly identified defects (true positives), incorrectly identified defects (false positives), undetected defects (false negatives), and the repeatability of a detection are calculated (i.e. number of times a defect was identified correctly (true positive) in the ten scans of a scanline). The validation of the final feature set, training set, and final classification algorithm is shown by these experiments as well. The two scanlines and the ten scans of each are two unique tests with ten trials of each test conducted, allowing for confidence in the results.

In the following sections the two key comparisons are made by calculating the difference between classification results 1. when the original and final feature sets are classified using just the original classification algorithm, 2. when the original and final feature sets are classified using only the final classification algorithm. This way the effects of the different feature sets and the effects of the two classification techniques can be isolated and compared as two separate events. By being able to evaluate these two changes separately improvements solely due to the feature set, solely due to the classification algorithm, and then due to the combination of these will be shown.

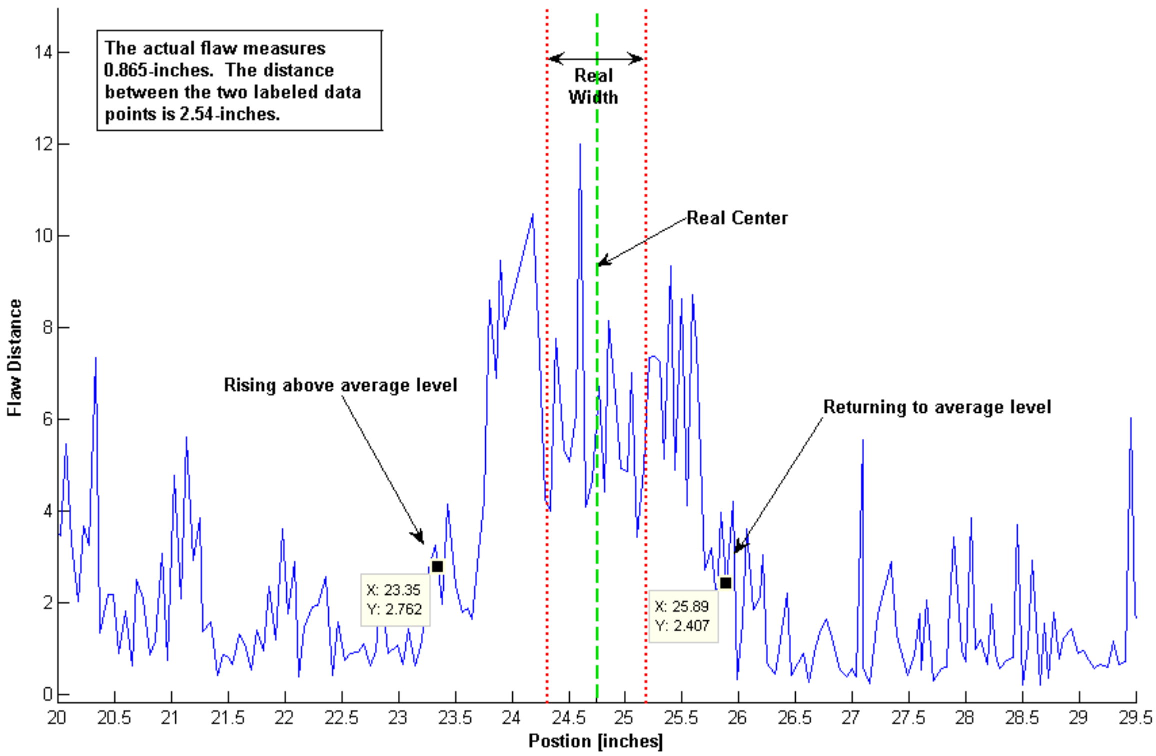

Figure 4.4: The width of a defect response is nominally 1.5-inches wider than the actual defect. Where the response's width is measured from the location were it rises above and returns to the local mean flaw distances immediately preceding and following the response.

4.3.1 Both Feature Sets using the Original Classification Algorithm

In this section the classification results using the original feature set with the original classification technique is compared with the classification results when the final feature set is also used in conjunction with the original classification technique. This provides a baseline for comparing the two feature sets based on the effectiveness of the original classification technique.

The original classification algorithm used to detect SCCs at the beginning of this research used the thirteen original features and the Mahalanobis distance from a "good" set as the classifier. At the time the 13-feature set was in use, the "good" set was formed by taking stationary data from a location that was marked as defect-free in the pipe under test. This data was acquired from scans taken of a decommissioned pipe containing natural SCCs at the Battelle PSF. The defect-free area was based on the information in the pipe's original assay report. Early on it became apparent that the *stationary* no-flaw signatures did not adequately reflect the variation that is present in no-flaw signatures taken while *moving*, as can be seen in Figure 4.5.

Because the stationary signatures were not providing an acceptable "good" set pauses during scans to collect stationary "good" sets were eliminated. Instead the "good" sets were created from signatures gathered while moving, but still from a range in the pipe under test listed as defect free. Since the original classification algorithm used a "good" set from an actual decommissioned pipe, a problem prone attribute in itself, in order to calculate the original feature set and use the original classification algorithm on the machined pipe the no-flaw signatures in the training set are used as the "good" set. All other steps and calculations for the original features and the original classification algorithm remain as they were. The use of the no-flaw signatures from the training set constructed from the machined pipe data actually improves the original feature set and classifier's calculations since there is 100% certainty that the no-flaw signatures are flaw and anomaly free. Something that could never be claimed about a "good" set derived from a decommissioned pipe section.

Before continuing it is important to take note of what the highest priorities as far as defect detection goes. There is no standard that address calculating the remaining strength of a pipe section containing a crack. There is a standard for making such a calculation for external corrosion on a pipe. This calculation is conservative even

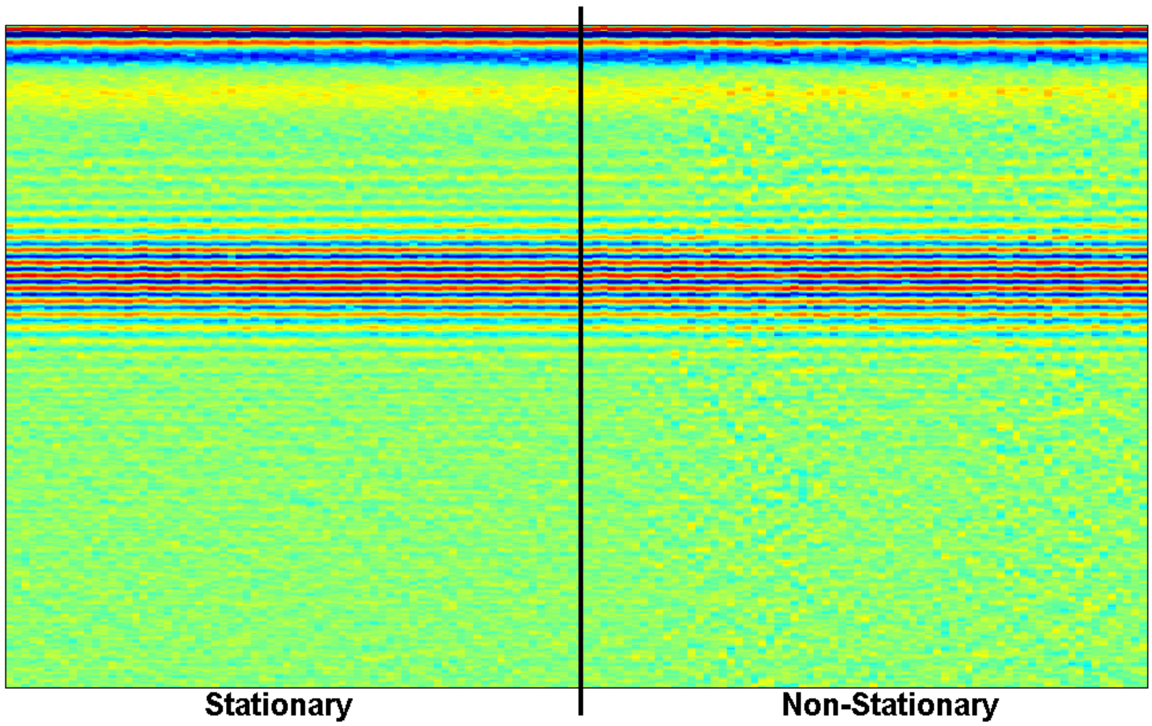

Figure 4.5: This B-scan image shows 72 signatures gathered while the PIG was stationary and 72 signatures collected while the PIG was moving, both from defect-free areas of the machined pipe.

for corrosion and so if used for other types of defects provides at least the same conservative estimate of remaining strength. The remaining strength of a pipe section is based on how long and deep the defect is. The calculation results in a length that a defect with same maximum through wall depth would be when either the pressure in the pipeline would need to be lowered or the section repaired to continue operating at the current pressure [39]. For the defects on the machined pipe the length that each defect must equal or exceed is shown in Table 4.3. The results when using the original features set with the original classifier are shown in Table 4.4.

The results for the final feature set using the original classifier are shown in Table 4.5. There is a sub-table for each scanline. The numbers listed on the left-hand side identifies one of the 10 scans. The row shows which defects were detected during that scan. The maximum through wall depth percentage and the average through wall depth percentage of each defect on the scan line are listed below their respective defect number. Each column is a single synthetic SCC defect and the scans in which it was detected. The percentage at the bottom of each column represents the percentage of times that defect was detected. A detection is indicated by a '**X**'.

With this in mind, notice in Tables 4.4 and 4.5 that the deepest defects are repeatedly detected, while the shallower defects are detected at a much lower rate, if at all. This directly impacts the number of false negatives since each row of the table that has a column without an '**X**' is automatically a false negative. The number of true positives, false positives, and false negatives for the original feature set, original classification algorithm combination is shown in Figure 4.6 and for the final feature set, original classification algorithm combination in Figure 4.7. The number of false positive is still of importance since in the eventual commercial usage of this technology to inspect natural gas pipelines locations with true positives, and therefore false positives, would likely be excavated for repair. As this is not an easy, cheap, or inexpensive proposition it is just as important that there be as close to 100% true positive detection of significant defects while keeping the false positives to a minimum.

4.3.2 Both Feature Sets using the Final Classification Algorithm

The section contains the results when using the original features set with the final classification algorithm, Table 4.6 and for when the final feature set is used with the

Table 4.3: The calculation, in [39], for determining the maximum allowable length of a corrosion based on the pipe wall thickness and the maximum depth of the defect was made for all 18 of the synthetic SCCs in scanline I and II of the machined pipe. Each column contains the average percentage through the pipe wall, the maximum percentage through the pipe wall, the actual length of the defect, the maximum allowable length, and the "buffer" between that maximum length and the actual length (i.e. how much longer the crack could grow before requiring repair or replacement).

Scanline I

	# 1	**# 2**	**# 3**	**# 4**	**# 5**	**# 6**	**# 7**	**# 8**	**# 9**
Average % Depth	34.82%	53.46%	34.82%	16.31%	6.3%	6.3%	16.31%	34.82%	53.46%
Maximum % Depth	50%	74.67%	50%	24%	9.3%	9.3%	24%	50%	74.67%
Actual Length [in]	1.546	0.877	0.756	0.442	0.334	0.332	0.508	0.765	0.85
Cutoff Length [in]	2.82	1.83	2.82	6.96	15.03	15.03	2.82	6.96	6.38
Remaining Length to Cutoff (Actual - Cutoff) [in]	1.27	0.95	2.06	6.52	14.69	14.69	2.31	6.19	5.53

Scanline II

	# 1	**# 2**	**# 3**	**# 4**	**# 5**	**# 6**	**# 7**	**# 8**	**# 9**
Average % Depth	34.82%	53.46%	34.82%	16.31%	6.3%	53.46%	34.82%	16.31%	6.3%
Maximum % Depth	50%	74.67%	50%	24%	9.3%	74.67%	50%	24%	9.3%
Actual Length [in]	2.208	0.864	0.745	0.524	0.357	0.87	0.713	0.587	0.392
Cutoff Length [in]	2.82	1.83	2.82	6.96	15.03	1.83	2.82	6.96	15.03
Remaining Length to Cutoff (Actual - Cutoff) [in]	0.61	0.96	2.07	6.44	14.67	0.96	2.10	6.37	14.63

Table 4.4: Defects that were correctly identified using the *Original Feature Set* and the *Original Classification Algorithm* are marked in a separate table for each scanline. Correctly identified defects are indicated by a 'X'. Each row is a scan of the same scanline, while the columns are the nine defects. The percent through the pipe wall of each defect's maximum point depth and average depth are listed below each defect ID. The percentage of times that a defect was identified across all ten scans is listed at the bottom of each table as well.

Scanline I — Original Feature Set and Original Classifier											
		# 1	# 2	# 3	# 4	# 5	# 6	# 7	# 8	# 9	
		50%	74.7%	50%	24%	9.3%	9.3%	24%	50%	74.7%	Max % of Wall
		34.8%	53.5%	34.8%	16.3%	6.3%	6.3%	16.3%	34.8%	53.5%	Avg % of Wall
Scan of Scanline I	1									X	
	2	X	X							X	
	3	X									
	4	X									
	5	X	X						X	X	
	6	X									
	7	X		X							
	8	X								X	
	9	X	X				X		X	X	
	10	X					X			X	
		90%	30%	10%	0%	0%	20%	0%	20%	60%	% Detected

Scanline II — Original Feature Set and Original Classifier											
		# 1	# 2	# 3	# 4	# 5	# 6	# 7	# 8	# 9	
		50%	74.7%	50%	24%	9.3%	74.7%	50%	24%	9.3%	Max % of Wall
		34.8%	53.5%	34.8%	16.3%	6.3%	53.5%	34.8%	16.3%	6.3%	Avg % of Wall
Scan of Scanline II	1	X	X				X		X		
	2	X	X				X		X		
	3	X	X				X	X			
	4	X	X				X	X			
	5	X	X				X				
	6	X	X				X				
	7	X	X				X				
	8	X	X				X	X			
	9	X	X				X		X		
	10	X	X				X	X			
		100%	100%	0%	0%	0%	100%	40%	30%	0%	% Detected

Table 4.5: Defects that were correctly identified using the *Final Feature Set* and the *Original Classification Algorithm* are indicated by a 'X' with a separate table for each scanline. The rows are the results for one of the 10 scans made of each scanline, while the columns are the nine defects. The percent through the pipe wall of each defect's maximum point depth and average depth are listed below each defect ID. The percentage of times that a defect was identified across all ten scans is listed at the bottom of each table as well.

Scanline I — Final Feature Set and Original Classifier

		# 1	# 2	# 3	# 4	# 5	# 6	# 7	# 8	# 9	
		50%	74.7%	50%	24%	9.3%	9.3%	24%	50%	74.7%	**Max % of Wall**
		34.8%	53.5%	34.8%	16.3%	6.3%	6.3%	16.3%	34.8%	53.5%	**Avg % of Wall**
Scan of Scanline I	**1**	X							X	X	
	2	X	X	X					X	X	
	3	X	X	X						X	
	4	X	X						X	X	
	5	X	X						X	X	
	6	X									
	7	X		X						X	
	8	X							X	X	
	9	X	X				X		X	X	
	10	X					X			X	
		100%	50%	30%	0%	0%	20%	0%	60%	90%	**% Detected**

Scanline II — Final Feature Set and Original Classifier

		# 1	# 2	# 3	# 4	# 5	# 6	# 7	# 8	# 9	
		50%	74.7%	50%	24%	9.3%	74.7%	50%	24%	9.3%	**Max % of Wall**
		34.8%	53.5%	34.8%	16.3%	6.3%	53.5%	34.8%	16.3%	6.3%	**Avg % of Wall**
Scan of Scanline II	**1**	X	X	X			X	X			
	2	X	X				X				
	3	X	X				X	X			
	4	X	X				X	X			
	5	X	X				X	X			
	6	X	X				X				
	7	X	X				X				
	8	X	X				X	X			
	9	X	X				X	X			
	10	X	X				X	X			
		100%	100%	10%	0%	0%	100%	70%	0%	0%	**% Detected**

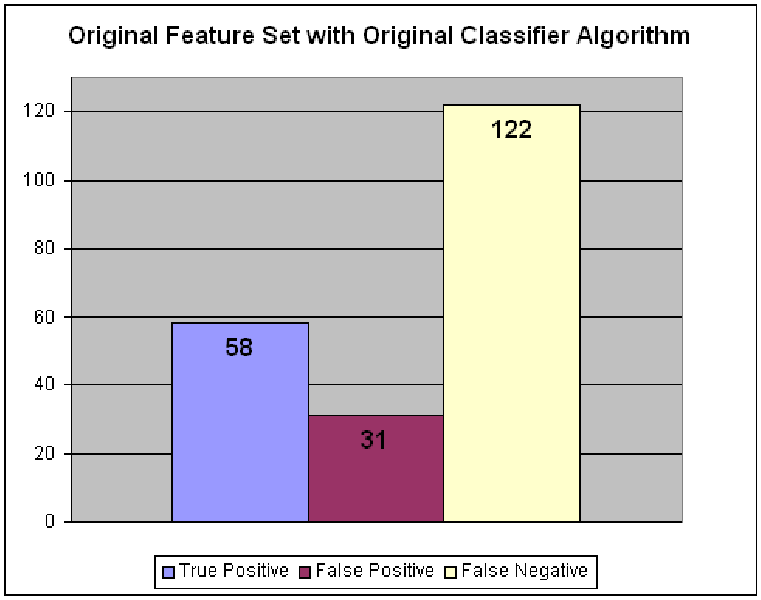

Figure 4.6: The cumulative number of true positives, false positives, and false negatives resulting from using the original feature set with the original classification algorithm for all 20 scans.

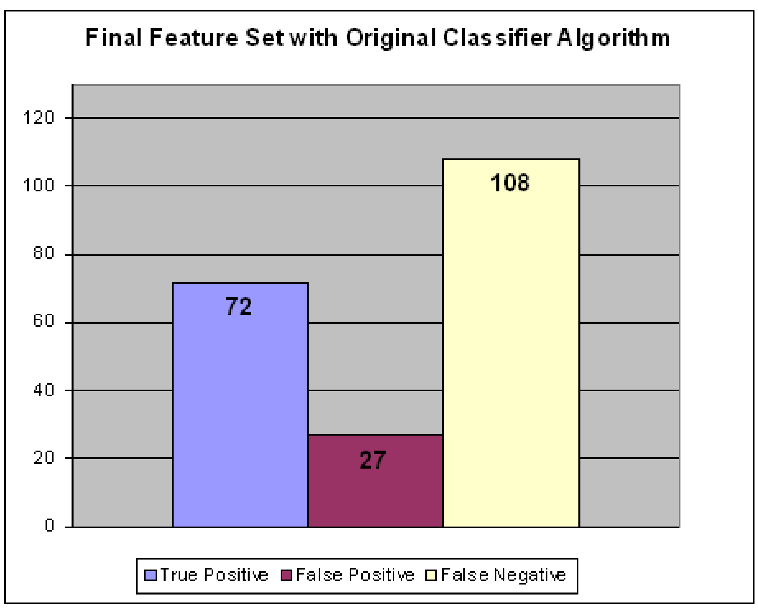

Figure 4.7: The cumulative number of true positives, false positives, and false negatives resulting from all 20 pipe scans when the final feature set and the original classification algorithm were used.

final classification algorithm, Table 4.7. There is a sub-table for each scanline. The numbers listed on the left-hand side identifies one of the 10 scans where the row shows which defects were detect during that scan. The maximum through wall depth percentage and the average through wall depth percentage of each defect on the scan line are listed below their respective defect number. Each column is a single synthetic SCC defect and the scans in which it was detected. The percentage at the bottom of each column represents the percentage of times that defect was detected. A detection is indicated by a '**X**'.

As before in Section 4.3.1, when examine the following results keep in mind that the highest priority, as far as defect detection goes, is to detect as many of deep defects possible, while holding the number of false positives to a minimum. Likewise, uses Table 4.3 as a conservative rule of thumb for determining how close a defect's length is to the "cutoff" length where a repair would be required. In a commercial usage of this technology to inspect natural gas pipelines locations with true positives, and therefore false positives, would likely require the section of pipe containing the true positive or false positive to be excavated. Because of the inherent danger and expense of excavating a section of a natural gas line it is important that there be minimal false positives.

4.3.3 Results Summary

This section compares the results of all four possible combinations of the two features sets and two classification algorithms. Figure 4.10 shows the number of true positives, false positives, and false negatives of each combination side by side. The total percentage of detections achieved by each combination based on the average percentage through the pipe wall of is shown in Figure 4.11. Finally, the percentage of defects each combination detect based on a specific range of average through wall depth is shown in Figure 4.12. That is to say what percentage of defects was detected out of all possible depths (Defects 6.3% through 53.5%), the percentage detected not counting the shallowest defects (Defects 16.3% through 53.5%), and the percentage detected of only the two deepest defects (Defects 34.8% through 53.5%). As you can see from these graphs the final feature set with the final classification algorithm detected the deepest defects far better than any of the other combinations. It also kept the number of false positives to a dramatically lower rate than any of the others.

Table 4.6: Defects that were correctly identified using the *Original Feature Set* and the *Final Classification Algorithm* are indicated by a 'X' with a separate table for each scanline. The rows are the results for one of the 10 scans made of each scanline, while the columns are the nine defects. The percent through the pipe wall of each defect's maximum point depth and average depth are listed below each defect ID. The percentage of times that a defect was identified across all ten scans is listed at the bottom of each table as well.

Scanline I — Original Feature Set and Final Classifier

		# 1	**# 2**	**# 3**	**# 4**	**# 5**	**# 6**	**# 7**	**# 8**	**# 9**	
		50%	74.7%	50%	24%	9.3%	9.3%	24%	50%	74.7%	**Max % of Wall**
		34.8%	53.5%	34.8%	16.3%	6.3%	6.3%	16.3%	34.8%	53.5%	**Avg % of Wall**
Scan of Scanline I	**1**	X								X	
	2	X	X	X						X	
	3	X		X						X	
	4	X		X							
	5	X	X	X					X	X	
	6	X		X							
	7	X		X						X	
	8	X								X	
	9	X	X	X			X		X	X	
	10	X		X			X			X	
		100%	30%	80%	0%	0%	20%	0%	20%	80%	**% Detected**

Scanline II — Original Feature Set and Final Classifier

		# 1	**# 2**	**# 3**	**# 4**	**# 5**	**# 6**	**# 7**	**# 8**	**# 9**	
		50%	74.7%	50%	24%	9.3%	74.7%	50%	24%	9.3%	**Max % of Wall**
		34.8%	53.5%	34.8%	16.3%	6.3%	53.5%	34.8%	16.3%	6.3%	**Avg % of Wall**
Scan of Scanline II	**1**	X	X				X	X		X	
	2	X	X				X	X			
	3	X	X				X	X		X	
	4	X	X				X	X			
	5	X	X		X		X	X			
	6	X	X	X			X	X		X	
	7	X	X	X	X		X	X			
	8	X	X				X	X			
	9	X	X	X	X		X	X			
	10	X	X				X	X			
		100%	100%	30%	30%	0%	100%	100%	0%	30%	**% Detected**

Table 4.7: Defects that were correctly identified using the *Final Feature Set* and the *Final Classification Algorithm* are indicated by a 'X' with a separate table for each scanline. The rows are the results for one of the 10 scans made of each scanline, while the columns are the nine defects. The percent through the pipe wall of each defect's maximum point depth and average depth are listed below each defect ID. The percentage of times that a defect was identified across all ten scans is listed at the bottom of each table as well.

Scanline I — Final Feature Set and Final Classifier

Scan of Scanline I	# 1	# 2	# 3	# 4	# 5	# 6	# 7	# 8	# 9	
	50%	74.7%	50%	24%	9.3%	9.3%	24%	50%	74.7%	Max % of Wall
	34.8%	53.5%	34.8%	16.3%	6.3%	6.3%	16.3%	34.8%	53.5%	Avg % of Wall
1	X	X						X	X	
2	X	X	X						X	
3	X	X	X					X	X	
4	X	X	X						X	
5	X	X	X					X	X	
6	X	X	X					X	X	
7	X	X	X					X	X	
8	X							X	X	
9	X	X				X		X	X	
10	X	X	X					X	X	
	100%	90%	70%	0%	0%	10%	0%	80%	100%	% Detected

Scanline II — Final Feature Set and Final Classifier

Scan of Scanline II	# 1	# 2	# 3	# 4	# 5	# 6	# 7	# 8	# 9	
	50%	74.7%	50%	24%	9.3%	74.7%	50%	24%	9.3%	Max % of Wall
	34.8%	53.5%	34.8%	16.3%	6.3%	53.5%	34.8%	16.3%	6.3%	Avg % of Wall
1	X	X				X				
2	X	X				X				
3	X	X				X	X			
4	X					X				
5	X	X	X			X	X			
6	X	X	X			X	X			
7	X	X	X			X	X			
8	X	X	X			X	X			
9	X	X	X			X	X			
10	X	X				X	X			
	100%	90%	50%	0%	0%	100%	70%	0%	0%	% Detected

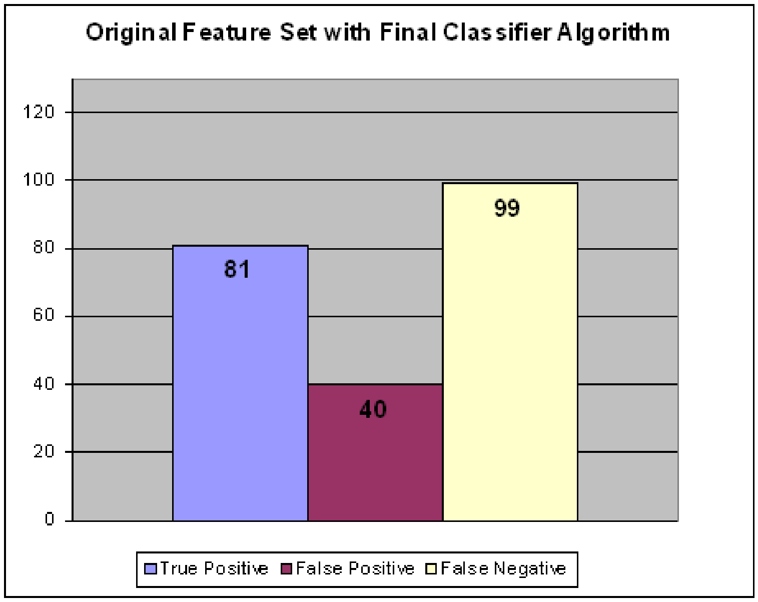

Figure 4.8: The cumulative number of true positives, false positives, and false negatives resulting from all 20 pipe scans when the original feature set and the final classification algorithm were used.

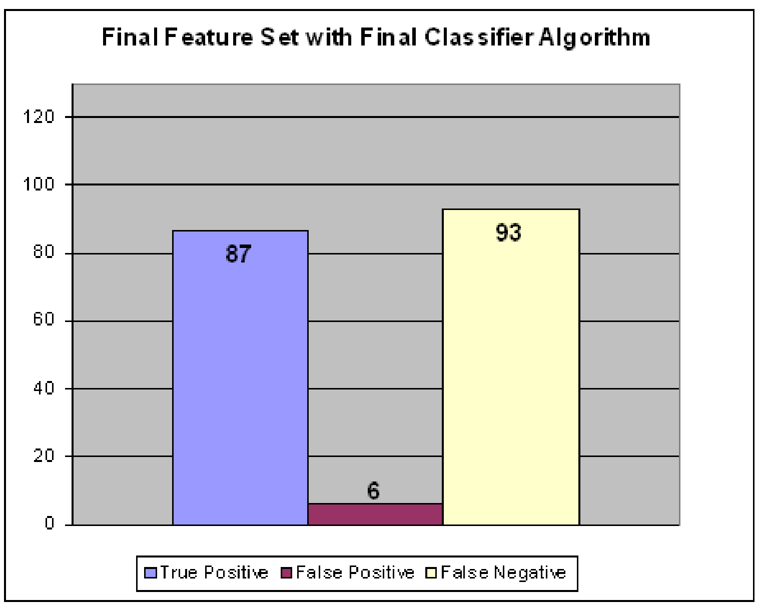

Figure 4.9: The cumulative number of true positives, false positives, and false negatives resulting from using the final feature set with the final classification algorithm for all 20 scans.

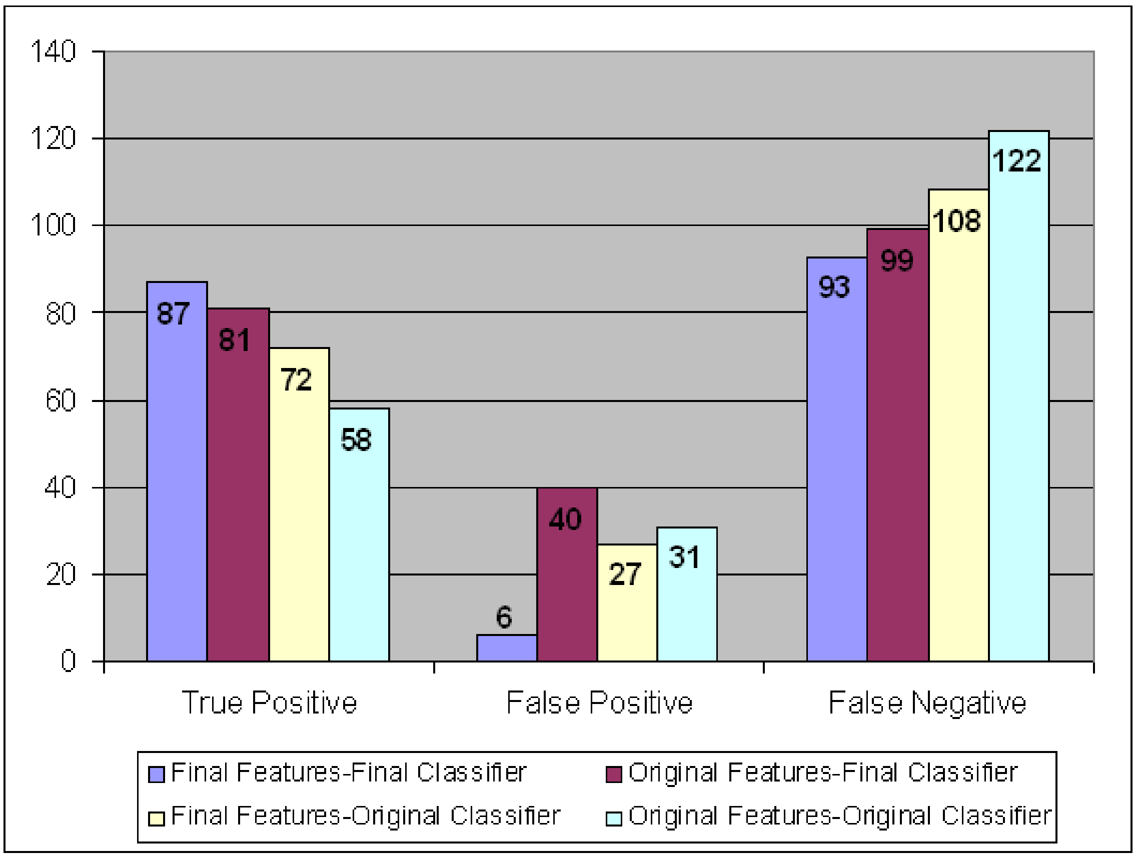

Figure 4.10: This bar chart shows how many true positives, false positives, and false negatives each feature set and classifier combination had in total.

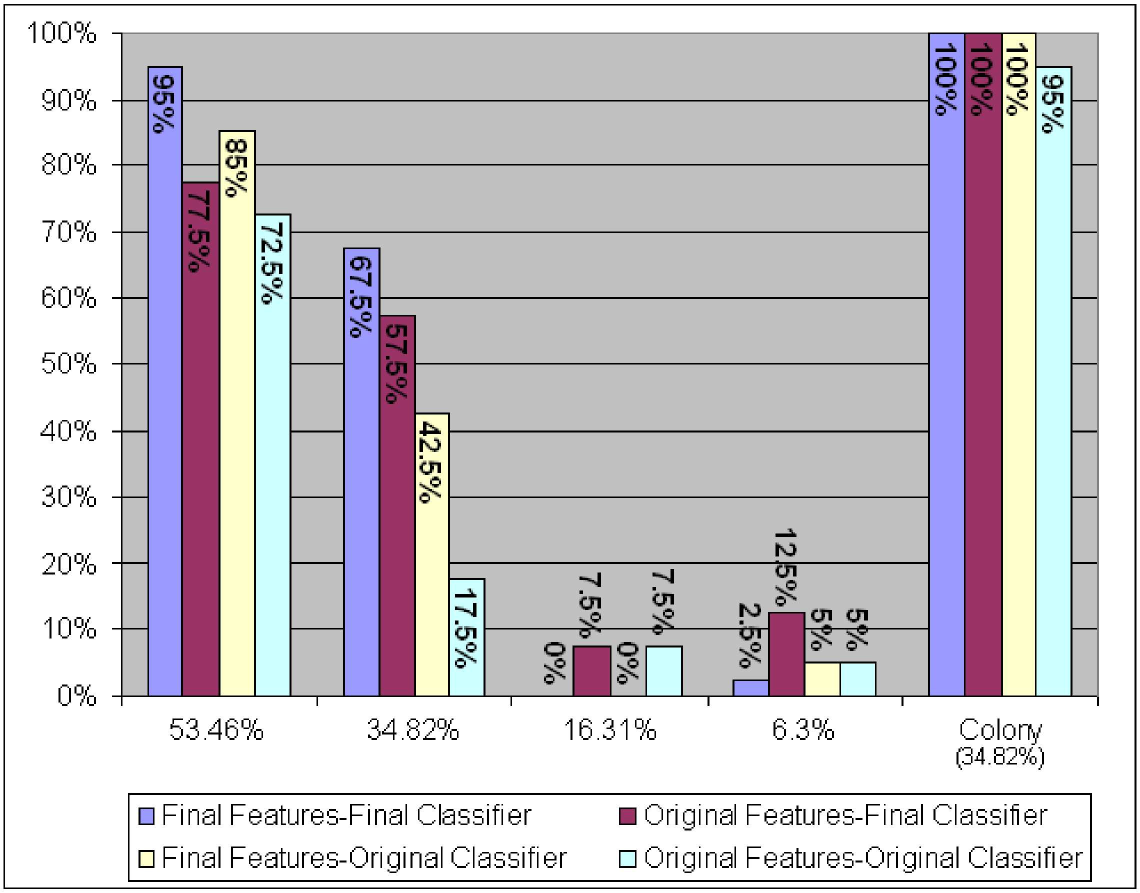

Figure 4.11: This bar chart shows the percentage of detections each feature set and classifier combination had for each "type" of defect on the machined pipe. Where the "types" are single cracks with an average through wall depth of 53.5%, 34.8%, 16.3%, and 6.3%, and the colony defects with an average through wall depth of 34.8%.

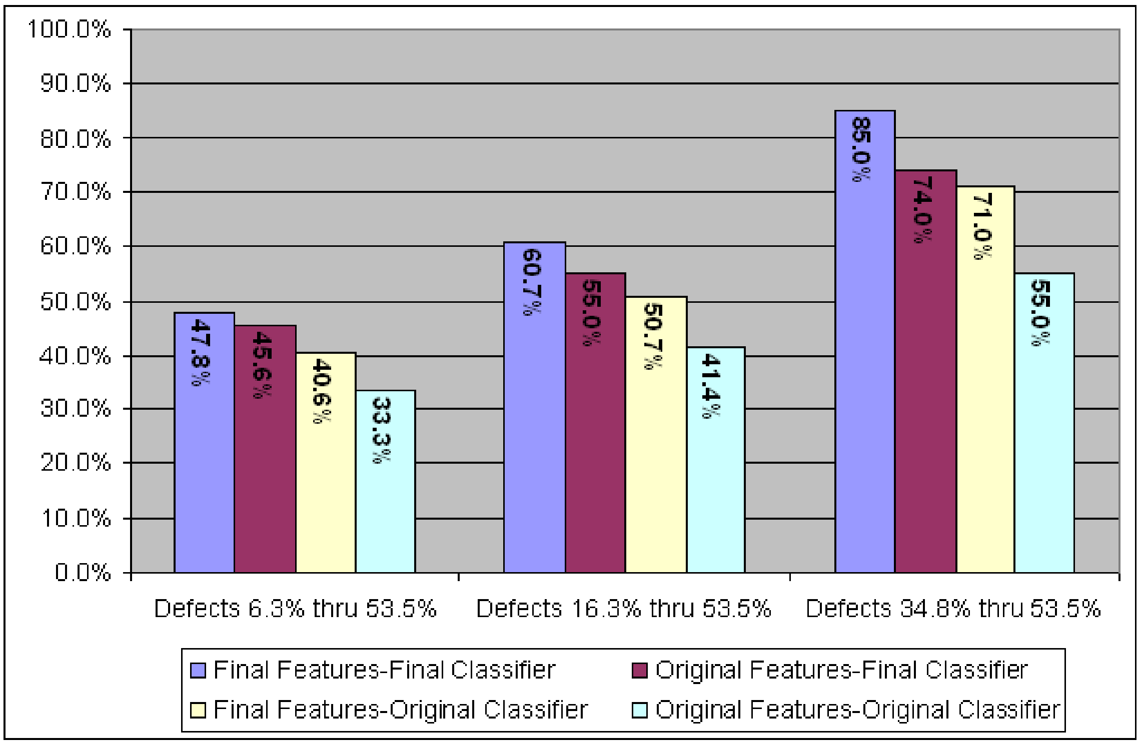

Figure 4.12: This bar chart shows the percentage of detections each feature set and classifier combination had based on the range of average depths. So the defects with an average through wall depth between 6.3% through 53.5% represents all possible defects on the machined pipe. The defects 16.% through 53.3% represents all but the shallowest defects. The defects 34.8% through 53.5% contains the most serious defects (53.5% through the pipe wall and the colonies) and the defects that would need close monitoring (34.8% through the pipe wall).

4.4 Blind Scan of a Decommissioned Pipe Containing Real SCCs

Up to this point all of the results and comparisons have been made using data collected from the machined pipe. While it was only possible to show statistical proof of the improvements achieved when using the final feature set and the final classification algorithm with the machine pipe, the question still remains; do those improvements remain when applied in a real-world environment? Specifically, is the low false positive rate seen in the machined pipe test also exhibited on real pipes? This section shows the results of using the final feature set, the final classification algorithm, and the training set in a blind test inspection of a decommissioned 26-inch diameter natural gas pipe known to contain SCCs, as well as corrosion, pitting, and a manufacturing defect. This blind test illustrates the robustness of the training set, feature set, and algorithm, since these elements were developed on a 30-inch diameter pipe with a wall thickness of 0.375-inches and in this case are applied to a 26-inch diameter pipe with a wall thickness of 0.281-inches.

This blind test was performed at the Battelle PSF. The staff at the PSF selected three scanlines on the pipe and specified four or five regions on each scanline that the results would be judged by. The volume of data collected makes it unreasonable to show all the scans from all the scanlines. What follows is a Mahalanobis distance that typifies the results seen in all the scans, Figure 4.13. The solid line boxes labeled SCC 7, SCC 8, SCC 9, and SCC 10 are the regions PSF staff to be used in the judging. The dashed line boxes labeled Defect #6, Defect #7, and Defect #9 mark locations that according to the 1994 MPI inspection of the pipe, contained SCCs. The numbered arrows identify valid defect responses. There is one exception in the case of the displayed Mahalanobis distance, arrow number 2. Two of the scanlines were separated circumferentially by only 14.75-inches. So while officially the defects labeled #6, #7, and #9 were the only SCC defects on this scanline there was a defect at arrow 2 that was within the circumferential scanning "window" of the EMATs. Since the PIG does not travel through the pipe with the EMAT heads precisely straddling the intended scanline, the defect at arrow 2, on the neighboring scanline, was frequently detected. The displayed classification result, Figure 4.13, is from the tenth scan of this scanline. In the first nine scans, a valid defect indication was produced at arrow 2. In the tenth scan there was no response at arrow 2 due to the orientation of the EMATs with respect to the scanline being slightly different. All other responses in the displayed scan are typical of the nine other scans. After the results of the blind inspection were released a follow-up trip to the Battelle PSF was made specifically to visually re-inspecting and document the size, type, and location of defects on the pipe. Additionally, all the locations that corresponded to a defect response in the Mahalanobis distance were inspected. This was done to allow us to determine a possible source for what at the time was thought to be an unacceptably high number of false positives. It turned out that there was not a false positive problem, instead the systems ability to detect multiple types of flaws was proven[‡]. Figures 4.14 through Figure 4.25 are the pictures taken corresponding to each arrow and defect in Figure 4.13. The caption of each image list the defect or arrow label of the corresponding defect response in the Mahalanobis distance and the type of defect(s) present, along with any significant additional information regarding that defect(s).

[‡]Until this blind test, all of the decommissioned pipe sections that had been scanned had contained only SCCs and some very minor corrosion. This decommissioned pipe section was the first to contain SCCs and significant corrosion and pitting.

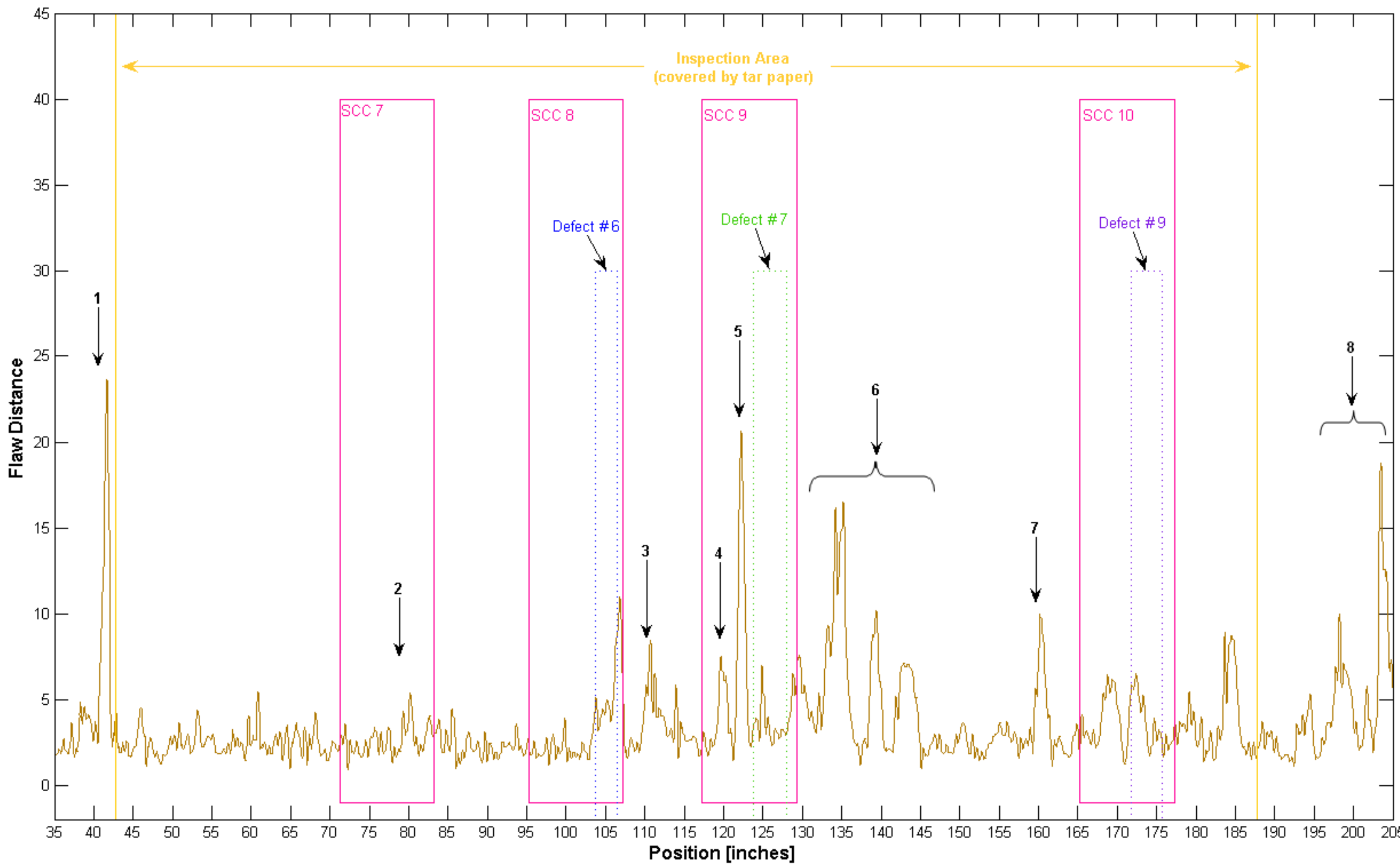

Figure 4.13: The filtered Mahalanobis distance classification results from the blind test inspection of a decommissioned section of natural gas pipeline is shown here. The pink solid line boxes labeled SCC 7, 8, 9, and 10 mark the areas designated by the test proctors and used to "grade" the systems performance. The dashed line boxes with the labels Defect #6, #7, and #9 mark areas that, according to the 1994 MPI assay of the pipe section, contained SCCs. The arrows labeled 1 through 8 mark defect responses, and are used in the following figures to correlate the physical source of these responses.

Figure 4.14: ***Indicator*: Arrow 1; *Defect Type*: Corrosion**

Figure 4.15: ***Indicator*****: Arrow 2;** ***Defect Type*****: Corrosion**
The Mahalanobis distance response shown on the right is representative of the defect response present in the first nine out of ten scans. The defect at arrow 2 is actually on the neighboring scanline. It is only an inch or so circumferentially outside the EMATs' "field of view," so whether it was detected or not, depended on the circumferential orientation. The scan shown in Figure 4.13 had a slight circumferentially "slip" that moved this defect out of the scan's field of view. Which is perfectly acceptable since it was technically not intended to be detected on this scanline as part of the blind test.

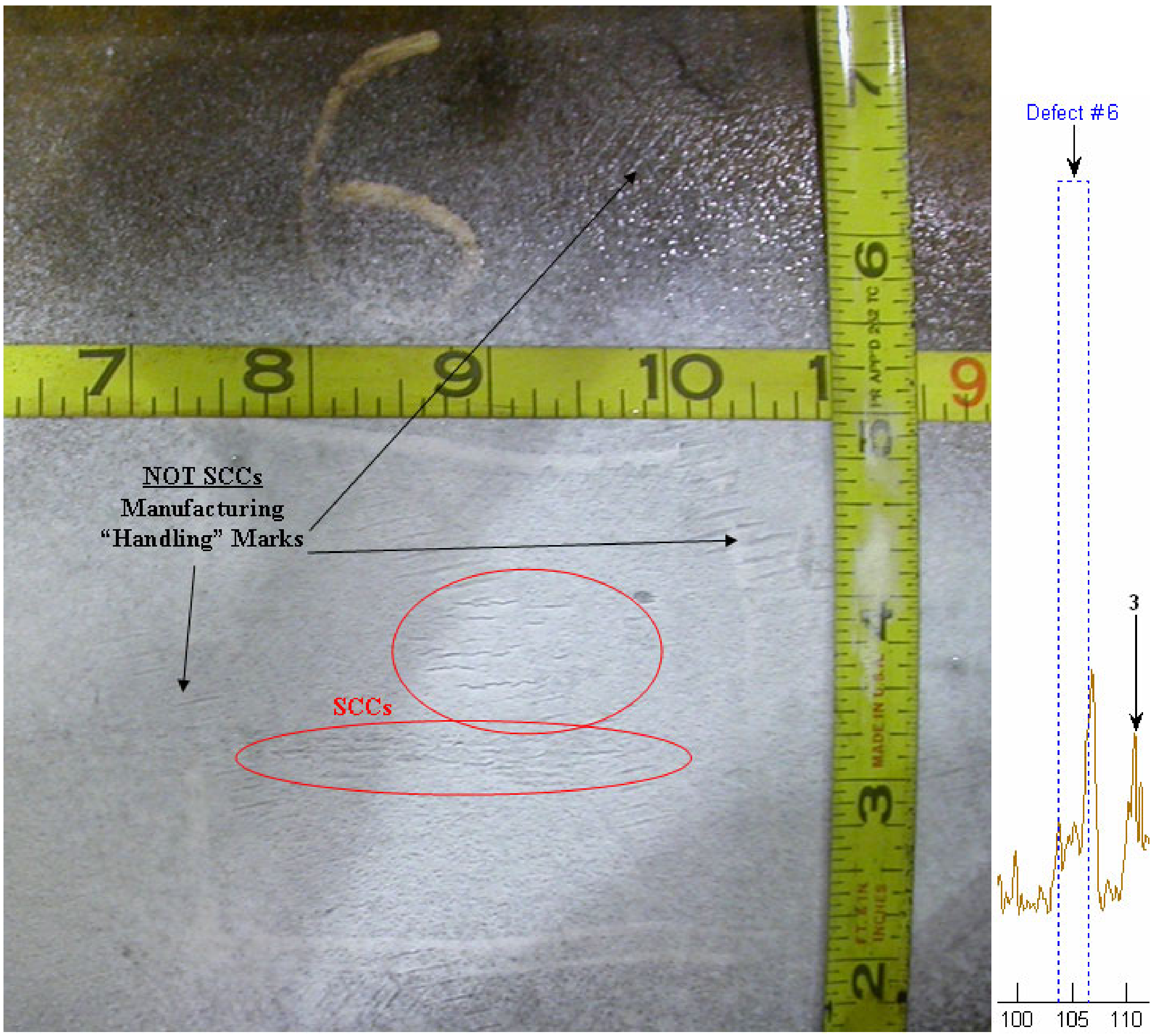

Figure 4.16: ***Indicator*: Defect #6; *Defect Type*: SCC Colonies**
The Mahalanobis distance on the right corresponds to Defect #6. The dashed line box is located based on information given in the original MPI assay of the pipe in 1994. The tape measure in the photograph allows the Mahalanobis distance results and actual defect locations to be correlated.

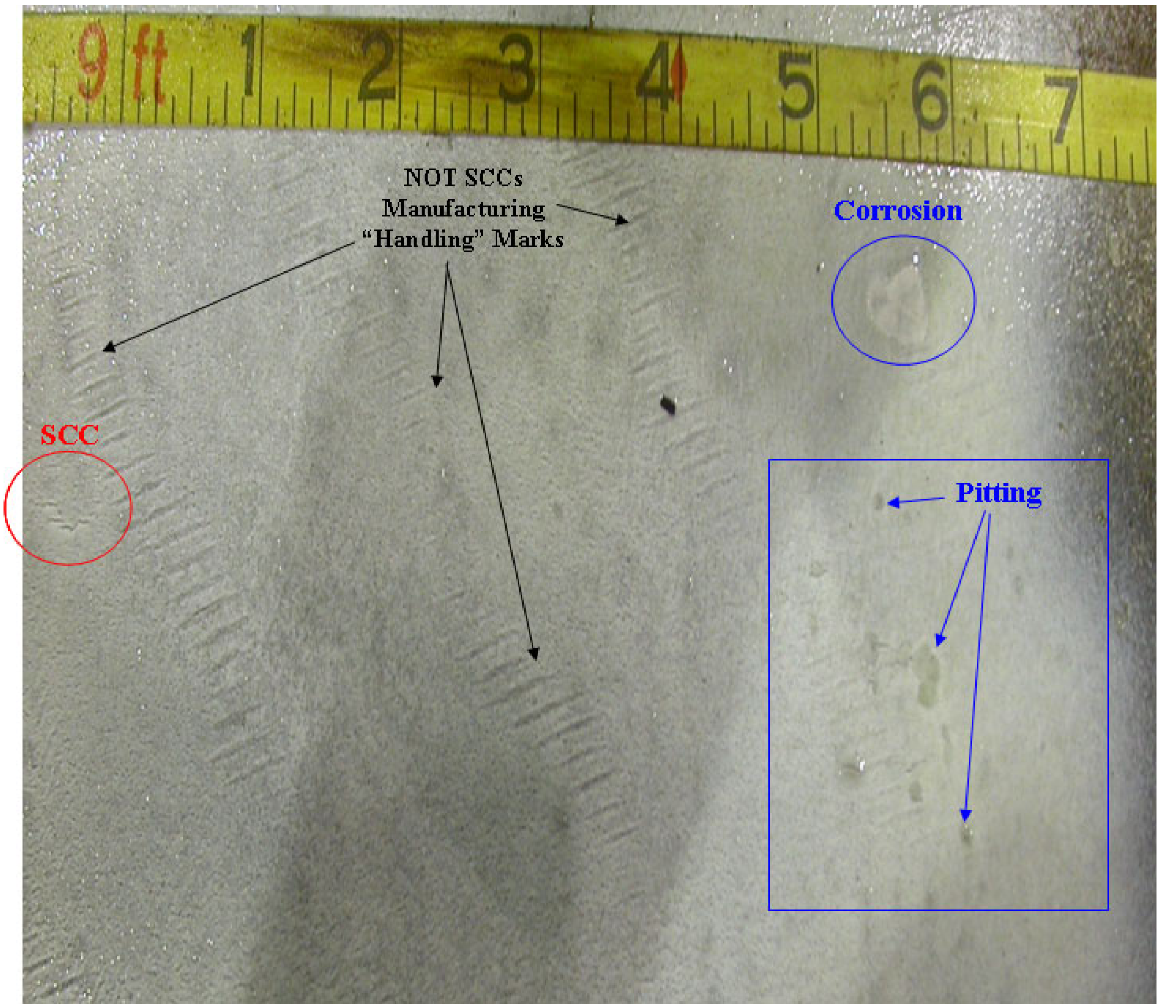

Figure 4.17: ***Indicator*****: Arrow 3;** ***Defect Type*****: SCCs, Pitting, and Corrosion**
The SCCs shown in this photograph were not identified by the 1994 MPI inspection of the pipe. They were identified visually for the first time during the re-inspection of the pipe after the final results of the blind test were released. The pits with arrows to them were singled out merely as examples of what a pit looks like with the white MPI contrast paint covering it.

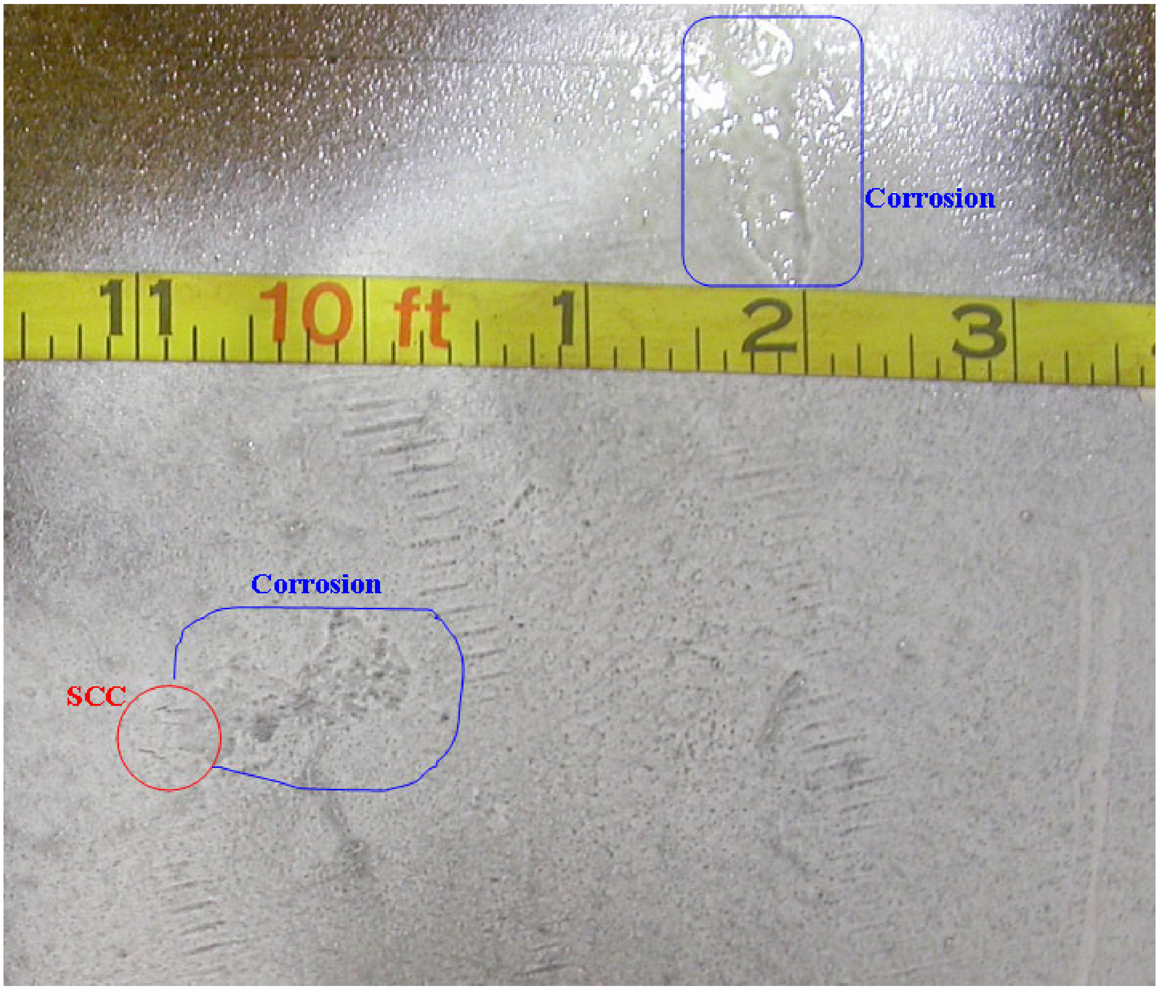

Figure 4.18: ***Indicator*: Arrow 4; *Defect Type*: SCCs and Corrosion**

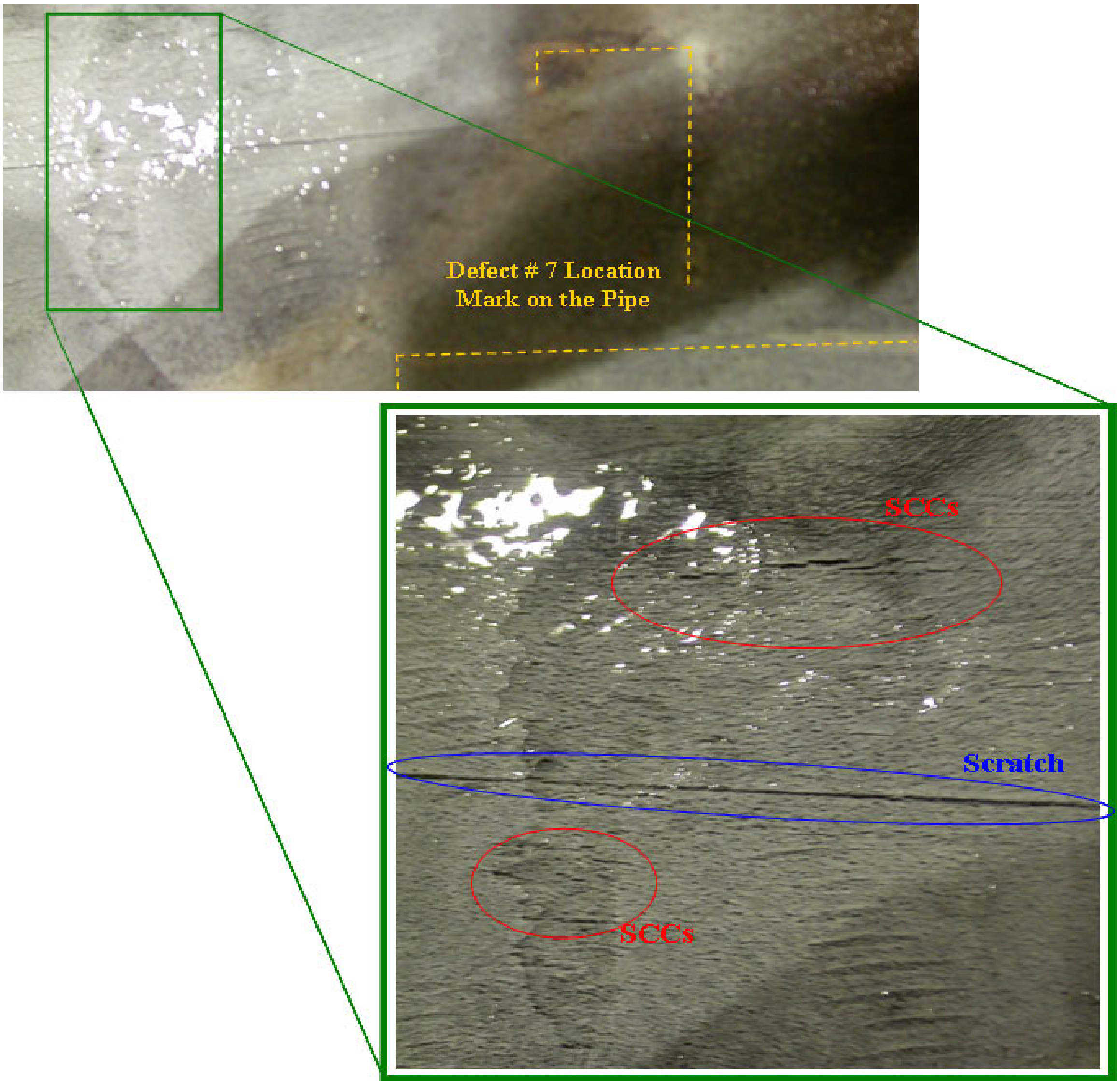

Figure 4.19: ***Indicator*: Arrow 5; *Defect Type*: SCC embedded in a Corrosion Patch This is a "new" SCC that was visually identified for the first time during the follow up visual inspection. These SCCs were not identified during the MPI characterization of this pipe in 1994. The yellow-orange dashed lines mark the box and seven drawn on the pipe, as seen in Figure 4.20, since the camera's flash "drowned" them out. These two landmarks are to help orientation these SCCs with respect to defects shown in the arrow 4 and Defect #7 figures.**

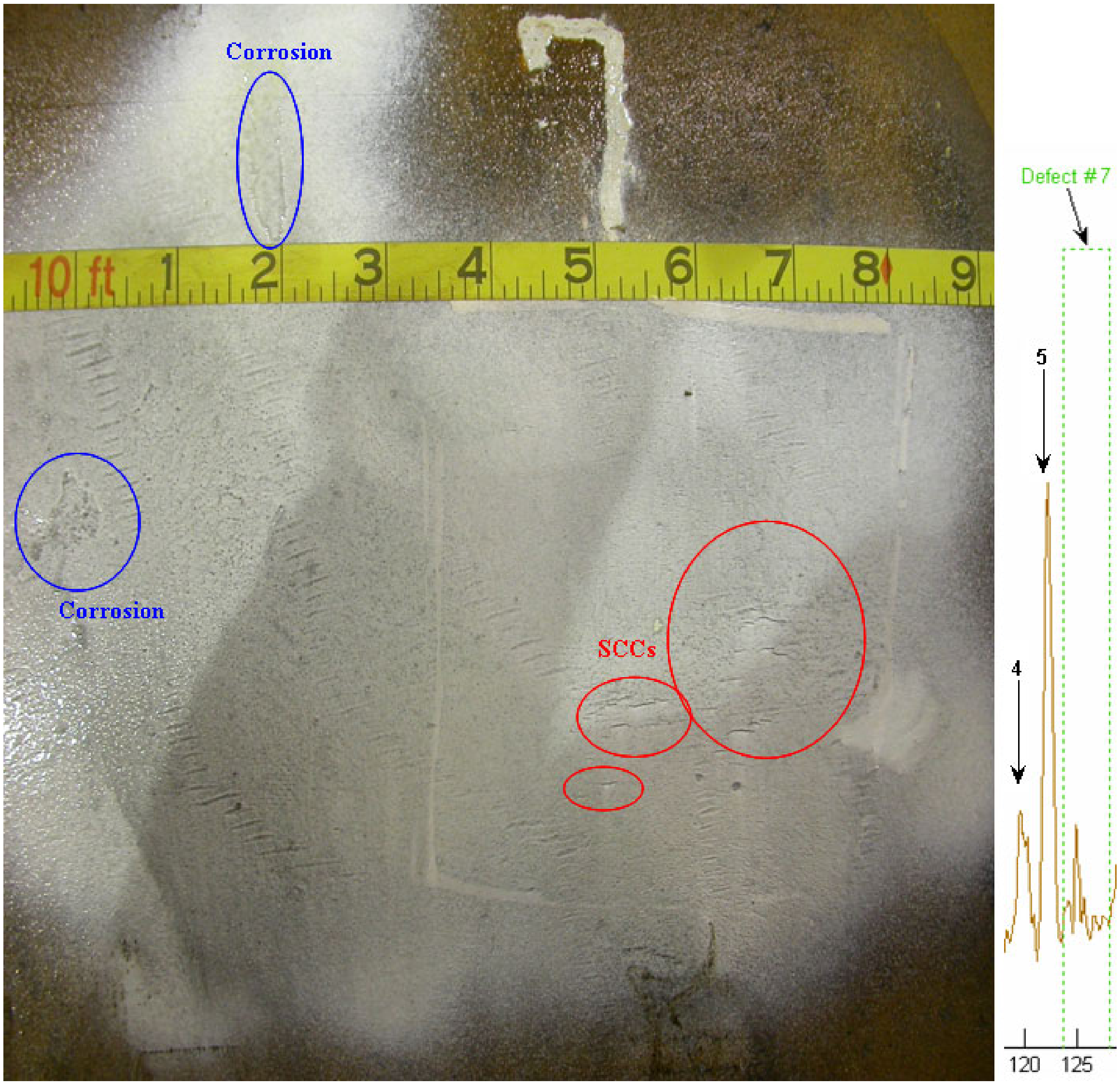

Figure 4.20: ***Indicator*: Defect #7; *Defect Type*: SCCs**
On the right, is the Mahalanobis distance for Defect #7, along with arrow 4 and 5. The circled corrosion patch above the tape measure is the same area shown magnified in Figure 4.19.

Figure 4.21: ***Indicator*: Arrow 6; *Defect Type*: Corrosion**
The corrosion patches marked by arrow 6 cover such a large area only the first eight inches are shown here. The final four plus inches of corrosion patches are shown in Figure 4.22.

Figure 4.22: ***Indicator*: Arrow 6; *Defect Type*: Corrosion**
This photograph shows the last four plus inches of the corrosion patches arrow 6 identifies. The first eight inches of these corrosion patches are shown in Figure 4.21.

Figure 4.23: ***Indicator*: Arrow 7; *Defect Type*: Corrosion Patch**

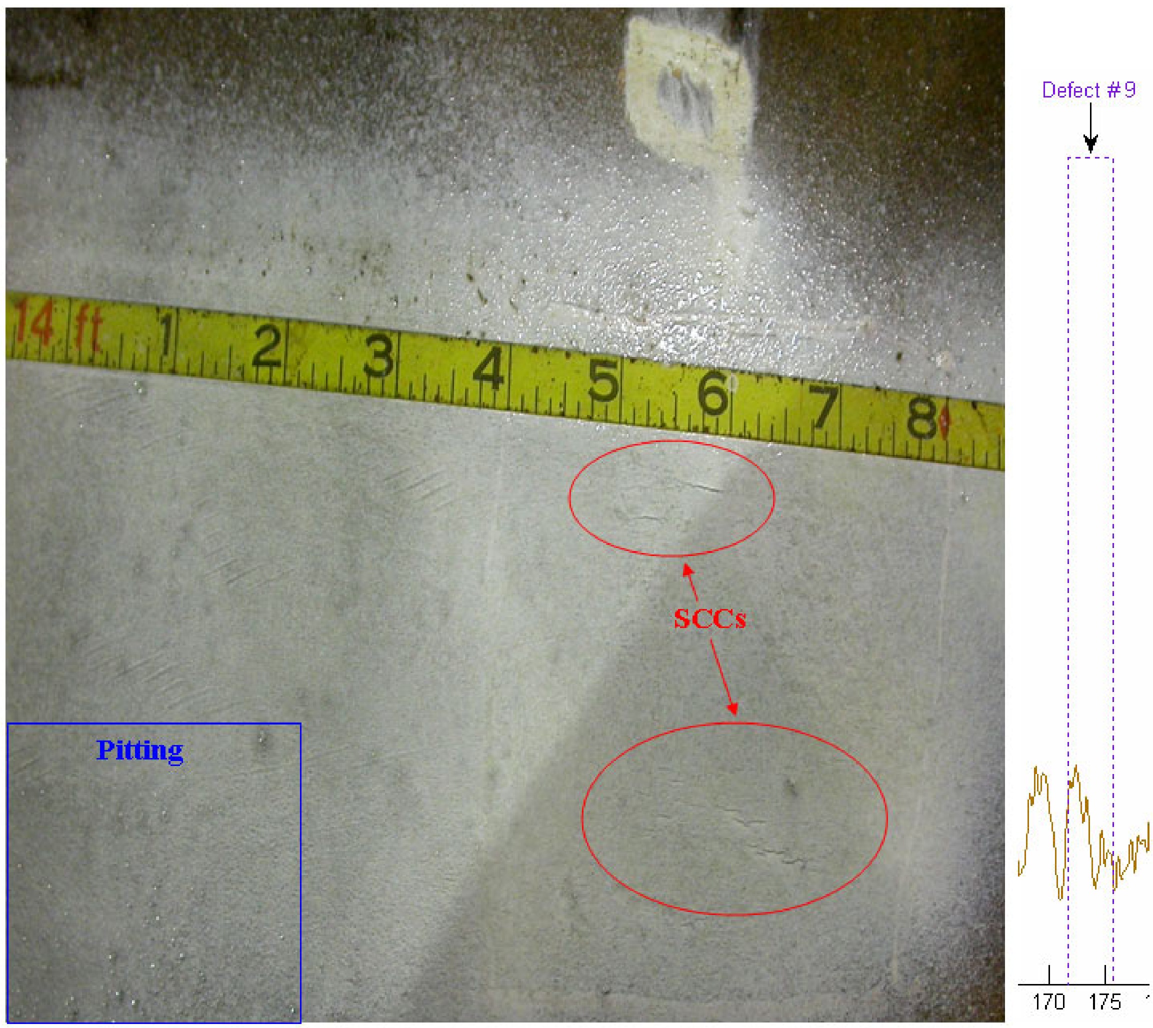

Figure 4.24: ***Indicator*: Defect #9; *Defect Type*: SCCs and Pitting**
The Mahalanobis distance for the area in the photograph is shown on the right.

Figure 4.25: ***Indicator*: Arrow 8; *Defect Type*:** Corrosion Patches

Chapter 5

Conclusions

While there has been a notable increase in research to develop a means for detecting SCCs in natural gas pipelines there are still significant challenges facing this research, such as overcoming the attenuation the protective coating on buried pipes causes. However, through the research presented in this thesis a method which overcomes the foremost challenge of simply detecting SCCs using non-contact, ultrasonic inspection while moving was presented. There is still plenty of room for further improvement, but a foundation is firmly in place. While most of the results shown in this thesis focus on synthetic SCCs in a clean, unused pipe, the majority of this research was performed using data collected from decommissioned pipe containing real SCCs. The results from the experiments involving real SCC samples are far more difficult to objectively quantify due to the uncertainty associated with these decommissioned pipe sections. This same uncertainty prevented a training set from being formed using natural SCCs. Before the training set created from the parabolic cuts on machined pipe, there was not a single "good" set that produced repeatable, believable[*] results on a pipe other than the one it was created from. However, the training set constructed from the machined pipe has been successfully used on 30-inch diameter pipes with different wall thickness from the machined pipe as well as on 26-inch diameter pipes with wall thicknesses different from that of the machined pipe. Formerly, having a "good" set that performed the same for all the scanlines on the same piece of pipe the set was created from was a rare event. Also, using PCA+LDA has significantly improved the discernibility of both synthetic and real SCC. Primarily by suppressing the responses

[*]Sometimes there would not be a single defect response in an entire Mahalanobis distance result or everything would produce a defect response; so the results were not believable.

generated by metallurgic variations and small changes in gap between the EMAT and the pipe wall. The system has detected 100% of the synthetic colony SCCs with an average volume of missing material equaling only 0.0039 cubic inches, 95% of the synthetic single crack SCCs with an average volume of missing material equaling a mere 0.0024 cubic inches, and 67.5% of the synthetic SCCs with an average volume of missing material equal to just 0.0014 cubic inches!

5.1 Future Work

As with any experimental system with the goal of making a classification, the classification is only as good as the feature set and therefore by association in this case the training set. The final feature set does not take advantage of any phase or frequency information. While some investigations into at least simple frequency base features was done and in the end were found to be detrimental to the classification, there is likely beneficial information in the frequency domain. In particular, a feature utilizing phase in some way or another may hold potential. Of the existing features, the quality/benefit of the point-by-point Mahalanobis distance squared feature is still something of a question. In a quick test using the final classification algorithm the final feature set was used with and without the point-by-point Mahalanobis distance squared features. The classification results were better when the point-by-point Mahalanobis distance squared features were included. At the time these test were enough to continue using the point-by-point Mahalanobis distance squared features, but a more thorough investigation would be beneficial.

Since nearly all SCCs which would require repair or heightened monitoring can be detected this research is ready for the next big step. The next significant goal is two equally important items; the ability to distinguish between types of defects and the ability to objectively determine at least crack length and ideally crack depth (maximum depth, average depth, or both). The ability to distinguish types of defects is important and necessary advancement for the system. When the final feature set and final classification algorithm were used to perform a blind inspection of a decommissioned section of 26-inch diameter natural gas pipeline, as shown in Section 4.4,defect responses were produced that corresponded in every instance to an actual defect on the pipe. The caveat however is that the sources of the defect responses are not limited to just SCCs, but include corrosion and pitting. The ability to detect all types of defects is a desired outcome, since only the ability to use just one inspection tool to inspect for all major pipe integrity issues is highly desired by the pipeline industry. But without the ability to separate the major types of defects and some measure of either the volume of missing material or the maximum depth and length of a defect, the remaining life of the pipe and priority for repair cannot be determined.

The classification results from using the original feature set and the original classifier were so inconsistent that there was no possibility of automating the identification of defect responses. However, with the improvements yielded by the combination of the final feature set and the final classification algorithm, the results have consistent behavior that could be used to automate the identification of defects responses and include the ability to disregard anomaly responses. This would be very beneficial, ideally eliminating the need for a highly experienced person to visually identify defect responses from anomaly response. This would also greatly reduce the amount of time needed for this task.

Bibliography

Bibliography

[1] Energy Information Administration. *Annual Energy Review 2006*. Tech. Rep. DOE/EIA-0384(2006), Energy Information Administration (EIA), June 2007. URL: http://tonto.eia.doe.gov/FTPROOT/multifuel/038406.pdf; Released: June 27, 2007; Next Update: June 2008.

[2] Office of Pipeline Safety. *2005 Transmission Annuals Data*. Electronic Data Files, June 2006. URL: http://ops.dot.gov/stats/DT98.htm.

[3] Eiber, R. J. and Kiefner, J. F. *Failure Analysis and Prevention. ASM Handbook*, vol. 11, 2002.

[4] Michael Baker Jr., I. *Stress Corrosion Cracking Study*. Tech. Rep. Integrity Management Program, Report TTO Number 8, Delivery Order DTRS56-02-D-70036, Department of Transportation, Office of Pipeline Safety, January 2005.

[5] Magnaflux. *Innovations: A Timeline*. Website. URL: http://www.magnaflux.com/overview/timeline.stm, accessed Jan 11, 2007.

[6] Magnaflux. *7HF Black/9CM Red Visible Magnetic Particle Wet Method Prepared Bath*. Product Data Sheet, April 2003. URL: http://www.magnaflux.com/files/library/pds/material_product_data_sheets/Magnaflux~reg_7HF~9CM_Wet_Method_Visible_Prepared_Bath.pdf, accessed Jan 11, 2007.

[7] Magnaflux. *14AM, 14A Aqua-Glo, 14A Redi-Bath, 20B Fluorescent Magnetic Particle Prepared Bath*. Product Data Sheet, July 2004. URL: http://www.magnaflux.com/files/library/pds/material_product_data_sheets/Magnaglo~reg_14AM_14A_Aqua-Glo_14A_Redi-Bath_20B.pdf, accessed Jan 11, 2007.

[8] Jiles, D. C. *Review of magnetic methods for nondestructive evaluation (Part 2)*. *NDT International*, vol. 23, no. 2, pp. 83–92, April 1990. Formerly known as Non-Destructive Testing; Continued as NDT & E International.

[9] Iowa State University. *Pipeline Inspection*. Website, May 2003. URL: http://www.ndt-ed.org/AboutNDT/SelectedApplications/PipelineInspection/PipelineInspection.htm, accessed Feb 21, 2007.

[10] Iowa State University. *Portable Magnetizing Equipment for Magnetic Particle Inspection*. Website, April 2003. URL: http://www.ndt-ed.org/EducationResources/CommunityCollege/MagParticle/Equipment/EquipmentPortable.htm, accessed Jan 11, 2007.

[11] Clark, T. and Nestleroth, B. *Gas Pipeline Pigability*. Topical Report. OSTI ID: 826134, Battelle for the Department of Energy, Columbus, OH, April 2004.

[12] Nestleroth, J. B. and Bubenik, T. A. *Magnetic Flux Leakage (MFL) Technology For Natural Gas Pipeline Inspection*. Tech. Rep., February 1999. URL: http://www.battelle.org/pipetechnology/MFL/MFL98Main.html; for The Gas Research Institute (GRI).

[13] ROSEN. *Corrosion Detection Pig (CDP)*. Website. URL: http://www.roseninspection.net/RosenInternet/InspectionServices/ILInspection/MagneticFlux/CDP/, accessed Mar 3, 2007.

[14] Iowa State University. *Magnetic Field Orientation and Flaw Detectability*. Website, September 2006. URL: http://www.ndt-ed.org/EducationResources/CommunityCollege/MagParticle/Physics/FieldOrientation.htm, accessed Feb 23, 2007.

[15] Nestleroth, J. B. and Bubenik, T. A. *MFL Tutorial*. Tech. Rep., October 2000. URL: http://www.battelle.org/pipetechnology/MFL/Links/tutorial1.html?; Created as aid for the Magnetic Flux Leakage (MFL) Technology For Natural Gas Pipeline Inspection report.

[16] Hirao, M. and Ogi, H. *SH-wave EMAT technique for gas pipeline inspection*. *NDT & E International*, vol. 32, no. 3, pp. 127–132, Apr 1999.

[17] Luo, W. and Rose, J. *Guided wave thickness measurement with EMATs. Insight: Non-Destructive Testing and Condition Monitoring*, vol. 45, no. 11, pp. 735–739, November 2003.

[18] Tucker Jr., R. W., Kercel, S. W., and Varma, V. K. *Characterization of Gas Pipeline Flaws using Wavelet Analysis*. In: *Proceedings of SPIE*, vol. 5132, pp. 485–493. Gatlinburg, TN, United States, 2003.

[19] Thurston, R. N. and Pierce, A. D. (editors). *Ultrasonic Measurement Methods*, *Physical Acoustics*, vol. 19. New York: Academic Press, 1990.

[20] Harkins, W. *Ultrasonic Testing of Aerospace Materials*. Tech. Rep., Marshall Space Flight Center, February 1999. URL: http://www.nasa.gov/offices/oce/llis/0765.html; NASA Engineering Network, Public Lessons Learned Entry: 0765.

[21] Kercel, S. W., Tucker Jr., R. W., and Varma, V. K. *Pipeline Flaw Detection with Wavelet Packets and GAs*. In: *Proceedings of SPIE - The International Society for Optical Engineering*, vol. 5103, pp. 217–226. Orlando, FL, United States, 2003.

[22] Datel, Inc. *PCI-417 Series Advanced Performance Analog Boards for Desktop PCI Bus Computers*. Manual., 2003. Note: All Datel data acquisition products discontinued as of Sep. 30, 2004.

[23] Instruments, M. *TB-1000 Gated Amplifier/Receiver Plug-In Card*. Tech. Rep., 2002. URL: http://www.matec.com/mindt/products/pc_cards/tb-1000/; Accessed Jan 11, 2007.

[24] Sigmund, J. *A,B,C's of Ultrasonics*. PowerPoint Presentation, 2001. URL: http://www.sonix.com/learning/ultrasonics.php3, accessed February 10, 2007.

[25] Kercel, S. W., Klein, M. B., and Pouet, B. *In-Process Detection of Weld Defects using Laser-Based Ultrasonic Lamb Waves*. Technical Report. ORNL/TM-2000/346, Oak Ridge National Laboratory, Oak Ridge, TN, November 2000.

[26] Akansu, A. N. and Haddad, R. A. *Multiresolution Signal Decomposition: Transforms, Subbands, Wavelets*. 1st edn. Academic Press, 1992.

[27] Duda, R. O., Hart, P. E., and Stork, D. G. *Pattern Classification*. 2nd edn. New York: John Wiley & Sons, Inc., 2001.

[28] Zhao, J., Wang, G.-Y., Wu, Z.-F., *et al. The Study on Technologies for Feature Selection*. In: *Proceedings of 2002 International Conference on Machine Learning and Cybernetics*, vol. 2, pp. 689–693. Beijing, China, 2002.

[29] Guyon, I. and Elisseeff, A. *An Introduction to Variable and Feature Selection*. *Journal of Machine Learning Research*, vol. 3, pp. 1157–1182, 2003.

[30] Bubenik, T., Nestleroth, J., Davis, R., *et al. In-Line Inspection Technologies for Mechanical Damage and SCC in Pipelines - Final Report*. Report. DTRS56-96-C-0010, U.S. Department of Transportation, Office of Pipeline Safety, June 2000.

[31] Hubert, C. J. *Applied Discriminant Analysis*. New York: John Wiley & Sons, Inc., 1994.

[32] Jain, A. K., Duin, R. P. W., and Mao, J. *Statistical pattern recognition: a review*. *IEEE Transactions on Pattern Analysis and Machine Intelligence*, vol. 22, no. 1, pp. 4–37, 2000.

[33] Price, J. and Gee, T. *Face recognition using direct, weighted linear discriminant analysis and modular subspaces*. *Pattern Recognition*, vol. 38, no. 2, pp. 209–219, Feb 2005.

[34] Zhao, W., Chellappa, R., and Krishnaswamy, A. *Discriminant analysis of principal components for face recognition*. In: *Proceedings Third IEEE International Conference on Automatic Face and Gesture Recognition*, pp. 336–341. IEEE, Nara, Japan: IEEE Computer Society, 1998.

[35] Fidler, S. and Leonardis, A. *Robust LDA Classification by Subsampling*. In: *Conference on Computer Vision and Pattern Recognition Workshop*, vol. 8, p. 97. Los Alamitos, CA, USA: IEEE Computer Society, 2003.

[36] Yang, J. and Yang, J.-Y. *Why can LDA be performed in PCA transformed space?* *Pattern Recognition*, vol. 36, no. 2, pp. 563–566, February 2003.

[37] Varma, V. K. *Dimensions and Layout for the Machined SCC*, January 2005. Internal project documentation of specifications supplied to the machine shop contracted to produce the synthetic SCCs in the machined pipe.

[38] Kreith, F. and Goswami, D. Y. *The CRC Handbook of Mechanical Engineering.* The Mechanical Engineering Handbook Series, 2nd edn. Boca Raton: CRC Press, 2005. Mechanical Engineering Handbook.

[39] ASME. *Manual for Determining the Remaining Strength of Corroded Pipelines.* Manual. ASME B31G-1991, ASME International, 1991.

Vita

Austin Peter Albright, the son of Steve and Peggy Albright, was born in Knoxville, TN, on July 31, 1980. He graduated from Central High School in Knoxville in 1999. In May of 2004 he graduated from Tennessee Technological University (TTU) in Cookeville, Tennessee with a Bachelor of Science in Electrical Engineering. While an undergraduate at TTU he was a teaching assistant for Introduction to Electrical Engineering and an assistant to the research and development engineer. His senior year at TTU, Austin was part of the student hardware team that built the winning robot at the IEEE Southeast Conference (SeCon) student hardware competition in 2004. After graduating in 2004, he began working at Oak Ridge National Laboratory through the Higher Education Research Experience Program. In 2005, Austin began working on a Master of Science in Electrical Engineering at the University of Tennessee - Knoxville (UTK). During his graduate studies Austin was awarded the Department of Homeland Security Fellowship, becoming the only Department of Homeland Security Fellow in the entire state of Tennessee. At UTK, Austin worked with the Advanced Imaging and Collaborative Information Processing lab led by Dr. Hairong Qi. He has been working on the course work for a PhD in Electrical Engineering at UTK for the last year and a half, while simultaneously writing the thesis for his Master's degree. He graduated with a Master of Science Degree in Electrical Engineering in December 2007, and has continued to pursue a doctorate in Electrical Engineering. Austin currently lives in Knoxville, TN with his wife Melissa.